New constraints on the structure, thermochronology, and timing of the Ailao Shan-Red River shear zone, SE Asia

P.H. Leloup, N. Amaud, R. Lacassin, J. R. Kienast, T. M. Harrison, T. T. Phan Trong, A. Replumaz, P. Tapponnier

HAL Id: insu-01891116

https://insu.hal.science/insu-01891116

Submitted on 9 Oct 2018

New constraints on the structure, thermochronology, and timing of the Ailao Shan-Red River shear zone, SE Asia

P. H. Leloup,[1] N. Arnaud,[2] R. Lacassin,[1] J. R. Kienast,[3] T. M. Harrison,[4] T. T. Phan Trong,[5] A. Replumaz,[1] and P. Tapponnier[1]

Abstract. New structural, petrographic, and $^{40}Ar/^{39}Ar$ data constrain the kinematics of the ASRR (Ailao Shan–Red River shear zone). In the XueLong Shan (XLS), geochronological data reveal Triassic, Early Tertiary, and Oligo-Miocene thermal events. The latter event (33-26Ma) corresponds to cooling during left-lateral shear. In the FanSiPan (FSP) range, thrusting of the SaPa nappe, linked to left-lateral deformation, and cooling of the FSP granite occurred at ≈35Ma. Rapid cooling resumed at 25-29Ma as a result of uplift within the transtensive ASRR. In the DayNuiConVoi (DNCV), foliation trends NW-SE, but is deflected near large-scale shear planes. Stretching lineation is nearly horizontal. On steep foliations, shear criteria indicate left-lateral shear sense. Zones with flatter foliations show compatible shear senses. Petrographic data indicate decompression from ≈6.5kbar during left-lateral shear (temperatures >700°C). $^{40}Ar/^{39}Ar$ data imply rapid cooling from above 350°C to below 150°C between 25 and 22Ma without diachronism along strike. Along the whole ASRR cooling histories show two main episodes: (1) rapid cooling from peak metamorphism during left-lateral shear; (2) rapid cooling from greenschist conditions during right-lateral reactivation of the ASRR. In the NW part of the ASRR (XLS, Diancang Shan), we link rapid cooling 1 to local denudations in a transpressive environment. In the SW part (Ailao Shan and DNCV), cooling 1 resulted from regional denudation by zipper-like tectonics in a transtensive regime. The induced cooling diachronism observed in the Ailao Shan suggests left-lateral rates of 4 to 5 cm/yr from 27Ma until ≈17Ma. DNCV rocks always stayed in a transtensive regime and do not show cooling diachronism. The similarities of deformation kinematics along the ASRR and in the South China Sea confirms the causal link between continental strike-slip faulting and marginal basin opening.

1. Introduction

Three decades after the plate tectonics revolution, two fundamental questions involving continental lithosphere deformation are actively debated. Is deformation mostly localized along a few great fault zones, or is it mostly distributed on many small structures? Localization clearly occurs in the upper brittle part of the crust. Is deformation also localized in the lower ductile crust and in the upper mantle? In other words, should deforming continents be seen as a pack of rigid blocks floating on a viscous lower crust, or as large coherent lithospheric blocks?

Answers to such fundamental questions may appear obvious. This is, however, not the case mostly because of timescale problems. When studying active tectonics using instrumental seismicity or present-day geodesy, deformation can be quite precisely characterized but may only correspond to a snapshot, sampling at most 0.001% of a collision process history. One may wonder about the significance of such a short observational window. On the other hand, the geological structures only reveal selected deformation events resulting from the integrated deformation history, possibly including several deformation phases or increments. Because the structures formed during the initial stages of a collision are often affected by later events and because it is difficult to measure precisely the amount and timing of tectonic movements, the study of finite deformation only gives a limited picture of the deformation history. From this partial picture it is difficult to answer the following question: At a given time (or during a given tectonic episode lasting several million years) was deformation mostly absorbed by a few large, or many small, structures?

In the debate about continental deformation localization the example of the India-Eurasia collision zone has focused the attention of many scientists because it is the largest active collision zone on Earth. Since 1982, P. Tapponnier and coworkers, starting from plasticine experiments and field observations and followed by detailed laboratory analyses, have promoted the idea that a large fraction of Asian deformation was taken up by successive extrusions of large coherent continental masses along great strike-slip faults [e.g., *Tapponnier et al.*, 1982, 1986]. Such a view has been challenged by the alternative view that the Asian continent responds to deformation as a viscous fluid [e.g., *England and Houseman*, 1986; *Houseman and England*, 1993].

[1]Laboratoire de Tectonique, Mécanique de la Lithosphère, UMR 7578 CNRS, Institut de Physique du Globe de Paris, France.

[2]Laboratoire Magmas et Volcans, UMR 6524 CNRS, Université Blaise Pascal, Clermont-Ferrand, France.

[3]Laboratoire de Pétrologie, Minéralogie, Métallogénie, UPRES-A 7058 CNRS, Université Denis Diderot, Paris, France.

[4]W. M. Keck Center for Isotope Geochemistry, Department of Earth and Space Sciences and Institute of Geophysics and Planetary Physics, University of California, Los Angeles, California.

[5]Institute of Geological Sciences, NCNST, Hanoi, Vietnam.
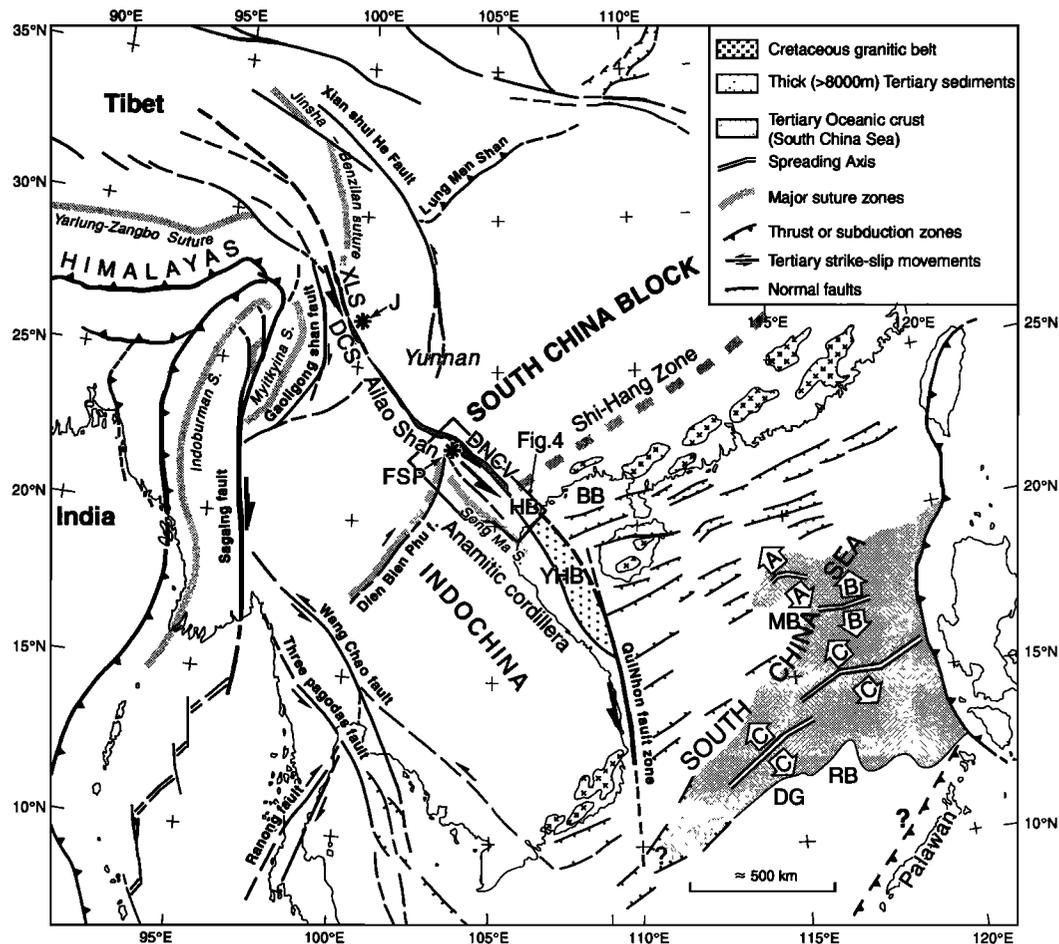
Figure 1. Structural sketch map of SE Asia. For ASRR, XLS, Xue Long Shan; DCS, Dian Cang Shan; DNCV, DayNuiConVoi. South China Sea seafloor is lightly shaded. Divergent arrows A, B, and C are the three main stages of seafloor spreading from Briais et al. [1993]. HB, Hanoi basin; BB, Beibu basin; YHB, Yingehai (or Song Hong) basin; MB, Macclesfield Bank; RB, Reed Bank; DG, Dangerous Ground. The arrows correspond to Tertiary shear senses prior to 16 Ma. Stars labeled J and FSP, correspond to the Jianchuan and FanSiPan areas respectively. Modified from *Leloup et al.*, [1995] with permission of Elsevier Science.

An extensive study of one of these great Asian strike-slip faults, the AilaoShan–Red River shear zone (ASRR, Figure 1), has been ongoing since 1990 [e.g., *Tapponnier et al.*, 1990; *Leloup et al.*, 1995] (see a review in section 5). Several important conclusions can be derived from this study: (1) Ductile deformations in the middle crust are localized in narrow shear zones capable of absorbing hundreds of km of displacement. (2) Localization continues for some tens of million years, indicating that large faults are not transient structures. (3) Localized deformation absorbs a substantial part of the Asian Cenozoic shortening. (4) Strike-slip shear zones slice the entire lithosphere and may lead to the opening of an oceanic marginal basin.

Whereas the basic observations within the ASRR shear zone have not been disputed, some aspects of the above interpretations have been questioned. The most disputed points are the total amount of displacement, its variation along strike, and the possibility of damping of some of the strike-slip motion by shortening or extension, the precise timing of shearing, the connection of the continental fault with seafloor spreading, and the process that led to localization of the shear zone (preexisting weakness or not?).

To further clarify the kinematics of the ASRR, we present new data from its NW and SE portions. These data are discussed with a particular emphasis on the disputed points mentioned above. We finally look how these results may highlight our knowledge of continental deformation.

2. Methodology

The work presented here is the result of a multidisciplinary study combining structural geology, metamorphic petrology, and $^{40}Ar/^{39}Ar$ thermochronology. Results of each of these methods have major implications for the two other ones. We think that final conclusions on the style and on the timing of deformation can only be reached by such a multidisciplinary approach. For each major structural unit we present data on the structure, petrology, and thermochronology and then a common discussion and interpretation.

2.1. Structure

To describe the ASRR structure, we combine analyses of data from plate tectonics to microscopic scale. Because very large strike-slip motion ($\approx 700 \pm 200$ km) is suspected along

the ASRR [*Leloup et al.*, 1995] Tertiary structure has to be assessed in the frame of the India/Eurasia collision, and we used published geological data covering the whole SE Asia. Our regional-scale database comprises the published geologic maps [e.g., *General Geological Department of the Democratic Republic of Vietnam*, 1973; *General Geological Department of Mines and Geology of the Socialist Republic of Vietnam* 1988; *Geological Bureau of Yunnan Province*, 1979]. We updated them with our own field observations and satellite image interpretations (Landsat and SPOT). At intermediate scale we rely mostly on our own field mapping and cross sections to describe the geometry and structure of the geologic units. At the outcrop scale we characterize the style, intensity, and geometry of deformation. For ductile rocks this requires a precise description of the foliation and lineation(s). In the case of mylonites we then measure shear criteria and select oriented samples. The main shear criteria used in this study are the geometric relationship between schistosity (S) and shear planes (C or C') [e.g., *Berthé et al.*, 1979], asymmetrical boudinage [e.g., *Lacassin*, 1988], and σ and δ porphyroclasts [e.g., *Passchier and Simpson*, 1986; *Hanmer and Passchier*, 1991]. Special attention is paid to the compatibility of structures observed in nearby places and at all scales from oriented thin sections to satellite images.

2.2. Metamorphic Petrology

A good knowledge of the P-T evolution during deformation is necessary to correctly interpret the geochronologic results in terms of deformation history. After a qualitative estimate of the deformation conditions and sample selection in the field, thin section study of the relationships between metamorphic parageneses and deformation(s) gives a better idea of the P-T conditions during deformation. For example, evidence of quartz plasticity (undulose extinction, recrystallization) indicated temperature of deformation above 300°C [e.g. *Passchier and Trouw*, 1996, p. 48]. In a second step, detailed electron microprobe analysis allowed determination of the paragenetic mineral composition and, when garnets were involved, use of thermobarometers to constrain these P-T conditions. The thermobarometers used in this study were based on the garnet-biotite (gt-bt) [*Hodges and Spear*, 1982] and the garnet-sillimanite-plagioclase-biotite-quartz (gt-sill-pl-bt-q) [*Ganguly and Saxena*, 1984] equilibria. If only one of these thermobarometers was used, the result was an equilibrium line in P-T space along which the P-T conditions of the considered paragenesis should lie. When two thermobarometers were calculated for the same paragenesis (and the same garnet composition), two independent lines were calculated and the P-T conditions correspond to the intersection between these two lines. For each thermobarometer, several equilibria using different mineral pairs were calculated using the software geothermobarometry written by M. Kohn and F. Spear (see Plate 1h, and Tables 5, A1[1] and A2[1]). Garnet chemical zoning was investigated by numerous discrete mineral analyses and, in some cases, with compositional traverses and X-ray maps. In some cases, P-T estimations were compared with the equilibrium

conditions calculated using Thermocalc [*Holland and Powell*, 1990] considering quartz-bearing reactions and actual mineral compositions (see Plate 1h, and Tables 5, A1 and A2). This comparison allows investigation of the H_2O activity assuming that $X(H_2O+CO_2)=1$ (fluid phase). Mineral analyses were performed with a Cameca Camebax microbeam electron microprobe at the Centre d'Analyses Microsonde de Paris (CAMPARIS, Paris, France). Accelerating voltage was 15 kV, beam current was ≈9.3 nA. We used a beam ≈2 μm in diameter for most minerals. For beam sensitive minerals (e.g., micas) beam diameter was enlarged to ≈10 μm. The data reduction routine employed the PAP procedure as matrix correction [*Pouchou and Pichoir*, 1991].

2.3. Thermochronology

Geochronologic samples were selected in the field based on freshness and structural context. Freshness of the minerals was checked on polished thin sections. In northern Vietnam, however, weathering is so intense that precise mapping and fresh rock sampling is often difficult and sometimes impossible.

The $^{40}Ar/^{39}Ar$ results were obtained in two different laboratories: at the Université Blaise Pascal in Clermont Ferrand, France (UBP), and at the University of California, Los Angeles (UCLA). Results obtained in these two laboratories are very consistent, precluding any systematic analytical bias. All results will be summarized in Tables 1, 3 and 6.

K-feldspar (Kf), hornblende, biotite, and white mica mineral separates were obtained using heavy liquid and magnetic separation techniques from crushed fresh hand specimens. Purity of the final mineral separates was carefully checked with a binocular microscope. Approximately 20 mg of K-feldspar and amphibole, and 5 mg of the micas were irradiated together with Fish Canyon sanidine (FC-3) flux monitors and salts, either in the Ford Reactor, University of Michigan (UCLA), or in the Mélusine reactor of the Commisariat à l'Energie Atomique of Grenoble, France (UBP). J factor was estimated assuming an age of 27.55±0.08 Ma for the Fish Canyon sanidine standard [*Lanphere and Baadsgaard*, 1997]. Various techniques were used to measure the ages of the mineral fractions: laser total fusion (UCLA), or furnace stepwise heating (UCLA and UBP). For samples treated by stepwise heating, a conventional age spectrum, from which plateau ages are calculated, and inverse isochron [*Roddick et al.*, 1980] are presented side by side to assess potential excess argon problems. If the inverse isochron age is close to the plateau age and $^{40}Ar/^{36}Ar_i$ is not significantly different from present-day $^{40}Ar/^{36}Ar$ atmospheric ratio (295.5), we consider that the plateau age is reliable. When this is not the case, we prefer to rely on the inverse isochron age if this one is well determined. For brevity, such choice will not be discussed in detail for each measurement, but all results will be shown on Tables 1, 3 and 6 (see also Figures 3, 11 and 18).

A particularly long furnace heating schedule was conducted on K-feldspar in order to retrieve diffusion characteristics, to apply diffusion models, and to calculate model thermal histories [e.g., *Lovera et al.*, 1989, 1991; *Harrison et al.*, 1991]. Comparable diffusion measurements on 115 K-feldspars revealed that their activation energies define a normal distribution with an average value of 46±6 kcal/mol [*Lovera et al.*, 1997]. In most cases we also conducted two-stage isothermal stepwise heating at low temperatures (450-800°C); the first and the second of the two isothermal stages lasting of the or-

---

[1]Supporting data tables are available via Web browser or via Anonymous FTP from ftp://kosmos.agu.org, directory "apend" (Username="anonymous", Password="guest"); subdirectories in the ftp site are arranged by paper number. Information on searching and submitting electronic supplements is found at http//www.agu.org/pubs/esupp_about.html.

der of 10 and 15 min respectively. Such heating schedule often produces a sawtooth-shaped age spectrum where the second of the two stages is systematically younger and less affected by excess argon [e.g., *Harrison et al.*, 1994]. We also systematically plotted inverse isochrons for K-feldspar. In some cases, careful interpretation of such plots, selecting linear arrays defined by several steps, may solve excess argon problems in some portions of age spectra.

Once the age of a given mineral is calculated, a fundamental and controversial issue is to determine if this age corresponds to mineral crystallization, deformation, or cooling below a given closure temperature. It appears that in most cases the $^{40}Ar/^{39}Ar$ ages correspond to cooling ages, and we choose to systematically build cooling histories from our results. This choice leaves open further discussion on the internal consistency of such cooling histories and the relationship between $^{40}Ar/^{39}Ar$ ages and deformation events. For example, $^{40}Ar/^{39}Ar$ ages of fine white micas may in fact correspond to the age of synkinematic crystallization [e.g., *Kirschner et al.*, 1996]. We have assumed closure temperatures of 320±40°C for biotites, 415±40°C for phlogopites, 390±45°C for white micas and 510±50°C for amphiboles. These closure temperatures are calculated for a wide range of cooling rates (1 to 200°C/Myr), using the formula given by *Dodson* [1973] and diffusion parameters deduced from the experimental data of *Giletti* [1974], *Hames and Bowring* [1994], *Harrison* [1981], and *Harrison et al.* [1985]. As stated above, most K-feldspars led to the calculation of a cooling history using diffusion models. When such calculation was impossible, we qualitatively considered that the lower furnace temperature (LT, 400-700°C) ages correspond to cooling at ≈150-300°C, whereas higher furnace temperatures (HT, 1000-1200°C) ages correspond to cooling at ≈300-450°C. In the same way, a well-defined plateau would correspond to a rapid cooling at these temperatures. All uncertainties are given at the 1σ confidence level.

3. The Ailao Shan-Red River Shear Zone (ASRR)

The Red River zone is the major physiographic and geological discontinuity in East Asia. It stretches for more than 1000 km from Tibet to the Hanoi basin and separates the Indochina and South China (SC) continental Blocks (Figure 1). This zone is the result of at least two successive phases of deformation [e.g., *Tapponnier et al.*, 1986; *Leloup et al.*, 1995]. The most recent phase corresponds to right-lateral/normal movements along the Red River fault [e.g., *Tapponnier and Molnar*, 1977; *Allen et al.*, 1984; *Leloup et al.*, 1995]. Total right-lateral offset has been estimated between 6 [*Allen et al.*, 1984] and 60 km [*Leloup et al.*, 1995], whereas the most probable value appears to be 25 km [*Replumaz et al.*, 2000]. Such right-lateral/normal motion began at 5 [*Leloup et al.*, 1993] to 13 Ma [*Bergman et al.*, 1997], and is partly responsible for the denudation of an older shear zone: the Ailao Shan-Red River (ASRR).

Whereas the existence of the ASRR has long been denied [e.g., *Cobbold and Davy*, 1988; *Dewey et al.*, 1989; *Houseman and England*, 1993] or minimized [e.g., *Rangin et al.*, 1995], many extensive studies have proven its importance in SE Asia tectonics [*Tapponnier et al.*, 1990; *Schärer et al.*, 1990, 1994; *Briais et al.*, 1993; *Harrison et al.*, 1992,

1996; *Leloup and Kienast*, 1993; *Lacassin et al.*, 1993; *Leloup et al.*, 1993, 1995; *Zhang*, 1995; *Zhang and Schärer*, 1999]. The ASRR is composed of four narrow (<20 km wide), high-grade gneiss ranges: the DayNuiConVoi (DNCV) in northern Vietnam and the Ailao Shan, Diancang Shan (DCS), and Xuelong Shan (XLS) in the Chinese province of Yunnan (Figure 1). Strongly foliated and lineated mylonitic gneisses compose the cores of these metamorphic ranges. The mylonitic foliation is generally steep and bears a horizontal stretching lineation, both being almost parallel to the local trend of the gneissic cores [e.g., *Tapponnier et al.*, 1990]. In some places, foliation dips more gently, but lineations are always horizontal and parallel to the trend of the belt [e.g., *Leloup et al.*, 1995]. Numerous shear criteria indicate that the gneisses have undergone intense, progressive left-lateral shear [e.g., *Leloup et al.*, 1995]. Petrologic studies show that left-lateral strain occurred in the Ailao Shan and Diancang Shan ranges under a very high geothermal gradient, from amphibolite facies (3-7 kbar and 550-780°C) to greenschist facies (<3.8 kbar and 500°C) conditions [e.g., *Leloup et al.*, 1993; *Leloup and Kienast*, 1993]. In all ranges, high-temperature shear was coeval with felsic magmatic activity that lasted at least from 33 to 22 Ma [*Schärer et al.*, 1990, 1994; *Zhang and Schärer*, 1999]. The $^{40}Ar/^{39}Ar$ data indicate that the Ailao Shan and Diancang Shan mylonites rapidly cooled during the lower Miocene, before the end of left-lateral motion [*Harrison et al.*, 1992, 1996; *Leloup et al.*, 1993]. In the Ailao Shan this cooling is diachronous along strike: it occurs at 22 Ma at YuanYang, close to the Vietnamese border, and at 17 Ma near the NW tip of the range. Total left-lateral offset on the ASRR is estimated at 700±200 km [e.g., *Leloup et al.*, 1995; *Chung et al.*, 1997], whereas paleo-slip rate estimates range between 3 and 5 cm/yr [*Briais et al.*, 1993; *Leloup et al.*, 1995; *Harrison et al.*, 1996].

In the field, deformation fabrics related to left-lateral shear are very clear in the Ailao Shan belt (Figure 1). This deformations is less spectacular at both ends of the Ailao Shan. To the northwest, ductile mylonitic rocks only crop out in the DianCang Shan and XueLong Shan ranges at the footwall of active normal faults, and the large-scale geometry of the shear zone has been affected by oroclinal bending due to the proximity of the Eastern Himalayan syntaxis. To the southeast the shear zone splits into several branches and is intruded by large granitoid bodies before disappearing below the Quaternary deposits of the Hanoi basin (Figure 1). There the geometry and kinematics of the shear zone and its connection with the YingeHai basin and the South China Sea have not been described and discussed in details mainly because the shear zone is buried by >1-10 km of post-Pliocene deposits.

In this paper we first present new geochronological results from the northwesternmost range of the ASRR: the XueLong Shan. Then we synthesize new structural, petrologic, and geochronologic results that constrain the structure of the ASRR across northern Vietnam up to the South China Sea shore. According to published geological maps of northern Vietnam [e.g., *GGDDR Vietnam*, 1973] the Ailao Shan range can be traced across the China/Vietnam border toward the FanSiPan region, south of the Red River valley (Figure 1). Toward the SE, another large metamorphic range stretches on the other bank of the Red-River: the DayNuiConVoi (DNCV, Figure 1). We successively present data from these three structural units.
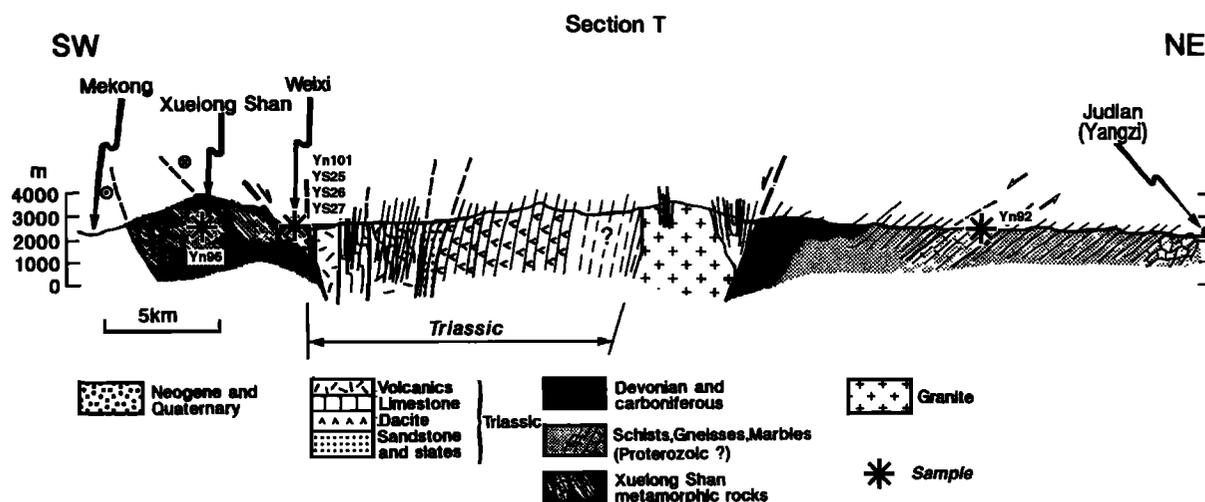
Figure 2. Section of northwestern ASRR accross XueLong Shan range (see location on Figure 1). Simplified from Figure 9b of *Leloup et al.* [1995] with permission of Elsevier Science.

4. The XueLong Shan Range

4.1. Structure and P-T Conditions of Deformation

Preliminary results on the structure of the XueLong Shan (XLS) were presented by *Leloup et al.* [1995]. These results were based on previous geological mapping [*Bureau of Geology and Mineral Ressources of Yunnan*, 1984a], and on a section near the southern tip of the range (section T, Figure 2). They can be summarized as follows : (1) The NE edge of the XLS range corresponds to an active normal fault. (2) This fault, marked by a ≈1 km cataclasite zone, separates vertical slices of volcanic and sedimentary Triassic rocks from the core of the range which is composed of mylonitic micaschists and gneisses (Figure 2). (3) The schists and gneisses exhibit a foliation striking ≈N160° E and dipping ≈40° E and a nearly horizontal lineation striking N170° on average. (4) Numerous shear criteria indicate that deformation was highly noncoaxial and that shear was top (east side)-to-the-north and thus compatible with a left-lateral movement on the ASRR.

The mica-schists contain numerous amphibolite, pegmatite, and quartz boudins. Some pegmatitic dikes are less deformed and crosscut the sinistral fabric. Rock thin sections show evidences for intense ductile deformation with strong quartz recrystallization suggesting left-lateral deformation temperatures above 300°C. The highest-grade rocks reached along section T are migmatitic paragneiss.

4.2. Thermochronology of the XueLong Shan Range

Sample Yn96 is a micaschist from the metamorphic core of the range (Figure 2). It contains quartz ribbons, biotite, muscovite, and K-feldspar porphyroclasts. The ^{40}Ar/^{39}Ar measurements on biotites of this sample yield an inverse isochron age of 26.3±0.6 Ma associated with some excess ^{40}Ar (Figures 3a and 3b, and Table 1). As we obtained only a few fresh samples along section T, we also sampled fresh gneiss boulders in the Weixi basin at the foot of the range (Yn101, YS25, YS26, and YS27, Figure 2). Yn101 is a two-mica orthogneiss which muscovites yield an inverse isochron age of 29.9±0.6 Ma

(Figures 3c and 3d, Table 1). Such an age is compatible (i.e., slightly older) with the Yn96 biotite age.

Other boulders from the same locality have been dated by U/Pb and Rb/Sr methods. YS25 is an orthogneiss crosscut by a leucocratic layer (YS26). The leucocratic layer contains Ti-U oxides that have a concordant U/Pb age of 33.1±0.2 Ma (±2σ) interpreted as the time of crystallization of the leucocratic layer [*Zhang and Schärer*, 1999]. The gneiss itself (YS25) contains allanite and zircons that show U/Pb lower intercepts of 56±7 Ma and 213±2 Ma (±2σ) respectively [*Zhang*, 1995]. YS25 biotites and muscovites show Rb/Sr ages of 28.9±0.6 and 52.6±1.1 Ma respectively [*Zhang and Schärer*, 1999]. Allanite and titanite from another orthogneiss (YS27) give Early Tertiary U/Pb ages of 59.1±0.3 and 64±6.1 Ma, respectively (±2σ) [*Zhang*, 1995]. YS26 apatites yield a fission track age of 2.7±0.6 Ma (±1σ) with long track length of 14.57±1.07 μm indicating rapid Pliocene cooling through 60-120°C [*Bergman et al.*, 1997].

The only other gneisses cropping out along section T form a west dipping slice 30 km east of the XLS, within low-grade schists mapped as Proterozoic (Figure 2). Yn92 sampled within these gneisses contains shear criteria suggesting a top-to-the-west (normal) shear. Yn92 muscovites yield a plateau age of 228±4 Ma (Figures 3e and 3f, Table 1).

These data are still sketchy but give some important constrains on the tectono-thermal history of the XLS region (Figures 3g and 3h). (1) The area presently cropping out east of XLS probably suffered a tectono-metamorphic event during the upper Triassic (≈210 to 230 Ma). (2) The XLS range suffered at least two periods of granite emplacement: the first one in the Early Tertiary (70 to 55 Ma) and a second one at ≈33 Ma. (3) Leucocratic layers emplaced at ≈33 Ma where later deformed within the ASRR, and in the XLS, such ductile deformation lasted until ≈26 Ma. (4) Final rapid cooling and hence probably denudation of the XLS occurred since ≈3 Ma.

5. The FanSiPan Range

The FanSiPan (FSP) range is a rugged area culminating at 3143 m elevation near the Sino-Vietnamese border (Figures 1,
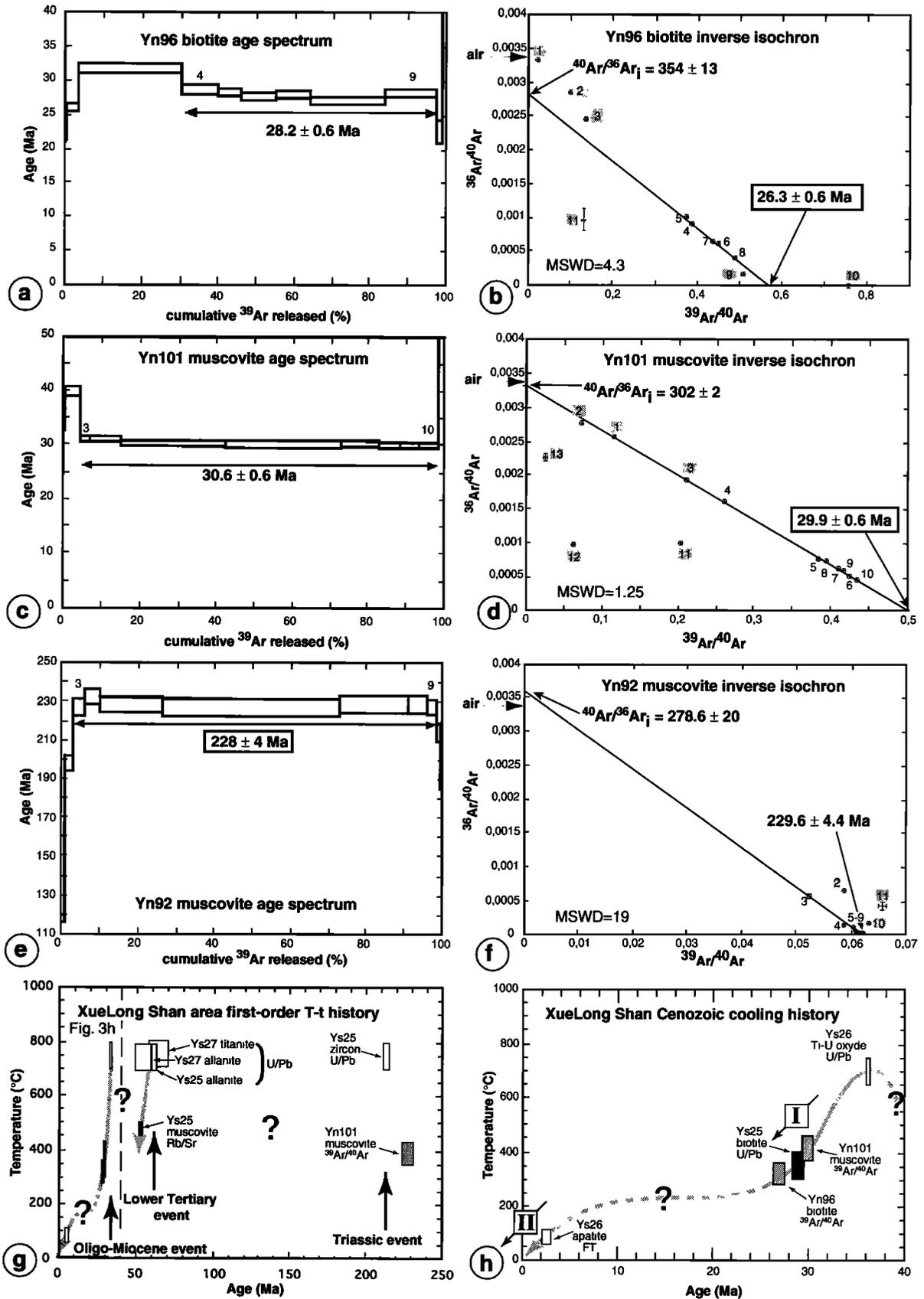
Figure 3. The $^{40}Ar/^{39}Ar$ data from the XueLong Shan range. Results are summarized in Table 1, and samples located on Figure 2. (a, c, e) Conventional age spectra. (b, d, f) Inverse isochrons for which each step is plotted with the corresponding error bars and step number, the drawn regression line corresponds to the calculated age and $^{40}Ar/^{36}Ar_j$. Step numbers in shaded boxes were not used for calculations. Preferred ages are framed. (g, h) Xuelong Shan area first order temperature-time (T-t) history. Rb/Sr and U/Pb results are from *Zhang* [1995] and *Zhang and Schärer* [1999]. Figure 2g is a zoom of the Oligo-Miocene history. Large shaded line represents preferred T-t history. The I and II refer to main Tertiary cooling phases.

Table 1. XueLong Shan Range $^{40}Ar/^{39}Ar$ Results

Section/Site	Sample					Plateau Age		Inverse Isochron Age				Reference
	Number	Mineral	Size (μm)	Lab[a]	Location	Age, Ma	Steps	Age, Ma	$^{40}Ar/^{36}Ar_i$	MSWD[c]	Steps	
Section T of Leloup et al. [1995]	YN96	biotite	125-400	UBP	=27°00'40"N =99°19'48"E Figures 1 and 2	28.2±0.6[b]	67%of gas 6 steps/11 (4-8)	26.3±0.6[b]	354±13	4.3	53%of gas 5 steps/11 -(1-3,9-11)	this study
Boulder in WeiXi basin	YN101	muscovite	250-400	UBP	=27°09'07"N =99°19'11"E Figures 1 and 2	30.6±0.6	95%of gas 8 steps/13 (3-10)	29.9±0.6[b]	302±2	1.3	91%of gas 7 steps/13 -(1-3,11-13)	this study
30 km east of the range along section T of Leloup et al. [1995]	YN92	muscovite	125-400	UBP	=27°12'23"N =99°34'12"E Figures 1 and 2	228.2±4.3[b]	95%of gas 11 steps/13 (3-9)	229.6±4.4	278.6±20	18.7	95.4%of gas 11 steps/13 -(1,2,10,11)	this study

[a]UBP, Université Blaise Pascal, Clermont Ferrand.
[b]Preferred age.
[c]MSWD, mean square weighted deviation.

4 and 5; see also Figure 10g). It is mainly composed of granites and metamorphic rocks (gneisses, schists, and marbles). According to Vietnamese and Chinese geological maps [e.g., *BGMR Yunnan*, 1983, 1984b; *GGDDR Vietnam*, 1973; *GDMGSR Vietnam*, 1988] these metamorphic rocks extend parallel to the Red River fault zone in the direct extension of the Ailao Shan range, southern part of the ASRR in China [e.g., *Leloup et al.*, 1995]. The large FSP potassic granite batholith (YeYenSun complex of *GGDDR Vietnam*, [1973]) bounds the metamorphic rocks to the south (Figure 5). This batholith is composed of several magmatic units reported to range in age from Cretaceous to Eocene [*Izokh et al.*, 1964; *GGDDR Vietnam*, 1973]. Geologic map relationships between the granitoids and the metamorphic rocks are not obvious. Locally, the batholith seems to crosscut the schists and gneisses of the ASRR. On the other hand, it is clearly elongated parallel to the ASRR and affected by a large-scale left-lateral shear plane (Figures 4 and 5). This suggests that the batholith is syntectonic to left-lateral shear parallel to the ASRR. To the southeast, the FSP granite intrudes the large Mesozoic TuLé volcanic unit and the associated intrusive bodies (Figure 4), [*GGDDR Vietnam*, 1973]. Twenty kilometers SW of the FSP granite outcrops the PuSamCap igneous alkaline complex reputed to be Paleogene in age [e.g., *GGDDR Vietnam*, 1973] (Figure 5). Most ages are based on K-Ar work performed in USSR in the 1960s [*Izokh et al.*, 1964] whose original data have not been published.

5.1. Structure of the FSP Range

We have performed field work in the FSP range mostly along two cross sections: near BatXat (section A, Figures 4 and 5), and between LaoCay and the ThanUyen basin (section B, Figures 4 and 5). These sections are completed by several observations along the Red River valley and the roads BaoHa-VanBan-ThanUyen and YenBai-NghiaLo-Tulé-ThanUyen (Figure 4).

5.1.1. BatXat section (section A).
This section exhibits clear evidence of left-lateral deformation along the ASRR. A NW-SE morphological discontinuity, clear on SPOT satellite image, corresponds to an active normal/right lateral fault that separates the section into two parts (Figures 5 and 6). NE of this fault, schists and mylonitic orthogneisses and paragneisses crop out, whereas to the SW the section is almost exclusively composed of orthogneisses in which deformation decreases toward the SW (Figure 6). All along the section, the rocks show a steep NW-SE (N150°E on average) foliation marked by the preferential orientation of biotites and sometimes muscovites and, in many sites (e.g., sites A7 and A8, Figure 6), by a mylonitic banding (Figure 7a). In all sites, the foliation bears a nearly horizontal stretching lineation (Figures 7b and 8a). On horizontal sections (i.e., parallel to lineation and perpendicular to foliation), the orthogneisses have C/S structures. The shear planes (C) often bear nearly horizontal striations (Figure 8a) and constantly trend more easterly (N125°E on average) than the foliation (S), testifying for a constant component of left-lateral shear in the deformation of these rocks (Figures 7c, 7d, and 8a). A closer look reveals several types of shear planes: Some are penetrative and stand at an acute angle (0 to 25°) to the foliation, whereas others are more discrete and stand at a larger angle (25°-35°). In the upper part of the section (SW) the gneisses apparently abut against a range of marbles and were probably thrust on these marbles along a late NW-SE reverse fault (Figure 5).
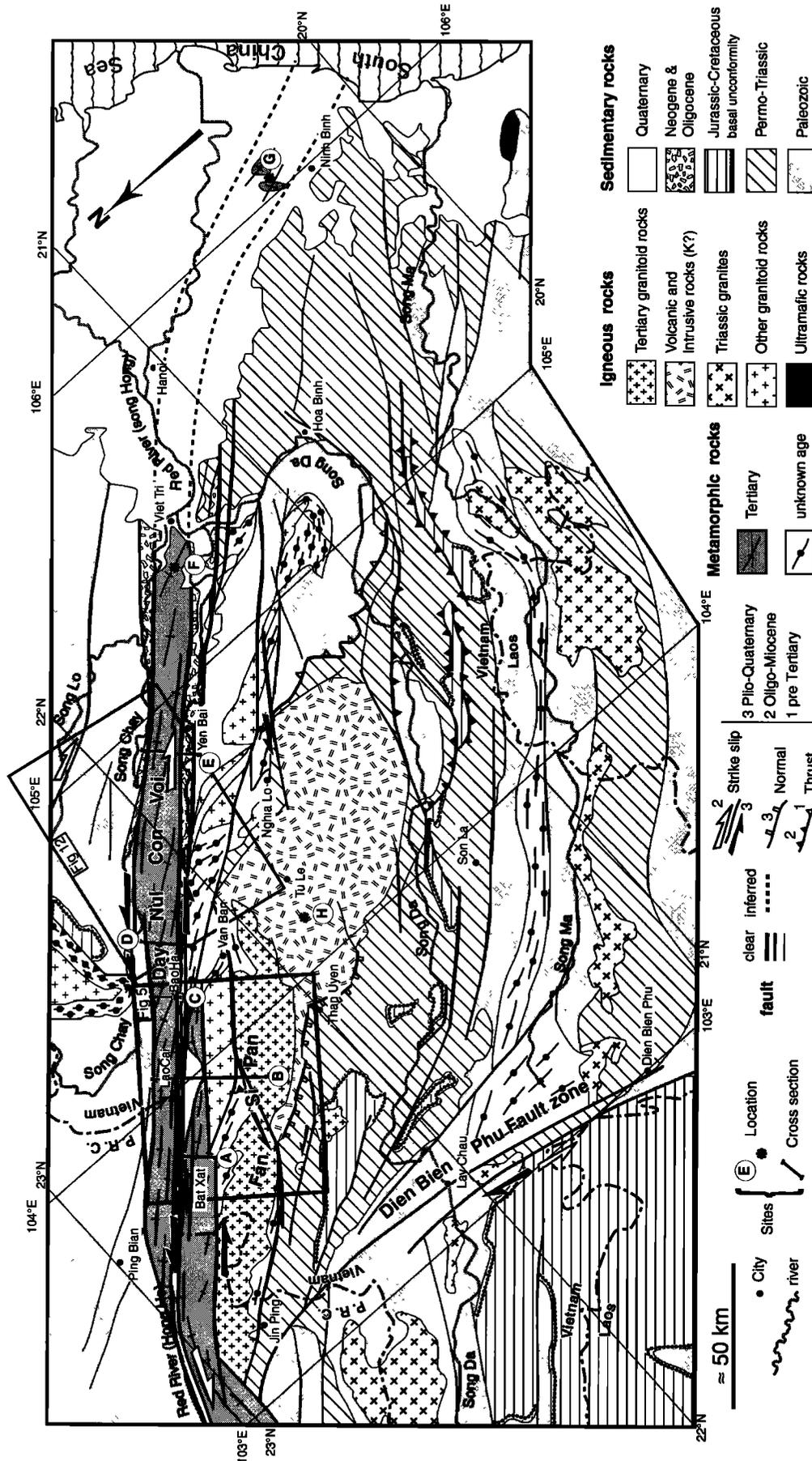
Figure 4. Structural map of northern Vietnam (framed area on Figure1) based on geological maps at 1/1,000,000 scale [e.g., GGDDR Vietnam, 1973, GDMGSR Vietnam, 1988, ; BGMR Yunnan, 1983], satellite image interpretations (SPOT and Landsat), and field observations. Figures 5 and 12 locations are indicated.

Figure 5a. Mosaic of four portions of SPOT satellite image of LaoCay area.

5.1.2. LaoCay-SaPa-ThanUyen section (section B). The road from LaoCay to SaPa and to the ThanUyen basin offers a splendid section across the main FSP range (Figure 9a). We describe our observations along this section from NE to SW.

Southwest of the Red River, folded epimetamorphic schists and marbles crop out (Early Paleozoic according to geological maps). They are cut by several strands of the active right-lateral Red-River fault [*Replumaz et al.*, 2000], (Figure 5). The southwest edge of the valley corresponds to en échelon right-lateral/normal active faults (Figures 5 and 9a). These faults bound the PoSen batholith, which is composed of plagiogranite, adamellite, granodiorite, and migmatite [*Tran et al.*, 1979]. According to *Tran et al.* [1979] the metamorphic grade in the Paleozoic series of the Red River valley increases toward this batholith which is mapped as Upper Palaeozoic. Along the LaoCay-SaPa section, the granite is affected by a mild penetrative deformation. Low-temperature brittle/ductile shear zones marked by chlorite-bearing planes crosscut the granite (Figure 9a). Near the active normal fault bounding the granite to the NE (e.g., site B1) the shear zones dip to the NE and show evidence of normal deformation (Figure 10a), whereas in the core of the granite they are close to vertical and left-lateral (site B2, Figure 10b). Along the SW margin of the granite the C/S orthogneiss result from a more ductile deformation. There foliation strikes NW-SE and dips 90° to 40° toward the NE. The stretching lineation is nearly horizontal (sites B3 and B4), (Figures 5, 8b, 9a, and 10c). Shear planes

strike more easternly than the foliation indicating a left-lateral component of shear (Figure 8b and 10d).

Gneisses, schists and marbles crop out between the PoSen and the FSP batholiths (Figures 5 and 9a). These rocks belong to two structural units: the SaPa nappe and the FSP metamorphics. The SaPa nappe has a spoon-like shape: its flat base becomes steep to the SE (Figure 9 and 10e). The nappe mainly consists of marbles that either trend NW-SE or are nearly flat. In both cases they show a NW-SE trending lineation (Figure 8c). Meter-scale amphibolite boudins crop out at the sole of the nappe (Figure 9a). The SaPa nappe overthrust the FSP metamorphics which are affected by a large-scale N165 trending fold visible on SPOT image (Figures 5 and 8d). The FSP metamorphics contain schists, gneisses, and marbles. Some of these rocks show a mild lineation that is nearly dip slip (Figure 8c). After rotation about the fold axis, these lineations trend ≈E-W. These lineations and their later folding could result from progressive deformation during an ≈E-W shortening phase. The fold was later overthrust by the SaPa nappe, whith direction of movement parallel to the direction of left-lateral shear in the nearby margin of the PoSen granite (Figures 5 and 8c).

The FSP batholith appears to intrude the FSP metamorphics but is often separated from them by an active, NE dipping normal/right-lateral fault (Figures 5, 9, and 10e). According to *Tran et al.* [1979], the FSP batholith corresponds to the alkaline YeYenSun complex, which contains amphibole-bearing biotite granosyenite and granites and was formed by at least
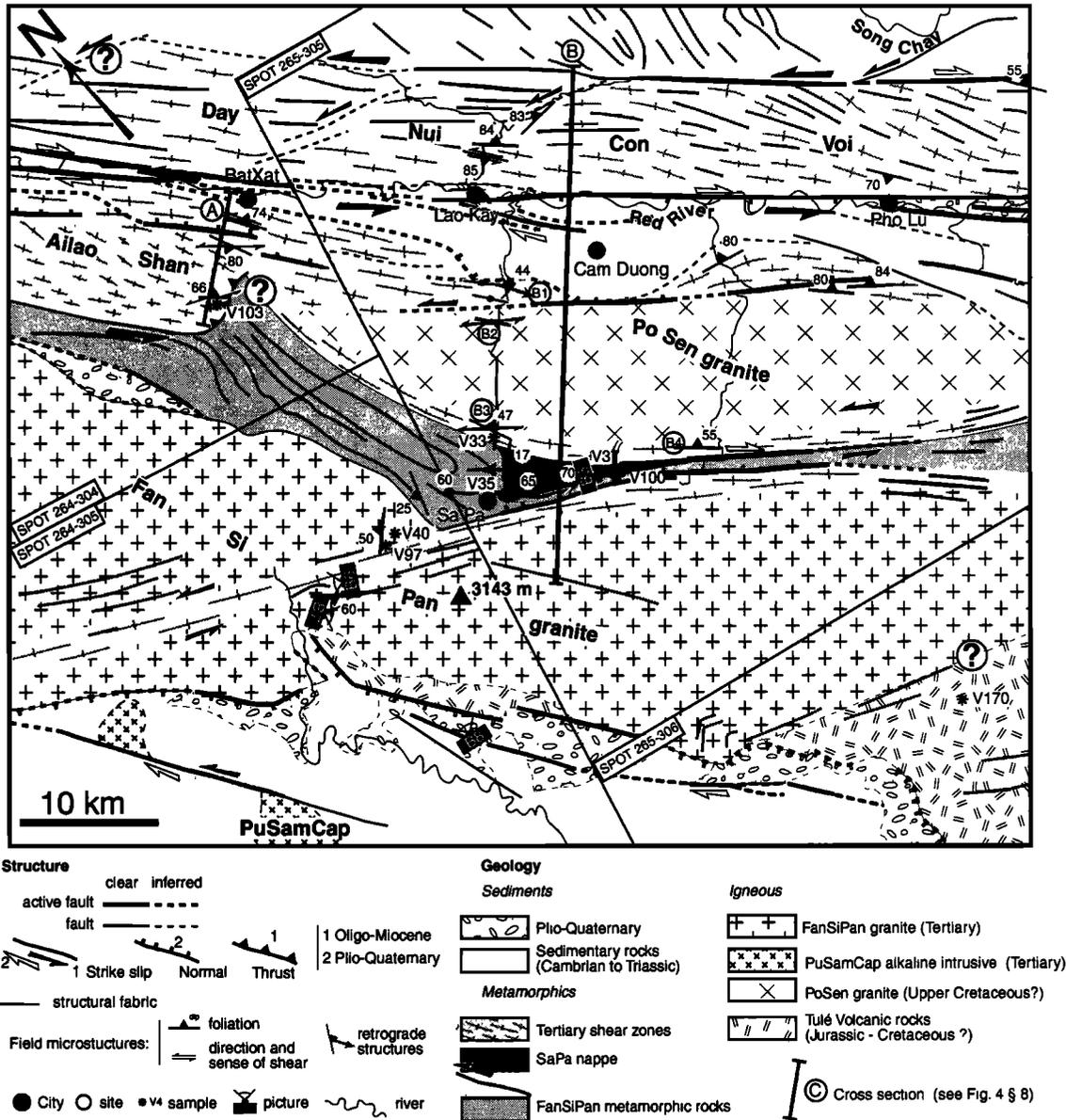
Figure 5b. Structural map of LaoCay area (NW Vietnam) and southern Yunnan (China) showing FanSiPan and northern DayNuiConVoi ranges. Drawn from satellite images (Figure 5a) interpretation and field observations. Sites and samples discussed in text are located, as well as cross-sections A (Figure 6) and B (Figure 9a).

six magmatic phases, the last ones corresponding to aplite and pegmatite intrusion. Published K-Ar ages on biotite and amphibole range between 41 and 72 Ma [*Izokh et al.*, 1964]. Although not affected by strong penetrative deformation, the granite locally shows a crude NW-SE trending foliation (Figure 8e). This foliation can be seen in the landscape along the left-lateral fault that offset the granite by ≈20 km (e.g., site B6, Figures 5 and 10f). Some late leucocratic dikes crosscut the foliation, whereas others are foliated, suggesting a syntectonic emplacement of these dikes. The FSP granite is also affected by late chlorite shear zones comparable to those affecting the PoSen batholith. To the south, geological maps show the FSP batholith crosscuting granitoids of the PhuSaPhin complex (see section 5.1.3). To the SW, the FSP range ends with a steep slope. Clear triangular facets and deep

canyons attest that this slope is the morphological expression of an active normal fault (Figure 5, Figure 10h). Below the Quaternary basin at the foot of the normal fault, Triassic sediments crop out and are unconformably overlain by red sandstones of supposed Cretaceous age [e.g., *GDMGSR Vietnam*, 1988]. These sandstones and their basal unconformity were intruded by the PuSamCap igneous alkaline complex (Figure 5). The Paleogene age of this complex seems to be confirmed by an imprecise $^{40}Ar/^{39}Ar$ whole rock age of a cocite sample (≈30 Ma [*Chung et al.*, 1997]). We note that a NW-SE left-lateral fault cuts and offsets the PuSamCap complex by ≈15 km (Figure 5).

5.1.3. The TuLé volcanic and intrusive rocks. A large zone of central North Vietnam (≈4000 km^2) is covered by the TuLé volcanic complex (Figure 4). The volcanic rocks
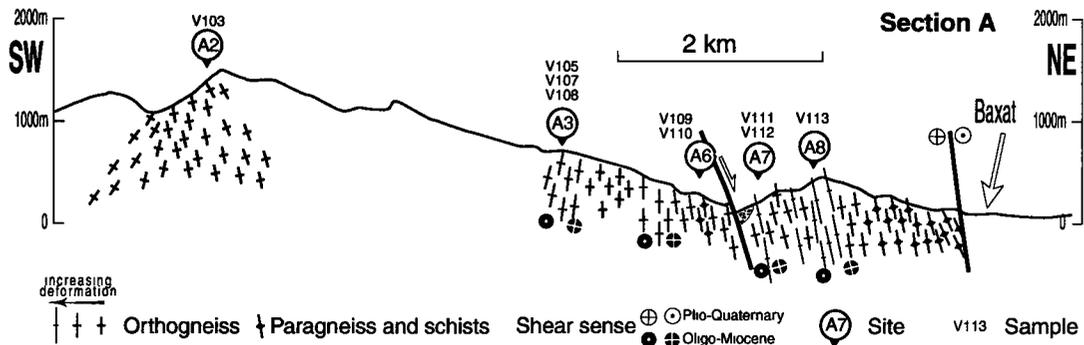
Figure 6. BatXat cross section (section A), located on Figure 5b, showing samples and sites discussed in text. Corresponding foliation and lineation attitudes are plotted on Figure 8a.

have various compositions: basaltic flows (mapped as Jurassic), rhyolites and trachytes (mapped as Cretaceous) intercalated with tuffs, and sandstones. These rocks are intruded by basic igneous rocks of the MuCangChai complex (gabbrodiabase, gabbrodiorite, pyroxene- and/or hornblende-bearing diorites, lamprophyres) and by acid igneous rocks of the PhuSaPhin complex (quartz syenite, alkaline, and subalka-

line granite) that have yielded biotite and hornblende K-Ar ages from 81 to 108 Ma [*Tran et al.*, 1979]. At a regional scale the TuLé volcanic complex does not seem to be affected by deformation related to the Red River fault zone, from which it is separated by gneisses and schists (Figure 4). Most volcanic rocks are, indeed, not deformed. However, several rocks show mylonitic fabrics as previously mentioned by *Deprat* [1914,
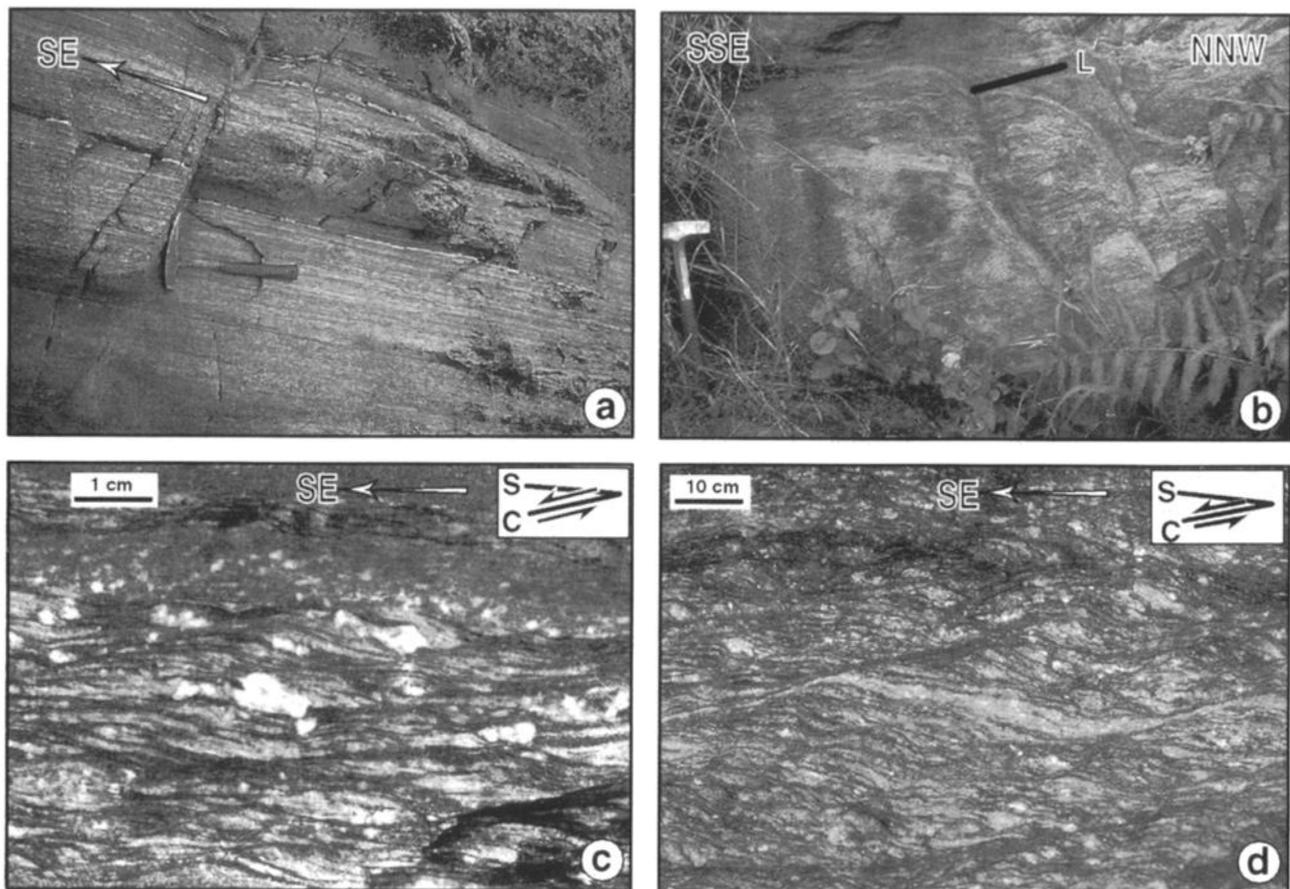
Figure 7. Field observations along BatXat section (section A, Figure 6). (a) Well-banded mylonites at site A8; foliation strikes N145° (view from above, hammer gives scale). (b) Steep foliation (N159°, 83°W) and sub-horizontal stretching lineation (pitch 18S) at site A3 (hammer gives scale). (c) Polished slab of sample V106 showing left-lateral C/S structures at site A3 (view from above). (d) Late left-lateral C/S structures at site A3 (view from above).
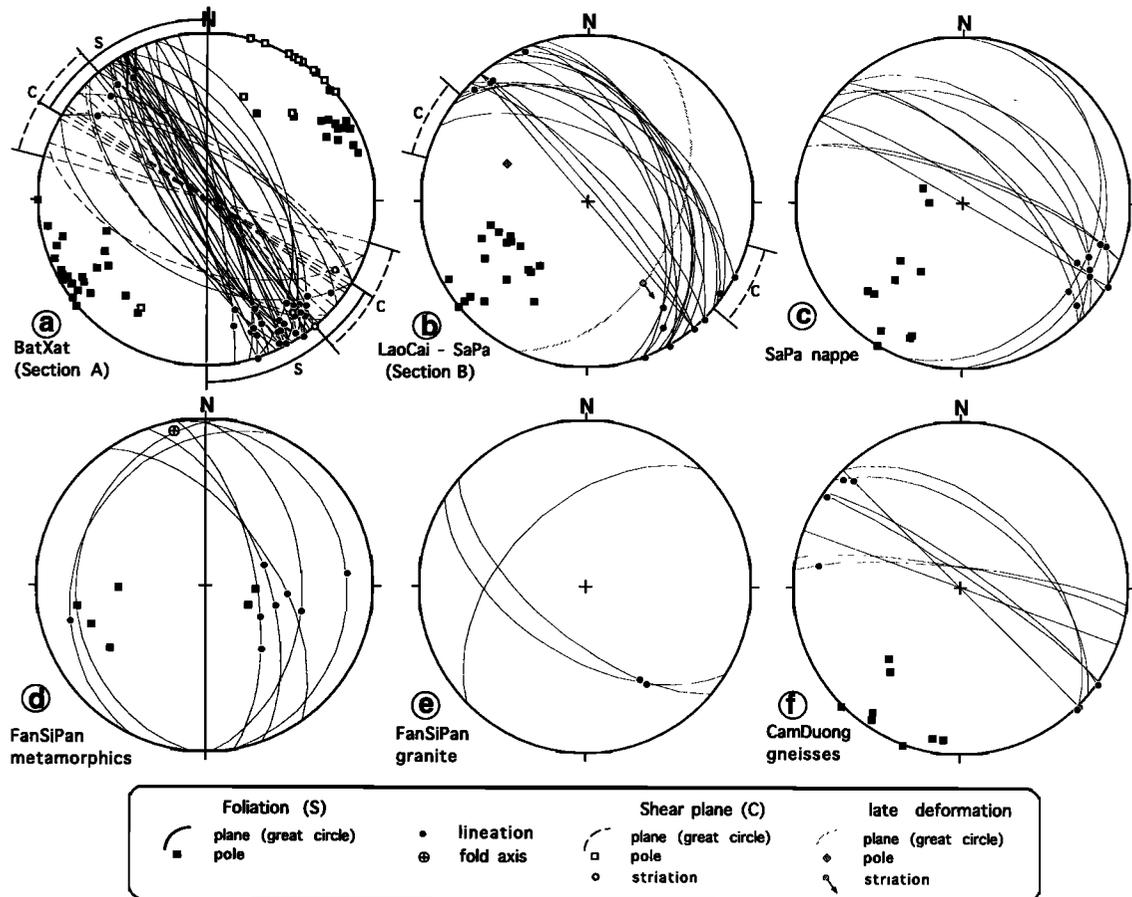
Figure 8. Structural data from FanSiPan range (Schmidt diagram lower hemisphere). (a) Batxat section (section A, Figures 5 and 6), 37 foliations, 34 lineations, and 12 shear planes (shaded). (b) Laocai-Sapa section (sites B1 to B4, Figures 5 and 9a), 19 foliations and 13 lineations. (c) Sapa thrust (Sapa nappe, Figures 5 and 9a), 11 foliations, and 8 lineations. (d) FanSiPan metamorphics (FSP metamorphics, Figures 5 and 9a), 9 foliations and 6 lineations. (e) FanSiPan granite, 3 foliations and 2 lineations (Figure 5). (f) CamDuong area (Figure 5), 8 foliations and 7 lineations.

p.65]. According to *Tran et al.* [1979], shallow intrusives are often associated with shear zones, especially near the margins of the Tulé complex.

## 5.2. P-T Conditions of Deformation in the FSP Range

Because of lack of fresh metapelitic rocks, the degree of metamorphism is difficult to ascertain. Along the BatXat section, most rocks are orthogneisses containing quartz, K-feldspar, plagioclase, biotite, often titanite and epidote, and sometimes green hornblende (Table 2). The mylonitic foliation probably formed at relatively high temperature (>300°C) as it contains quartz ribbons, biotite, and sometimes muscovite. However, retrograde recrystallization is important: chlorite and sericite mark many C and C' shear planes (Figures 7c and 7d). Minerals defining the high-temperature lineation are often brittlely stretched in the same direction. This suggests, as in the Ailao Shan [*Leloup and Kienast*, 1993], a continuum of strike-slip deformation from temperatures above 300°C to low temperatures.

In the PoSen granite both normal and left-lateral chlorite-bearing shear zones probably correspond to low-grade deformation conditions (T<300°C). Temperature seems to have

been higher for the left-lateral deformation at the western edge of the range where quartz and feldspar show recrystallization during left-lateral deformation.

In the SaPa nappe the foliation is underscored by phlogopite and white micas, suggesting temperature conditions higher than 300°C during deformation. Crosscutting phlogopite crystals suggest that such temperatures were maintained after deformation.

5.3. Thermochronology of the FSP Range

The $^{40}Ar/^{39}Ar$ results obtained in the FSP range are summarized in Table 3 and Figure 11.

5.3.1. BatXat section. V103 is a midly deformed orthogneiss from the SW of the BatXat section (Tables 2 and 3b and Figure 6). K-feldspar from this sample yields an age spectrum that exhibits a plateau age of 25.1±0.1 Ma between 10 and 30% of gas release (LT, Table 3 and Figure 11a). Then the ages rise progressively up to ≈50 Ma with a small plateau at 34.6±0.3Ma (HT, Table 3 and Figure 11a). The experimental Arrhenius diagram can be satisfactorily fit with a diffusion model assuming eight domains sharing a common activation energy of 47.3 Kcal/mol (Figure 11c). The best cooling model shows two rapid cooling phases at 41 Ma and 25 Ma separated
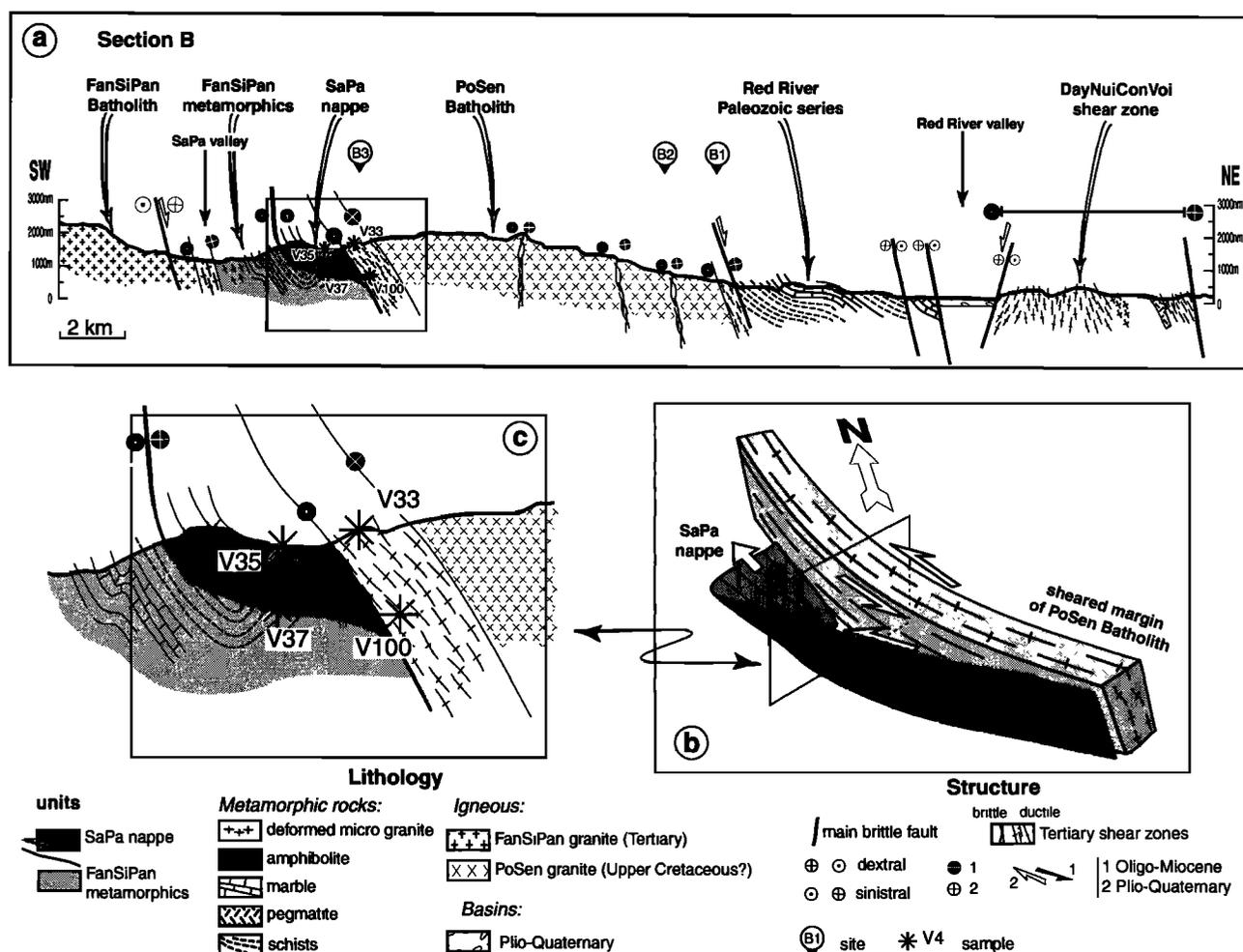
Figure 9. (a) LaoCay-Sapa cross section (section B, Figure 5). Drawn from geological map [*General Geological Directorate of Vietnam*, 1978] and field work. (b) Schematic 3-D representation of SaPa nappe. See also Figures 8b and 8c. (c) Zoom of the SW border of the Posen granite and SaPa thrust.

by an isothermal period at ≈285°C (Figures 11a and 11d). The age of the oldest cooling event is poorly constrained as it is impossible to obtain a perfect fit for the oldest part of the age spectrum. The inverse isochron suggests that all high temperature steps (27-36) are affected by excess argon (Table 3 and Figure 11b). The K-feldspar could thus contain two argon reservoirs, ≈25 and ≈34 Ma old, respectively, and possibly indicate two rapid cooling events at those times (LT and HT, Figure 11d). Biotites give a total laser fusion age of 28.1±0.1 Ma compatible with the cooling history deduced from the K-feldspar (Figure 11d).

We note that biotites from VN105, sampled nearby in the Red River valley (Figure 5), yield a plateau age of 28.4±1 Ma [*Maluski et al.*, 2000], very close to V103 biotite age and compatible with V103 K-feldspar model cooling history (Figure 11d).

5.3.2. LaoCay -SaPa (section B). We dated samples from the PoSen and FSP granites and numerous samples from the SaPa nappe.

5.3.2.1. PoSen batholith: Sample V33 comes from the sheared SW margin of the PoSen granite (site B3, Tables 2 and 3 and Figures 5, 9a and 10c). K-feldspar shows an age spectrum starting in a classical sawtooth fashion for two-

stage isothermal stepwise heating (Figure 11e). We were, however, unable to correct these steps by "chlorine cleaning" [*Harrison et al.*, 1994] or with the inverse isochron approach. An age estimate for this low-temperature part of the spectrum is thus deduced from the mean of the second isothermal stages: 22±0.4 Ma (LT1, Table 3 and Figures 11e and 11f). After 15% of gas release the ages of the isothermal stages converge, and an inverse isochron suggests an age of 26.7±0.5 Ma (LT2, Table 3 and Figures 11e and 11f). Then the ages rise until a small plateau at 88.6±1.7 Ma (HT, Table 3 and Figures 11e and 11f). We were unable to calculate a diffusion model that could correctly fit the data. Biotites give an inverse isochron age of 34.2±0.7 Ma, calculated for all heating steps except the first and last ones (82% of gas, Table 3, Figures 11g and 11h). The oldest significant age for the K-feldspar is 89 Ma. This suggests that V33 did not undergo temperatures higher than ≈400°C since at least the Late Cretaceous. The biotite age suggest temperatures of ≈300°C at ≈34 Ma. After this date the sample possibly suffered two rapid cooling episodes at low temperatures at ≈27 (LT2) and ≈22 Ma (LT1) (Figure 11r).

V100 was sampled from a large boulder derived from the SW margin of the PoSen batholith (Figure 5). This sample is less weathered than samples of the same facies taken in place at
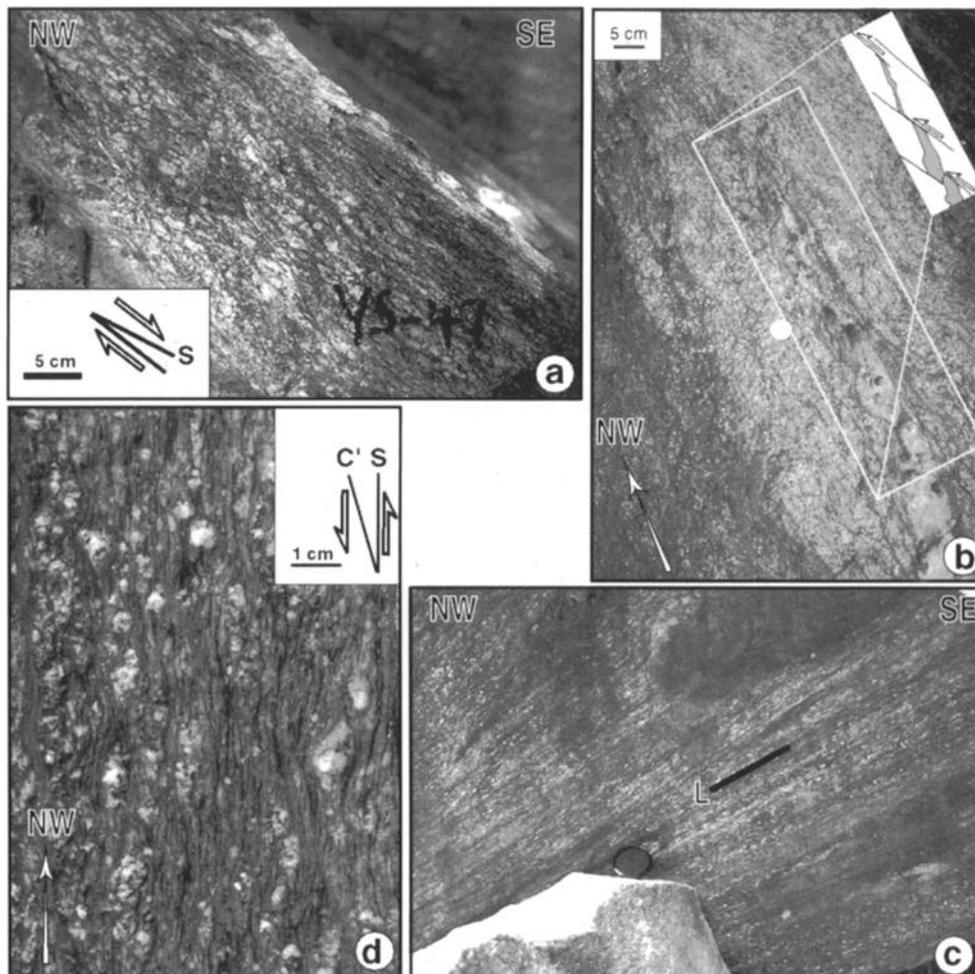
Figure 10. Field observations along LaoCay-SaPa section (section B) and in FanSiPan granite (sites located on Figures 5 and 9a). (a) Late C/S structures at site B1, indicating dextral/normal shear along NE margin of PoSen granite. (b) Late, low-temperature chlorite left-lateral shear zones at site B2 (view from above, coin gives scale). (c) Foliation (N125°,50°N) and sub horizontal stretching lineation (pitch 10W); site B4 , lens cap gives scale. (d) Penetrative, left-lateral C/S structures at site B3 (view from above, lens gives scale). (e) (top) Landscape and (bottom) interpretation drawing of SaPa valley; view from site B5 toward NW. (f) Foliation affecting the FanSiPan granite in a large-scale sinistral shear plane (view from site B6 toward NW, Figure 5). (g) Granite needles of FanSiPan range (view from site B7 toward NE). (h) Steep SW front of Fansipang range. Large triangular facets and wine glass canyons attest for active normal faulting (view from site B8 towards NW).

site B4. Biotites from V100 yield a flat age spectrum and an inverse isochron age of 32.4±0.7 Ma (Table 3 and Figures 11i and 11j).

5.3.2.2. SaPa nappe: An inverse isochron on all steps of phlogopites from V35 marble (Figures 5 and 9) gives an age of 35.3±0.8 Ma (Table 3, Figures 11k and 11l). Biotites from sample V37 (sole of the SaPa thrust, Figures 5 and 9) give an inverse isochron age of 33.3±0.7 Ma (Table 3 and Figures 11m and 11n).

5.3.2.3. FSP granite: Sample V40 was collected near the NW margin of the FSP granite (Figure 5). The K-feldspar yields a relatively flat age spectrum slowly rising from 27 to 33 Ma (Figure 11o). The first 4% of ^{39}Ar release corresponds to a small plateau at 27.6±2 Ma (LT1) and is followed by a rough plateau at ≈28Ma (LT2). The final plateau (HT) is at 33.1±0.3 Ma. From inverse isochron calculations, neither

LT1 nor HT seem to be affected by excess argon (Table 3). An activation energy of 41.22 kcal/mol for argon diffusion can be calculated from the first six points of the Arrhenius diagram. However, it is impossible to model the data by assuming that the sample is composed of discrete diffusion domains sharing this activation energy. The first six steps correspond to <1% of the total ^{39}Ar release and to abnormally high K/Ca ratios. This suggests that the gas released during these steps is probably not characteristic of the bulk sample and may represent clay alteration. The following five isothermal stages (steps 7, 9, 11, 13, and 15) yield higher activation energy of 48.5 kcal/mol for argon diffusion, closer to the average determined by *Lovera et al.* [1997]. A relatively good fit to the data can be calculated assuming eight diffusion domains sharing this activation energy (Figure 11p). In that case, the first six steps are not fitted by the model. Assuming this activation
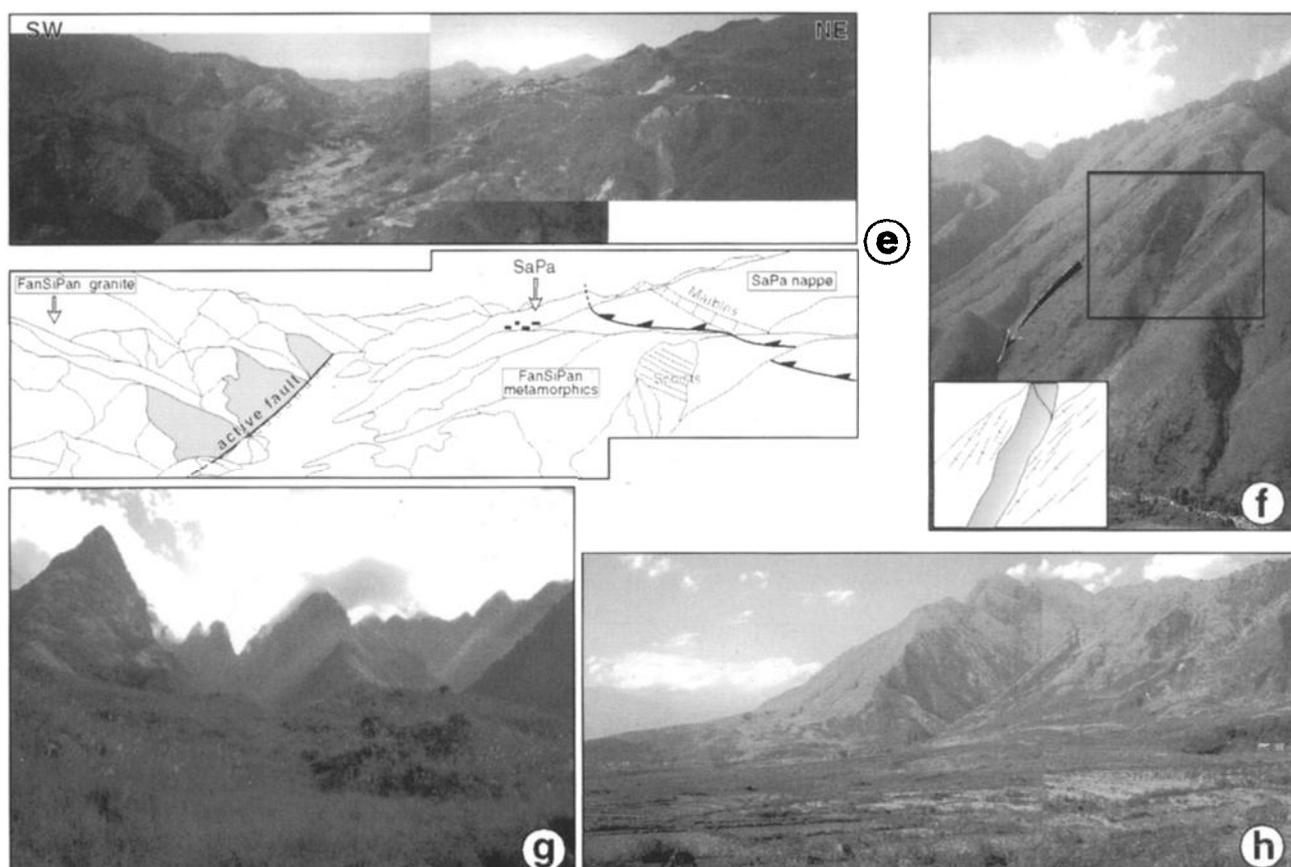
Figure 10. (continued)

energy and domain distribution, a cooling history that fits the age spectrum can be calculated: rapid cooling (≈150°C/Myr) until 33.5 Ma, then slow cooling until 28.5 Ma, at which time rapid cooling (190°C/Myr) resumes from ≈305°C. Note that the initial small plateau at 27.6 Ma (LT1) is not fit by this model.

5.3.2.4. TuLé hypovolcanics: V170 sampled the Tulé intrusive complex, ≈2 km away from the FSP granite (Figure 5), and yielded unzoned and undeformed K-feldspar. These K-feldspars give a highly variable age spectrum. The only indications that can be retrieved from this spectrum are the youngest and oldest ages (26 Ma and 96 Ma respectively) observed in the middle part of the spectrum, which is a priori less affected by argon contamination than initial and final steps. Such ages suggest a Cretaceous minimum age for the Tulé intrusives and a last cooling event around ≈26 Ma.

5.4. Discussion, Interpretation of the Cooling History and Deformation of the FSP Range

5.4.1. Cooling history of the FSP Range. From the above geochronological data we propose a complex cooling history for the FSP range (Figures 11d, 11q, 11r and 11s). None of these data give evidence for any thermotectonic episode older than 100 Ma. They are compatible with a Middle Cretaceous or older initial emplacement of some of the plutonic rocks of the FSP range: the Posen batholith and the Tulé intrusive complex (≈90 Ma, HT of V33Kf, oldest age of V170Kf). This assertion only rests on two high-temperature K-feldspar ages and thus needs confirmation (e.g., U/Pb zircon ages).

A major cooling event affected the entire FSP range at ≈35 Ma. It is documented both in the BatXat section (HT of V103 Kf) (Figure 11d), and in the FSP granite (V40 Kf) (Figures 11q and 11r). In the SaPa nappe this event is only shown by the age of V35 phlogopite from the décollement level, which is slightly older than all the nearby biotites. This event most probably occurred a short time after, or during, the emplacement of at least a part of the FSP granite: Titanites from sample YS50 (taken few meters from sample V40) gave an U/Pb age of 35.2±0.4 Ma interpreted as the granite crystallization age [*Zhang and Schärer*, 1999]. Cooling seems to have slowed for several million years, as suggested by V103Kf and V40Kf cooling histories and by the relatively large biotite age span (32 to 35 Ma).

Rapid cooling resumed at ≈28 Ma in the FSP granite (V40 cooling history), ≈27 Ma in the Posen granite (LT2 of V33Kf), and ≈25 Ma in the BatXat section (V103 cooling history). These cooling ages increase from NE to SW along a section perpendicular to the ASRR and from NW to SE along strike. Although more data are necessary to confirm these trends, we note that they correspond to the across- and along-strike diachronisms documented farther north in the Ailao Shan [e.g., *Harrison et al.*, 1996]. The age spectrum of V33Kf from the PoSen granite suggests another, later cooling event at ≈22 Ma (Figure 11q).

5.4.2. Kinematics of the ASRR in the FSP Range. The BatXat section in the continuation of the ASRR (section A, Figure 4) shows clear evidence of left-lateral deformation. A significant fraction of this deformation took place at ≈300°C (Table 2) and thus, according to the cooling

Table 2. Fansipan Range Petrography[a]

Site	Sample	Rock Type	Mineralogy	Deformation
			BatXat (Section A)	
Site A2	V103[b] Figures 5 and 6	orthogneiss	porphyroclasts: quartz, K-feldspar[b], epidote foliation: ribbons of recrystallized quartz (<0.25 mm), white micas, green biotite[b]	recrystallized quartz ribbons
Site A3	V105 Figure 6	orthogneiss	porphyroclasts: stretched epidotes (zoïsite + monoclinic) foliation: quartz ribbons, braun biotite, and green biotite boudins gaps: chlorite	sinistral C shear planes epidotes elongated and stretched in lineation direction
	V107 Figure 6	quartz mylonite	porphyroclasts: epidote, titanite foliation: quartz (<0.25 mm), braun biotite	recrystallized quartz ribbons
	V108 Figure 6	orthogneiss	porphyroclasts: K-feldspar, epidote, titanite foliation: ribbons of recrystalized quartz (<0.25 mm), white micas, green biotite boudins gaps: chlorite, calcite, quartz	sinistral C' shear planes titanite elongated and stretched in lineation direction
Site A6	V109 Figure 6	orthogneiss	porphyroclasts: epidote, titanite, green hornblende, K-feldspar foliation: quartz (<0.25 mm), braun biotite	sinistral C planes and conjugate dextral C planes
	V110 Figure 6	quartz rich ultramylonite	porphyroclasts: epidote, plagioclase foliation: quartz (<0.25 mm), braun biotite	recrystallized quartz ribbons
Site A7	V111 Figure 6	quartz ribbon	foliation: quartz (<0.05 mm)	recrystallized quartz ribbons
	V112 Figure 6	mylonite	porphyroclasts: epidote, titanite (≤0.25 mm) foliation: biotite	recrystallized quartz ribbons
Site A8	V113 Figure 6	mylonitic orthogneiss	porphyroclasts: K-feldspar, plagioclase, quartz, titanite foliation: quartz, white mica, braun biotite	sinistral C planes
			LaoCay-SaPa (section B)	
site B1	V27	orthogneiss	porphyroclasts: K-feldspar, plagioclase, quartz foliation: green biotite	dextral/normal shear planes see Figure 10a
site B3	V33[b]	orthogneiss	porphyroclasts: plagioclase foliation: green biotite[b], and small Q, plagioclase, and K-feldspar[b] tension gashes: calcite	penetrative left-lateral deformation see Figure 10d
site B4	V100[b]	orthogneiss	porphyroclasts: plagioclase foliation: biotite[b], and small Q, plagioclase and K-feldspar	penetrative deformation see Figure 10c
			SaPa Thrust	
	V35[b] Figures 5 and 9	marble	calcite foliation: phlogopite[b], plagioclase, chlorite? and amphibole?	some levels strongly foliated and lineated
	V37[b] Figures 5 and 9	amphibolite	green hornblende, biotite[b], quartz	foliation
			FanSiPan Granite	
	V40[b] Figure 5	fine-grained granite	plagioclase, K-feldspar[b], quartz	slight preferred orientation
	V97[b] Figure 5	leucocratic dike	plagioclase, K-feldspar, quartz, green hornblende, titanite	slight foliation
			Tulé Hypovolcanics	
	V170[b] Figure 5	rhyolite	xenocrysts: feldspar[b] and quartz	no deformation

[a]Sites and samples located on Figures 5, 6, and 9.
[b]The $^{39}Ar/^{40}Ar$ samples, see Figure 11.

history constrained by $^{40}Ar/^{39}Ar$ thermochronology, between 35 and 25 Ma (Figure 11d). Such an age range is in agreement with previous ages determined for left-lateral deformation along the ASRR [e.g., *Schärer et al.,* 1990, 1994; *Leloup et al.,* 1995; *Harrison et al.,* 1996]. The deformation along the BatXat section is thus clearly due to Oligo-Miocene left-lateral motion between Indochina and south China. This left-lateral deformation is more complicated toward the SE, where the

shear zone has been dissected by later faults (Figure 5). In the Posen granite, NW-SE left-lateral shear indicators exist but appear less intense. V33 biotite age (34.2±.7 Ma, Table 3, Figures 11g and 11h) corresponding to the conditions of left-lateral deformation (≤ 300°C, Table 2), indicates that such deformation probably took place around 34 Ma and later. This is again compatible with the ASRR timing. Emplacement of the SaPa nappe took place during and prior to the crystallization

Table 3. Fansipan range $^{40}Ar/^{39}Ar$ results

Section/Site	Sample					Plateau Age		Inverse Isochron Age				Reference
	Number	Location	Mineral	Size, μm	Lab[a]	Age,[b] Ma	Steps	Age, Ma	$^{40}Ar/^{36}Ar_i$	MSWD[d]	Steps	
Bat Xat section (section A)	V103	22°32'56"N 103°47'20"E	biotite		UCLA	28.1±0.1[c]	mean of 3 laser total fusions					Harrison et al. [1996]
		Figures 5 and 6	Kf		UCLA	LT: 25.1±0.1[c]	5 steps/42 (10-14) 20% of gas	25.1±0.3	303±45	87	39% of gas 10 steps/42 (8-17)	Harrison et al. [1996] and this study
						HT: 34.6±0.3[c]	4 steps/42 (27-30) 16% of gas	34.1±0.4	307±1	6.9	24% of gas 10 steps/42 (27-36)	
LaoCay-SaPa section (section B)	V33	22°21'53""N 103°56'33"E	biotite MgFe=0.99	125-250	UBP	34±0.8	6 steps/11 82% of gas	34.2±0.7[c]	277±3	1.8	9 steps/11 -(1,11)	this study
Posen granite		Figures 5 and 9	Kf	125-250	UBP	LT1: 22±0.4[c]	steps 6, 8 and 10 5% of gas	22.5±0.5	286 ± 68	0.003	steps 6, 8 and 10 5% of gas	this study
						LT2: 26.7± 0.5	steps 12 - 14 9.4% of gas	25.6±0.6[c]	397± 64	0.004	steps 11-14 13%of gas	
						HT: 88.6±1.7[c]	steps 31 to 33 19% of gas	88.5±6.6	299±83	4.1	steps 31 to 33 19% of gas	
	V100	22°17'35"N 103°55'07"E Figures 5 and 9	biotite MgFe=0.86	250-400	UBP	31.4± 0.6	7 steps/13 86.4 % of gas	32.4±0 7[c]	256±4	21	9 steps/13 -(1,11,12,13)	this study
Sa Pa thrust	V35	22°20'18"N 103°51'15"E Figures 5 and 9	phlogopite MgFe=18.3	250-400	UBP	34.9±0.7	84.11% of gas 4 steps/8	35.3±0.8[c]	325±8.3	1.3	on all steps	this study
	V37	22°18'05"N 103°54'28"E Figure 5 & Figure 9	biotite MgFe=1.66	250-400	UBP	33.6±0.96	8 steps/ 13 96.33% of gas	33.3±0.7[c]	304±0.9	1.7	9 steps /13 -(1,11,12,13)	this study
FanSiPan granite	V40	22°21'43"N 103°45'40"E Figure 5	Kf	125-250	UBP	LT: 27.6±2[c]	9 steps/38 (3-11) 4% of gas	27.4±0.6	309±11	1.5	9 steps/38 (3-11) 4% of gas	this study
						HT: 33.1±0.3[c]	6 steps/38 (33-36) 29% of gas	33.5±0.7	300±12	5295	6 steps/38 (33-38) 30% of gas	
Tulé hypovolcanics	V170	22°02'07"N 104°00'19"E Figure 5	Kf	125-250	UBP	youngest age ≈26 Ma oldest age =96 Ma	no plateau age					this study

[a]UBP, Université Blaise Pascal, Clermont Ferrand. UCLA, University of California, Los Angeles.
[b]LT, low furnace temperature (400-700°C) age, LT1, lower furnace temperature (500-600°C) age, LT2, 650-700°C furnace temperature age, HT, high furnace temperatures (1000-1200°C) age.
[c]Preferred age.
[d]MSWD : mean square weighted deviation.
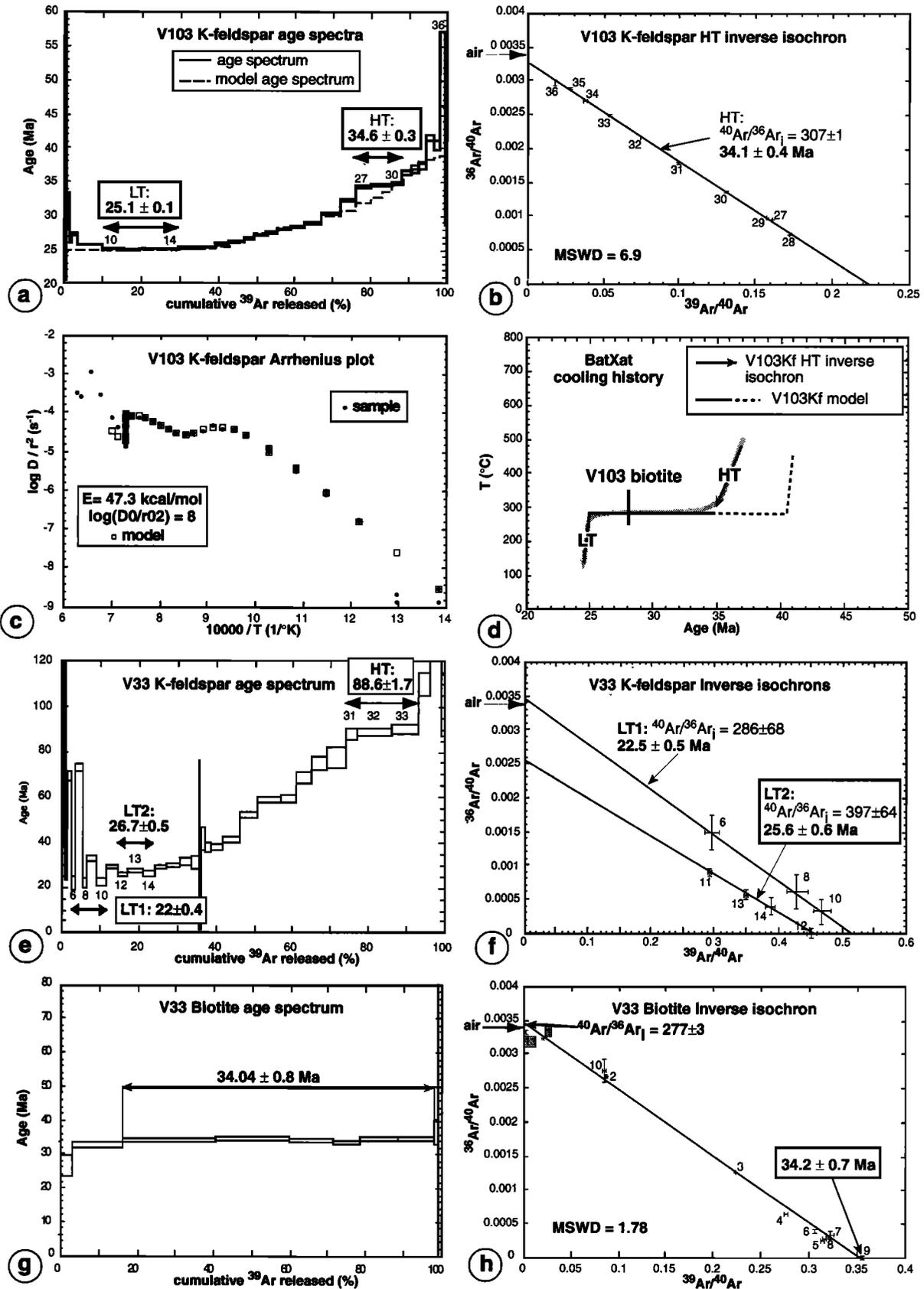
Figure 11. The ^{40}Ar/^{39}Ar data from the FanSiPan range. Results are summarized in Table 3 and samples located on Figures 5, 6, and 9a. (a, e, g, i, k, m, o) Conventional age spectra. In the case of K-feldspar, model age spectra are also shown. (b, f, h, j, l, n) Inverse isochrons. Each step is plotted with the corresponding error bars and step number, the drawn regression line corresponds to the age and ^{40}Ar/^{36}Ar$_i$ calculated. Step numbers in grayed boxes were not used for calculations. (c, p) K-feldspar Arrhenius plots showing both experimental and model data (see text for details). (d, q, r) Cooling histories deduced from geochronological results (see text). Large shaded lines represent preferred T-t histories. U/Pb age of YS50 titanites is from *Zhang and Schärer* [1999]. (s) Synthesis of the FanSiPan range cooling history.

Figure 11. (Continued)

SaPa nappe and PoSen granite cooling history

?

V35 phlogopite

V33
Kf-LT2

V33, V37, V100
biotite

V33
Kf-LT1

(q)

FanSiPan granite cooling history

YS50 titanites

V40 Kf
model

LT2

LT1   V40 Kf

(r)

FanSiPan range cooling history

FanSiPan,
Sapa and Posen

BatXat

?

?

?

zipper
SaPa

FanSiPan
granite

zipper
BatXat

PoSen
granite

(s)
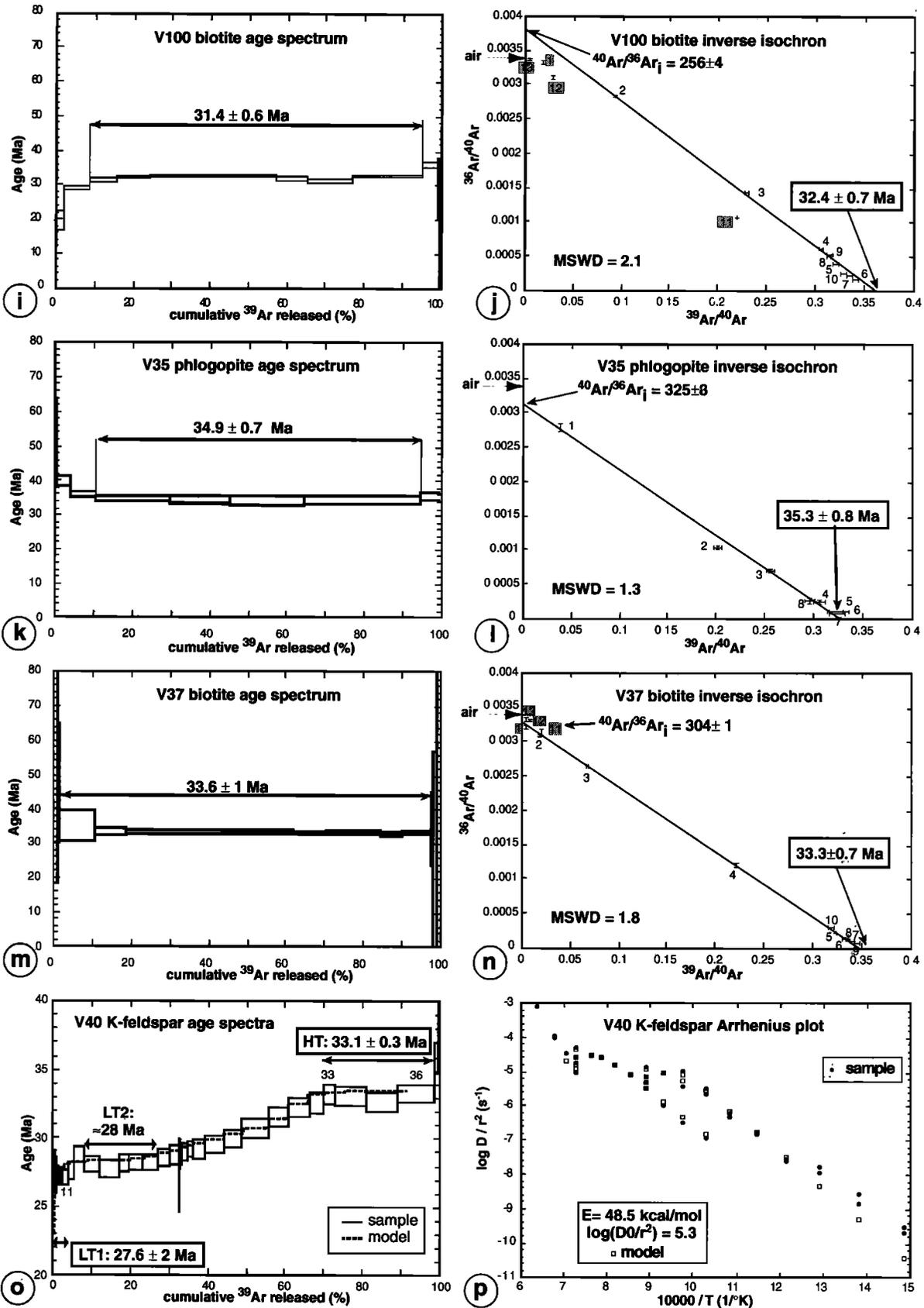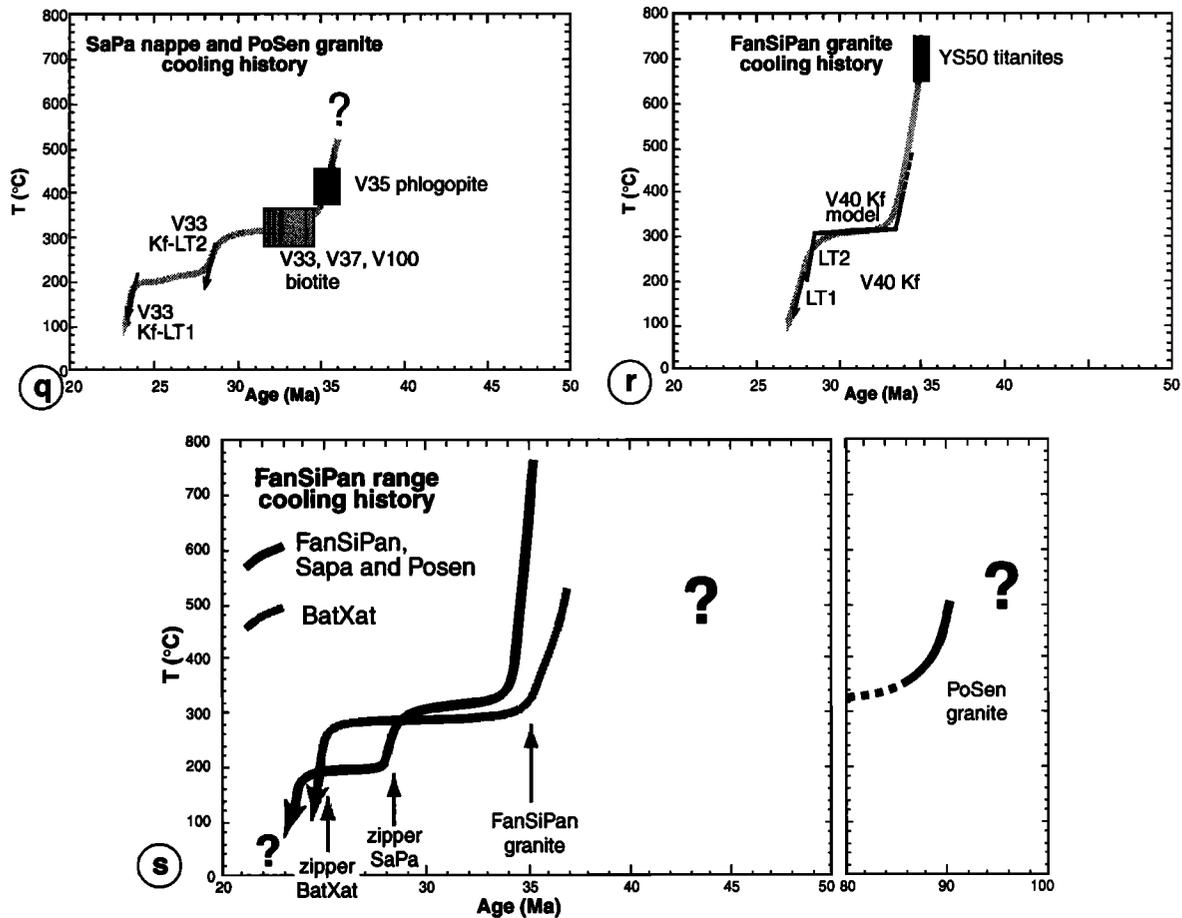
Figure 11. (Continued)

of V35 phlogopites dated at 35.3±0.8 Ma. We interpret the ≈35Ma event as the contemporaneous cooling of the FSP granite and thrusting of the SaPa nappe in a left-lateral strike-slip environment.

Tertiary deformation related to the ASRR within the Tulé intrusive rocks is not documented. These rocks experienced their last cooling below 300°C at ≈26 Ma, the time at which the nearest rocks of the ASRR (V33) were rapidly cooling. Metamorphic units and granites crop out NE of the Tulé intrusive rocks (Figure 4). These units do not seem to have been affected by left-lateral shear parallel to the ASSR and yield Early Proterozoic K/Ar ages on amphiboles (≈1700 and ≈2000 Ma [*Nam*, 1998a]). Such old rocks probably correspond to large-scale "boudins" separated by brittle left-lateral faults (Figure 4). The trace of the main ASRR thus becomes obscure south of LaoCai on the SW bank of the Red River. On the NE bank of the river the DayNuiConVoi is a range of high-grade rocks mapped as Proterozoic [*GGDDR Vietnam*, 1973; *GDMGSR Vietnam*, 1988]. This range has been interpreted as the main trace of ASRR in Vietnam [*Leloup et al.*, 1995].

6. The DayNuiConVoi (DNCV) Range

The DayNuiConVoi (DNCV) range extends for ≈270 km, from south of PingBian (China) to VietTri (Vietnam) where it disappears below the Quaternary Hanoi basin (Figure 4). Rocks similar to those of the DNCV crop out ≈100 km farther south, north of the city of NinhBinh, surrounded by Quaternary deltaic deposits (site G, Figure 4).

6.1. Structure

6.1.1. Structure of the DNCV metamorphic belt. The DNCV is bounded by active right-lateral strike-slip faults: the SongChay fault zone to the NE and the Red River fault zone to the SW (Figures 5 and 12), [*Replumaz et al.*, 2000]. Recent activity on these faults is attested to by the sharpness of their morphology and by river offsets. High-relief and triangular facets suggest that the Red River fault system also has a normal component of movement that has denuded the DNCV range. Triangulation and GPS measurements conducted 11 years apart (1983 and 1994, respectively) are compatible with a present-day right-lateral strike-slip rate of 1-5 mm/yr on the Red River fault near YenBai [*Duong and Feigl*, 1998].

Owing to dense vegetation and intense weathering (near YenBai, the lateritic layer can reach 30 m in thickness), fresh exposures of metamorphic rocks are scarce. We studied the DNCV rocks along four sections across the range and in six other localities (Figures 4, 5 and 12). Most rocks are mylonitic micaschists and gneisses, migmatitic in places, that exhibit well-defined foliation and stretching lineation. Foliation strike is relatively constant: NW-SE with local variations that are discussed below (Figures 5, 12 and 13). They constantly dip to the NE along the NE flank of the range and to the SW along its SW flank (Figure 14). Dips in the core of the range are more variable: steep along sections B and D and shallower along section E (Figures 9 and 14). The DNCV thus presents the structure of a metamorphic dome, very similar to
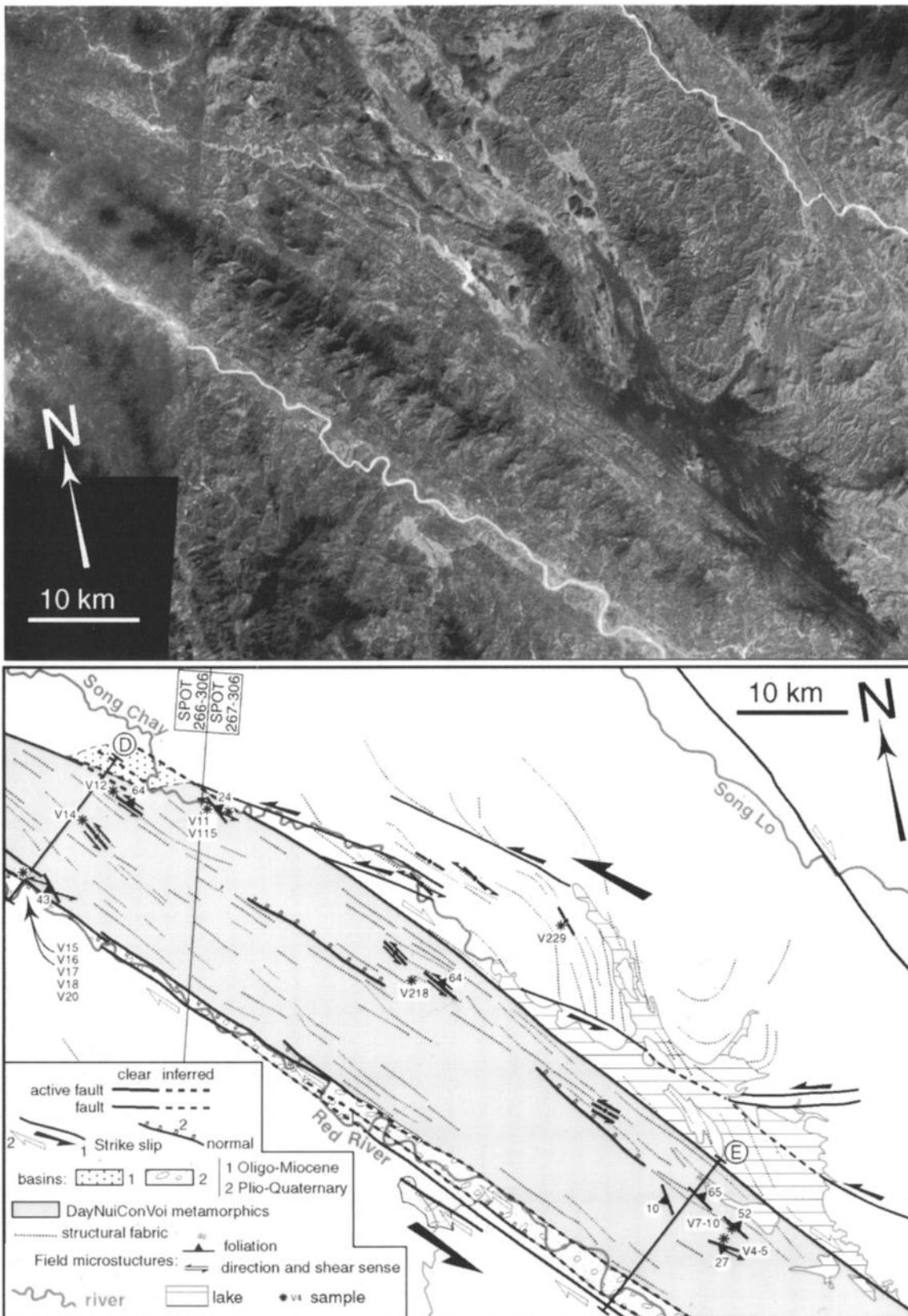
Figure 12. Satellite image and structural map of central DayNuiConVoi range. (a) Mosaic of part of 266-306 and 267-306 SPOT images. See location on Figure 4. (b) Corresponding structural map drawn from interpretation of satellite images and field observations. Samples discussed in text are located as well as sections D and E (Figure 14).
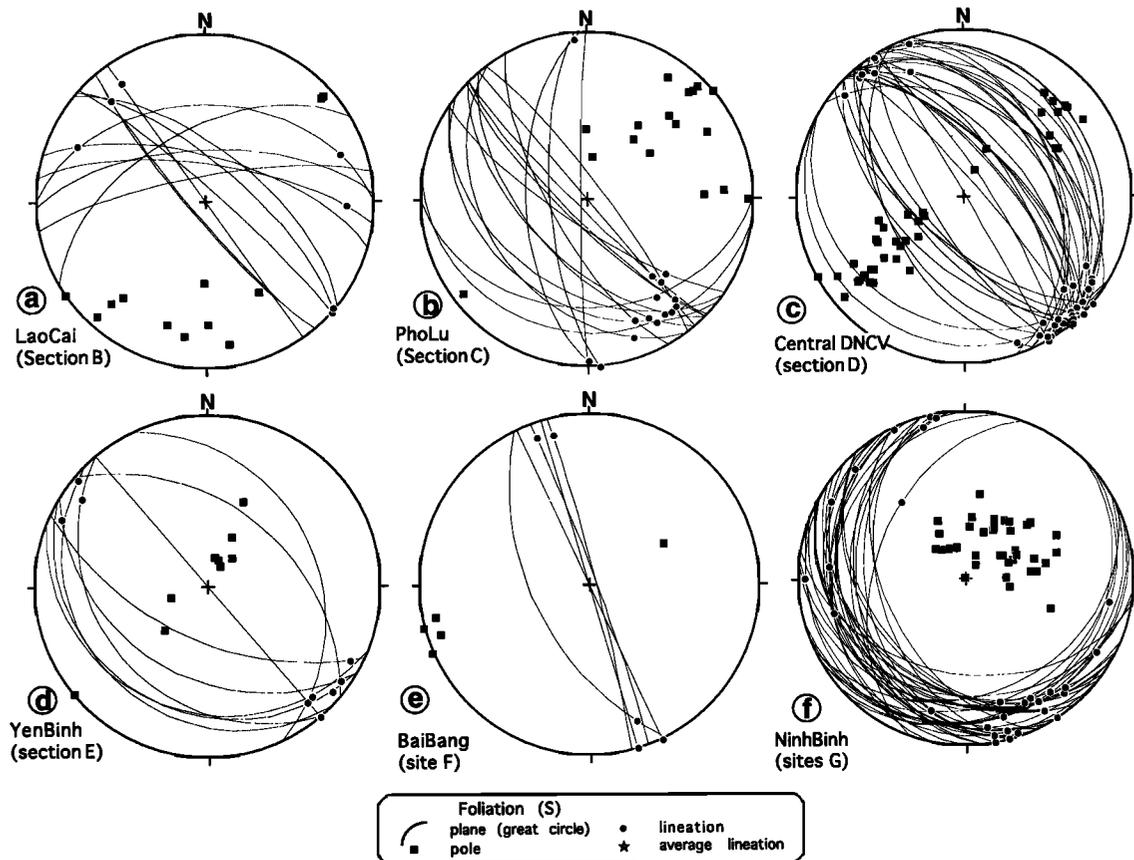
Figure 13. Structural data from DayNuiConVoi range (Schmidt diagram lower hemisphere). Sections and sites located on Figure 4. (a) LaoCai section (NE part of section B), 12 foliations and 8 lineations. (b) PhoLu section (section C), 18 foliations and 16 lineations. (c) Baoyen area (central DNCV) and section (section D), 38 foliations and 35 lineations (see Figures 12 and 14a). (d) Yen Bai-YenBinh-Tan Huong section (section E), 9 foliations and 9 lineations (see Figures 12 and 14b). (e) Baibang outcrop (site F), 5 foliations and 5 lineations. (f) NinhBinh area (site G), 12 foliations and 8 lineations.

the DianCang Shan 600 km farther NW along strike [*Leloup et al.*, 1993]. South of YenBai, structural observations and sampling are difficult due to poor quality outcrops. A quarry in BaiBang city exhibits migmatitic gneisses with a steep NW-SE foliation (site F, Figures 4 and 13e). In this area, foliation geometry is similar to that seen along section E.

Most rocks of the DNCV exhibit a clear mineral and stretching lineation which generally plunges gently towards the SE (Figure 13). In some areas (e.g., section E, Figure 14) the foliation is affected by metric folds with axes parallel to the lineation. Locally, sheath folds elongated parallel to the lineation are found. These observations strongly suggest, as in the Ailao Shan-FSP belt, an intense deformation with a finite stretching parallel to the belt.

In the field and thin section, many shear criteria (C and C'/S structures, rolling structures, asymmetric boudinage) are found in sections perpendicular to the foliation and parallel to the lineation (Figures 15c, 15f and 16). Where the foliation is steep, these criteria indicate a left-lateral sense of shear. Where foliation dip gently toward the SW (on the SW flank of the structure) shear criteria indicate a top to the SE sense of shear. Where dips are toward the NE (on the NE flank of the structure), shear senses are top to the NW. All the shear

criteria are thus compatible with an overall left-lateral sense of shear along a NW-SE direction.

The DNCV shares many structural features with the other metamorphic ranges of the ASRR [e.g., *Leloup et al.*, 1995]. The geometry of the stretching lineation is quite constant, always nearly horizontal and parallel to the trend of the belt, whereas the foliation is often steep and parallel to the trend of the belt. There are departure from this ideal case of strike-slip shear, however. Gentle dips are common and can even dominate, as along section E, and foliation and lineation strikes are less constant than farther north along the ASRR. Foliation strikes depend on the shear deformation intensity. Where deformation is less intense, foliation trends more northerly, defining large-scale foliation boudins or fish whose asymmetry attests for shear sense (Figures 5 and 12). This is especially true around boudins of marble, amphibolite, microgranite, and ultramafic rocks that can reach widths of several hundreds of meters. Large-scale C' shear planes are common along the ASRR [e.g., *Leloup et al.*, 1995]. They make an angle of 10°-30° with the mylonitic/shearing direction. In the case of the DNCV, foliation trends more westerly at the proximity and within these large C' shear planes. This is the case in the northern part of LaoCay section (section B, Figures 5 and
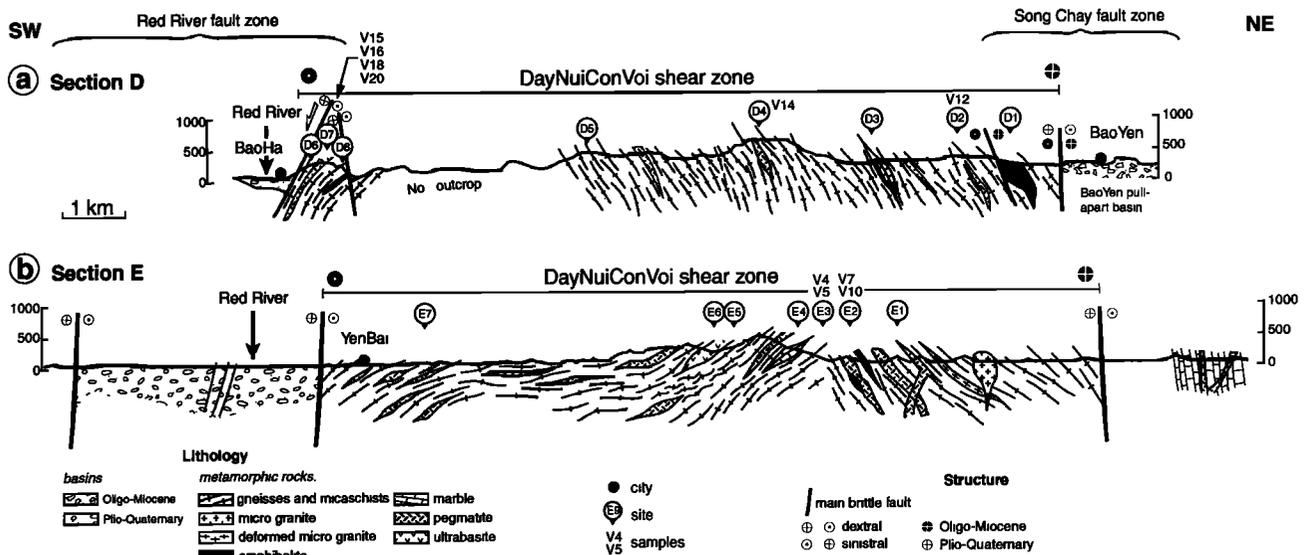
Figure 14. Cross sections of DayNuiConVoi metamorphic range. Sections are located on Figure 12. (a) BaoYen-BaoHa section (section D, Figures 13c, 15a-d and 16. (b) YenBai-YenBinh-TanHuong section (section E, Figure 13d).

13a). The flatness of the foliation can be interpreted in several ways. It could result from a larger componant of vertical flattening, thus suggesting that the ASRR was more and more transtensive toward the SE. Given the ubiquity of large-scale boudins, another possibility is that some of the metamorphic rocks of the DNCV could have acquired a flat foliation prior to being strongly reworked within the ASRR. These two possibilities are not mutually exclusive, but the poor outcrop conditions preclude deciphering the extent of each process.

Small-scale brittle normal faults cut across the ductile structures. Some of these faults trend NW-SE, parallel to the two main faults bounding the DNCV range, and they most probably result from the current deformation episode. Others trend NE-SW, perpendicular to the stretching lineation. Horizontal stretching resulting from these late faults is thus nearly parallel to the ductile lineation.

6.1.2. Structure along the northern flank of the DNCV metamorphic belt.
Low-grade schists and marbles crop out north of the DNCV. The schistosities in these rocks strike from N-S to NW-SE with variable dips. Such structure is comparable with that observed within the DNCV: Where the deformation is mild, the schistosity trends N-S, corresponding to an approximately E-W compression; where deformation is more intense, schistosity trends NW-SE, and WNW-SSE trending left-lateral shear planes are observed. At the large scale, left-lateral faults bounding sigmoidal boudins of metamorphic rocks are detected on SPOT images (Figure 12). We interpret these structures as resulting from the same NW-SE left-lateral shear that affects the metamorphic rocks of the DNCV. The main difference is that angles between S and C directions are larger, suggesting that deformation is milder. A further complication is that the shear planes commonly exhibit gentle dips toward the NE with horizontal lineations. In such cases, shear criteria indicate top to NW.

Near BaoYen, the northern edge of the metamorphic rocks jumps south (Figure 12) and a large amount of conglomeratic sedimentary rocks is found. These sediments are mapped as Miocene and Oligocene (Figure 12) [GGDDR Vietnam, 1973]

and are locally vertical and parallel to the DNCV. They were thus possibly deposited in a pull-apart along a left-lateral precursor to the SongChay fault.

6.1.3. Metamorphic rocks east of NinhBinh.
South of VietTri, the DNCV metamorphic rocks disappear below the Quaternary but probably extend toward Hanoi and the South China Sea margin. High-grade mylonitic rocks containing large pegmatitic pods, very similar to those of the DNCV, crop out at 35 km from the sea shore, east of the city of NinhBinh (site G; Figure 4).

The outcrops consist of small hills emerging from the Red River delta plain. Most of these hills are aligned approximately N-S. Foliation is nearly flat, dipping gently toward the west or south (Figure 13f). In some places, the stretching lineation is very clear (Figure 15e) and trends from N-S to NW-SE (Figure 13f). It is possible to follow the same lineation swinging from NW-SE to N-S, resulting from wrapping around large boudins. In few places, approximately E-W lineations are observed. Such lineations may have formed during a previous high-temperature event and have been preserved within boudins. On NW-SE to N-S vertical sections, large (several centimeters) feldspar rolling structures and σ-type asymmetric tails on smaller porphyroclasts indicate top-to-the-north shear sense (Figure 15f). The high grade metamorphic banding is commonly affected by small C' normal shear planes that generally dip gently to the north, also suggesting an overall top-to-north shear sense (Figure 15f). However, the presence of opposite shear sense indicators suggests a large component of vertical flattening during the high-temperature deformation.

As in the DNCV, the high-grade metamorphic rocks are affected by two generations of normal faults. The first generation consists of approximately E-W trending and north steeply dipping faults. These faults are nearly parallel to the above mentioned C' shear planes and could have been formed during the same tectonic event. The second generation trends N170°E, compatible with the present stress regime. A large fault of this direction may be responsible for the emergence of
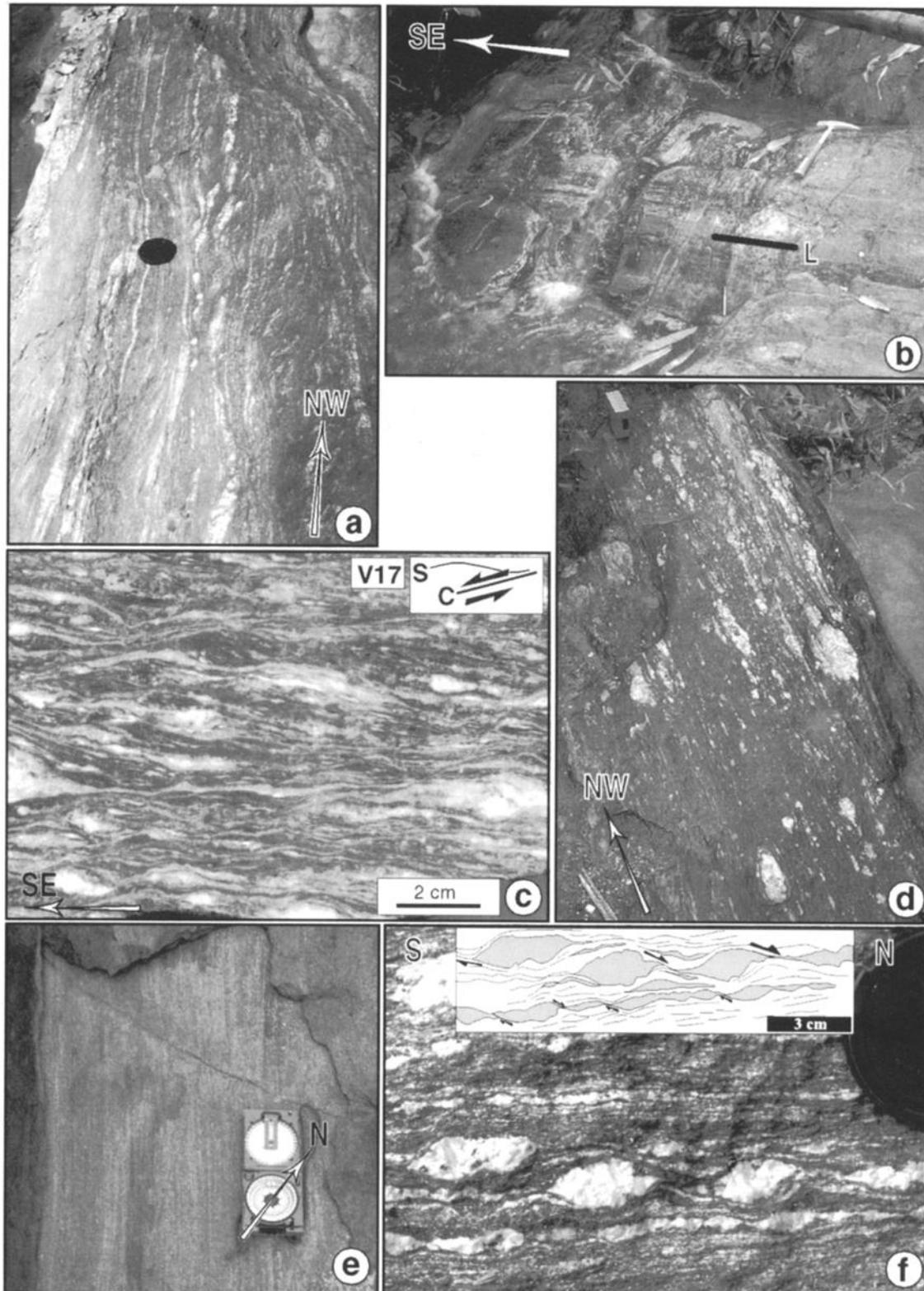
Figure 15. Structural field observations in DayNuiConVoi range. Sites located on Figures 4, 12 and 14a. (a) Banded steep mylonites at site D6, foliation strikes N140° (view from above, lens cap gives scale). (b) Steep foliation (N147°,78°NE) and subhorizontal stretching lineation (pitch 18°S) at site D5. (c) Polished slab of sample V17 (site D7) showing left-lateral C/S structures (view from above). (d) High-temperature foliation (site D5) typical of DayNuiConVoi range striking N150° (view from above). (e) Flat foliation and N165° trending stretching lineation at site G (compass gives scale). (f) Shear criteria indicating top to the north shear at site G.
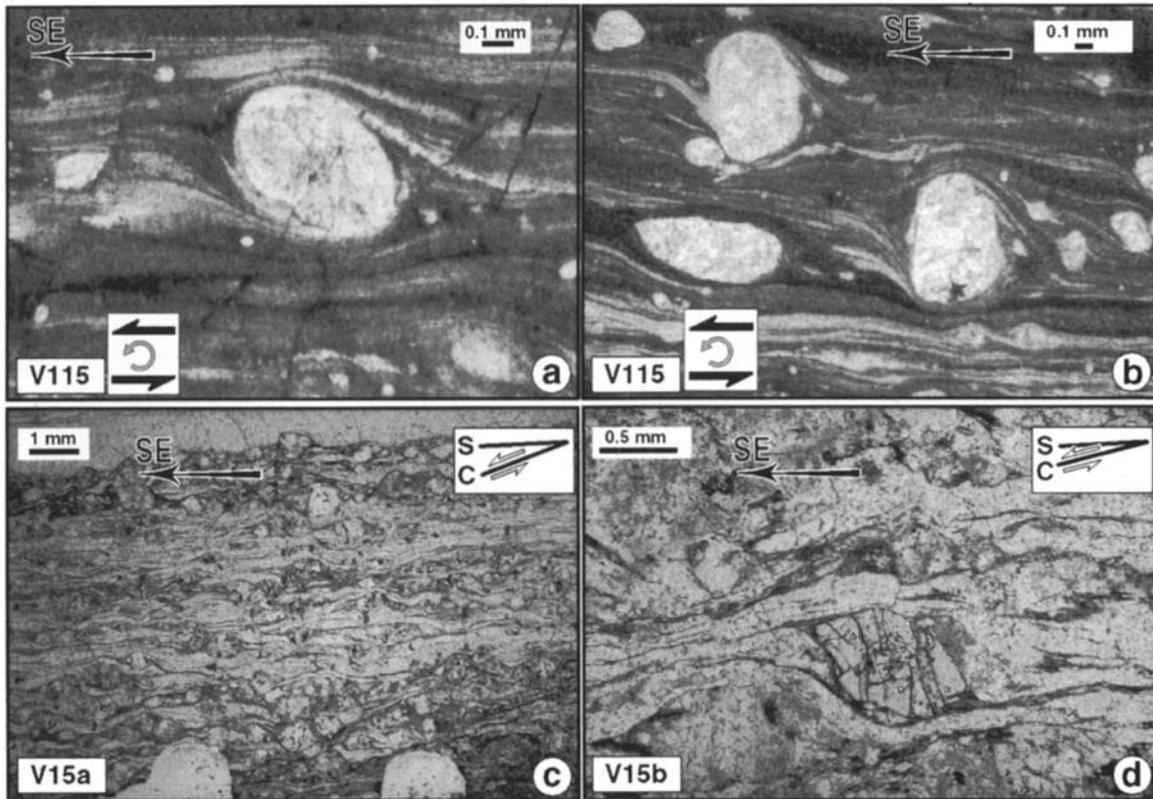
Figure 16. Shear criteria in polished thin sections from DayNuiConVoi range. (a, b) Rolling structures from sample V115 (Figure 12). Section perpendicular to foliation (N147°,25°E) and parallel to stretching lineation (azimuth N127°), view from above. (c, d) Left-lateral C/S structures from sample V15 (site D6, Figures 12 and 14a). Section perpendicular to foliation (N135°,47°S) and parallel to stretching lineation (pitch 0°, view from above).

the metamorphic hills. Movement on these late normal faults may have been responsible for tilting the foliation whose precise initial geometry is difficult to assess but was probably nearly flat.

6.2. P-T Conditions of Deformation in the DNCV Range

6.2.1. Petrography. Most rocks of the DNCV range are garnet-sillimanite gneiss and micaschists which probably are metamorphosed pelitic rocks. These micaschists contain various amounts of leucosomes and leucocratic dikes. The quartzofeldspatic leucosomes define a small-scale banding concordant with the foliation (Figures 15a, 15d and 15f). Some of the dikes were clearly affected by the left-lateral deformation, whereas others were not. Such relationships suggest that both the leucosomes and the dikes result from partial melting during left-lateral deformation, as in the other ranges of the ASRR. The amount of melts progressively increases along strike from the NW to the SE. Some leucocratic layers contain large corundums crystals (e.g., V218, Table 4). Rubies, which can be of good quality and as large as 1.7 kg, are found within the DNCV micaschists. Leucocratic dikes are also found outside of the DNCV range in the LucYen area, where they intrude large marble boudins (Figure 14b). There, at the proximity of the dikes, a corundum (ruby) + phlogopite + graphite + spinel paragenesis developed within the marbles. Small undeformed microgranites are locally found within the shear zone. Outcrop

conditions are so poor that we could not determine if these microgranites correspond to large boudins or if they crosscut the micaschists (Figure 14b).

Marble and amphibolite are locally interlayered within the garnet micaschists (Figure 14). Such layers vary in size from few to several meters across strike and from several meters to hundreds of meters along strike. These layers represent boudins of rocks with initially different compositions (mudstone for marbles and probably volcanic rocks for amphibolites) which were sheared and metamorphosed together with the surrounding schists. Some large serpentinite bodies also crop out within the micaschist. It is not clear if these bodies resulted from the alteration of metamorphosed mafic or ultramafic rocks.

6.2.2. Parageneses and deformation within the micaschists. The DNCV micaschists contain biotite + garnet ± sillimanite + quartz + plagioclase + K-feldspar ± cordierite ± zircon ± white micas ± chlorite (Table 4). The foliation is mostly defined by the biotites and by recrystallized quartz ribbons. Sillimanite crystals are aligned in the stretching lineation direction. Garnets occur as large porphyroclasts, sometimes euhedral, but often exhibiting a long axis parallel to the stretching lineation (Table 4; Plate 1a-d). Pressure shadow crystallizations of biotite, chlorite and white micas develop in the direction of this long axis. In many cases, these pressure shadows are asymmetric, testifying to noncoaxial shear during their growth (Plate 1b). The garnets contain quartz + biotite ± plagioclase ± sillimanite ± zircon ±

Table 4. DayNuiConVoi Range Petrography[a]

Site	Sample	Rock Type	Mineralogy	Deformation
			Section D	
BaoYen 1	V11 Figure 12	orthogneiss	porphyroclasts: K-feldspar, few garnet (elongated), zircon foliation: recrystallized quartz and small biotites	cataclastic deformation some left-lateral shear criteria
BaoYen 2	V115 Figure 12	mylonitic paragneiss	porphyroclasts: K-feldspar, zircon foliation: very finely recrystallized quartz ribbons, and biotites	left-lateral rolling structures on K-feldspars, and C planes (see Figures 16a and 16b)
site D2	V12[b,c] Figures 12 and 14	mylonitic garnet micaschist	porphyroclasts: garnet (mostly rounded but some very elongated) containing zircon and biotite inclusions, K-feldspar[b] with biotite inclusions, quartz, and plagioclase foliation: quartz ribbons, biotite[b], sillimanite, zircon tails: biotite	sinistral C planes, and few conjugate dextral C planes
site D4	V14 Figures 12 and 14	leucocratic garnet micaschist	porphyroclasts: garnet (mostly rounded but some broken and recrystallized) containing quartz, and biotite inclusions, few K-feldspar, and plagioclase foliation: short quartz ribbons, biotite, sillimanite tails: biotite, and K-feldspar	asymmetric tails on garnets indicating left-lateral shear
site D6	V15 Figures 12 and 14	mylonitic paragneiss	porphyroclasts: K-feldspar, and small garnets containing, quartz, and biotite inclusions foliation: quartz ribbons, biotite tails: biotite	numerous left-lateral shear planes (see Figures 16c and 16d)
	V16 Figures 12 and 14	mylonitic orthogneiss	porphyroclasts: K-feldspar, and few garnets foliation: recrystallized quartz ribbons, chloritised biotite, few white micas tails: K-feldspar, and chlorite	left-lateral C' shear planes
site D7	V18[b] Figures 12 and 14	fine-grained orthogneiss	porphyroclasts: K-feldspar and small garnets (some very elongated) containing quartz, and biotite inclusions foliation: recrystallized quartz ribbons, biotite[b] tails: K-feldspar, and biotite	left-lateral C shear planes
	V20[b] Figures 12 and 14	amphibolite	foliation: green hornblende, biotite[b], plagioclase, quartz	
			Zone and Section E	
site E8	V218 Figure 12	leucocratic layer	porphyroclasts: corundum foliation: biotite, sillimanite, plagioclase, K-feldspar, zircon tails: titanomagnetite, sillimanite, garnet, biotite	long tails on corundum porphyroclasts
site E3	V4[b,c] Figures 12 and 14	mylonitic garnet micaschist with leucocratic veins	porphyroclasts: garnet containing, quartz, and biotite inclusions, K-feldspar[b], plagioclase, quartz, zircon, apatite foliation: quartz ribbons, biotite[b], sillimanite, zircon, rutile tails: biotite, quartz, sillimanite	top to the north (sinistral) shear planes crosscutting garnet outlined by sillimanites (see Plate 1b) asymmetric pressure shadow tails stretched sillimanites
	V5 Figures 12 and 14	mylonitic garnet micaschist	porphyroclasts: large elongated garnets with circular cores containing quartz, sillimanite,zircon, and biotite inclusions, zircon foliation: quartz ribbons, biotite, sillimanite tails: biotite, sillimanite, quartz	some very elongated garnets, others clearly broken few left-lateral asymmetric tails and C planes (see Plate 1c)
site E2	V7 Figures 12 and 14	biotite-rich garnet micaschist	porphyroclasts: garnets with quartz, and biotite inclusions, K-feldspar with biotite inclusions, plagioclase, zircon foliation: quartz ribbons, biotite tails: biotite, quartz	numerous left-lateral C planes
	V10 Figures 12 and 14	mylonitic garnet micaschist	porphyroclasts: small garnets, and large K-feldspar containing biotite inclusions foliation: quartz ribbons, biotite, sillimanite tails: biotite	very elongated garnets
Site F (Viet Tri)	V1[b,c] Figure 4	mylonitic garnet micaschist	porphyroclasts: garnet containing sillimanite, quartz, and biotite inclusions, K-feldspar[b], plagioclase, quartz, cordierite foliation: quartz ribbons, biotite, sillimanite tails: biotite[b], chlorite, white mica	elongated garnets (see Plate 1a) broken piece of garnets floating in foliation stretched sillimanites
			Luc Yen	
	V161[b]	marble	calcite, ruby, phlogopite[b], graphite	
	V229	marble	calcite, ruby, phlogopite, graphite, sphene, rutile	

Table 4. (continued)

Site	Sample	Rock Type	Mineralogy	Deformation
			Ninh Binh	
site G1	V132[c] Figure 4	mylonitic garnet micaschist	porphyroclasts: garnet containing, quartz, and biotite inclusions, K-feldspar, plagioclase, quartz foliation: quartz ribbons, biotite, sillimanite tails: biotite, chlorite, white mica	rounded and elongated garnets, shear planes and asymmetric tails on garnets
site G2	V126[b] Figure 4	mylonitic garnet micaschist	porphyroclasts: garnet containing sillimanite, quartz, and biotite inclusions, K-feldspar, plagioclase, quartz, cordierite foliation: quartz ribbons, biotite[b], sillimanite tails: biotite, chlorite, white mica	small rounded and broken garnets with tails
	V127[c] Figure 4	mylonitic garnet micaschist	porphyroclasts: garnet containing quartz, feldspar, and biotite inclusions, K-feldspar, plagioclase foliation: quartz ribbons, biotite, sillimanite tails: biotite	asymmetric tails on garnet indicating top to the North shear criteria

[a]Sites and samples located on Figures 4, 12 and 14.
[b]The $^{39}Ar/^{40}Ar$ samples, see Figure 18.
[c]P-T estimates, see Plate 1h and Tables 5, A1 and A2.

monazite inclusions (Table 4). Plagioclase and K-feldspar are found as small porphyroclasts within the foliation. In sample V1, cordierite porphyroblasts occur in the matrix at the periphery of garnets (Plate 1a). In some cases garnets are shattered in many small pieces indicating continued low grade deformation.

6.2.3. Thermobarometry of the high temperature paragenesis. Detailed microprobe analyses of selected sillimanite and garnet-bearing samples (V12 from section D, V4 from site E1, V1 from site F, V127 and V132 from site G2) show that all large garnets are zoned. Garnet rims have higher Fe and Mn and lower Mg contents than garnet cores (e.g., sample V1, Plate 1e, and sample V132, Plates 1d and 1f). In most cases, garnet Ca contents are nearly constant, below 6% grossular, but the largest garnets from sample V132 also show an inner core with up to 14% grossular (Plates 1d and 1f).

This chemical zoning may be interpreted as the result of progressive garnet growth under changing P-T conditions (cores) and late stage reequilibration (e.g., V1 rims). Within this continuous evolution we have distinguished four garnet phases (Plate 1g) that, together with the other minerals crystallizing at the same time, define four parageneses. The initial phase (garnet phase I or GPI), characterized by the higher Ca content, is only seen in the inner core of the largest garnets of sample V132 (Plate 1d and 1f), whereas the following phases are seen in all garnets (Table 5, and Plate 1g). For each garnet phase and each sample we calculated the corresponding pressure-temperature (P-T) estimates using classical thermobarometers based on gt-bt [*Hodges and Spear*, 1982] and/or the gt-sill-pl-bt-q [*Ganguly and Saxena*, 1984] equilibria (Table 5). For the garnet cores (GP I and II), garnet compositions were equilibrated with composition of inclusions. These inclusions have different compositions than the same minerals in the matrix or in the pressure shadows (e.g., plagioclase inclusions are more calcic and biotite inclusions have higher X_{Mg}). No chemical zoning of the garnet has been detected near the inclusions. We thus interpret the composition of the inclusions (and the P-T conditions that can be calculated from those) as inherited from

the time of their incorporation within the garnets. As the high calcic inner cores of garnets from V132 contain small plagioclase inclusions but no biotite, we could only use the gt-sill-pl-bt-q thermobarometer for GP I and the corresponding temperature and pressure are not tightly constrained (Tables 5, A1 and A2, and Plate 1h). The second phase (GP II) corresponds to V132 garnet outer core and garnets core of all other samples. These cores contain ≈70% almandine, 22% pyrope, 3% spessartite, and 5% grossular (Tables A1 and A2, and Plates 1e and 1f). This growth phase incorporates sillimanite, biotite and, in sample V132, plagioclase. Temperature of GP II is thus well constrained in all samples, whereas corresponding pressure is constrained for sample V132 only (Tables 5, A1 and A2, and Plate 1h). The third garnet phase corresponds to the garnet rims. In most garnets, zoning is more accentuated near the garnet extremities in contact with pressure shadow crystallization than in the garnet rims in direct contact with the surrounding foliation. This led us to define two distinct garnet phases. GP III corresponds to garnet rims and minerals in the foliation, whereas GP IV corresponds to garnet rims near pressure shadows and minerals in these pressure shadows. P-T conditions of GP III are well constrained as both biotite and plagioclase are found in the foliation while pressure of GP IV is only constrained for sample V132 (Tables 5, A1 and A2, and Plate 1h).

For some parageneses, using the same microprobe data, we calculated P-T estimates with Thermocalc [*Holland and Powell*, 1990] (Tables 5, A1 and A2). Most Thermocalc estimates tend to indicate a higher pressure range than the classical thermobarometry. This could reveal a tendancy of the *Ganguly and Saxena* [1984] calibration to underestimate pressures. However, the presence of cordierite at the rim of garnets in sample V1 indicates that this is not the case: the P-T conditions calculated by thermobarometry fall on the biotite + sillimanite <-> cordierite + garnet reaction curve (3 in Plate 1h) [*Powell and Holland*, 1990]. In all samples, Thermocalc and classical thermobarometry estimates are compatible if a low water activity (X_{H2O} between 0.5 and 0.3) is assumed (Tables 5, A1 and A2). This suggests the presence of nonhydreous fluids, most probably CO_2, during metamorphism. The presence
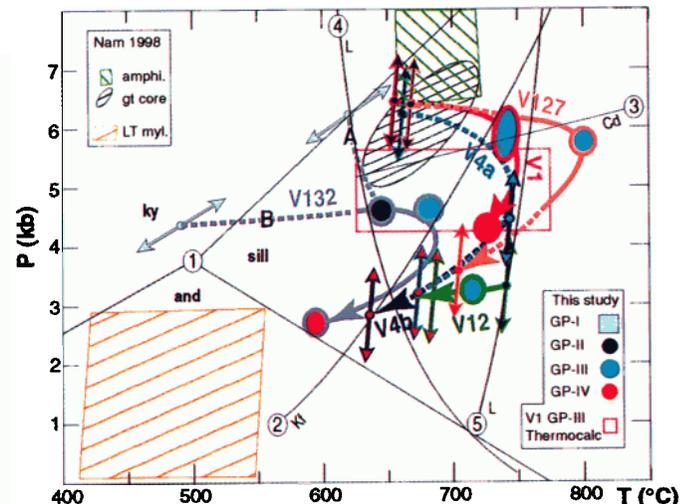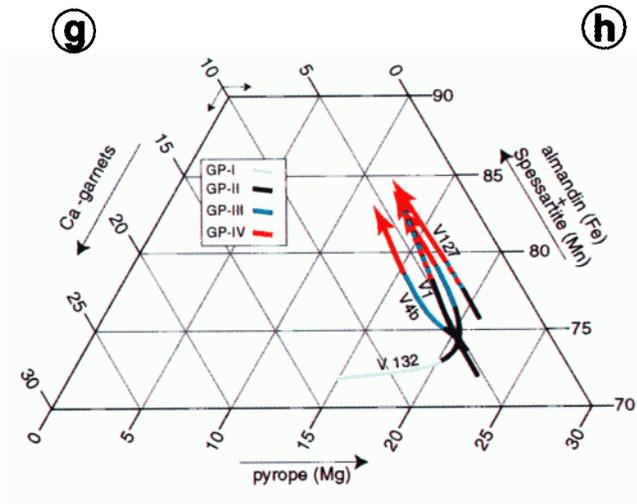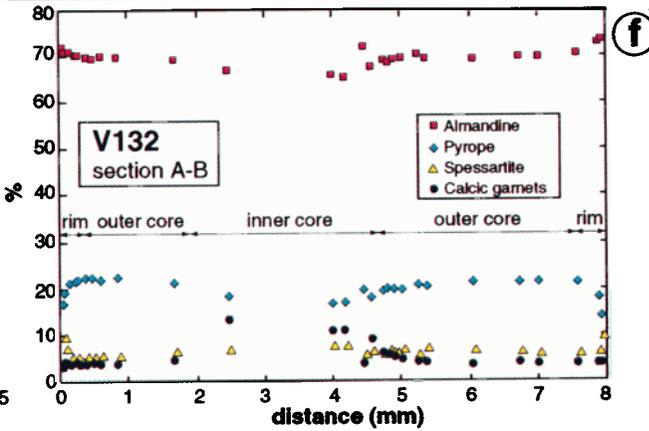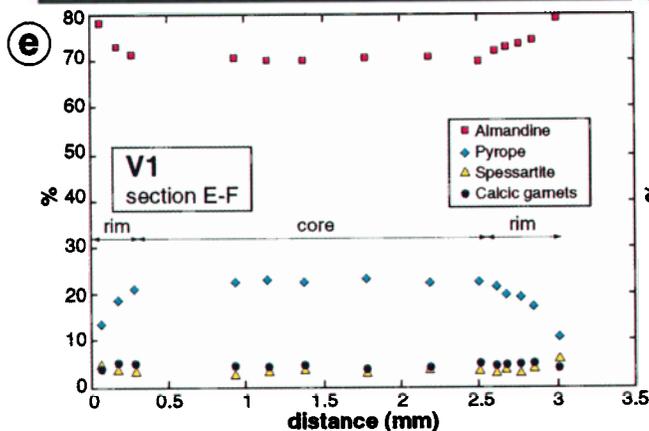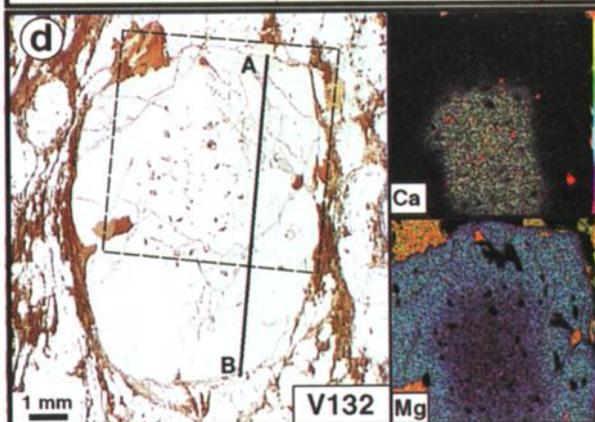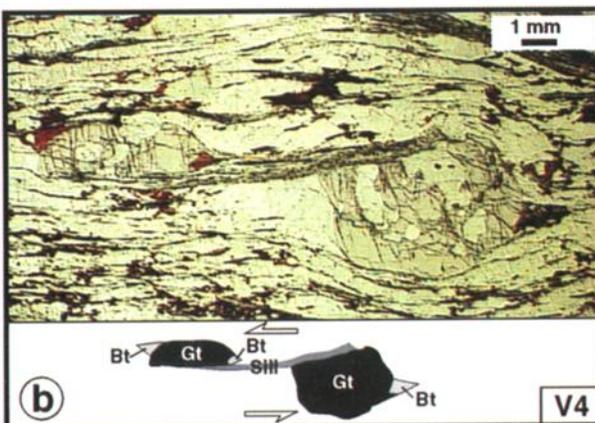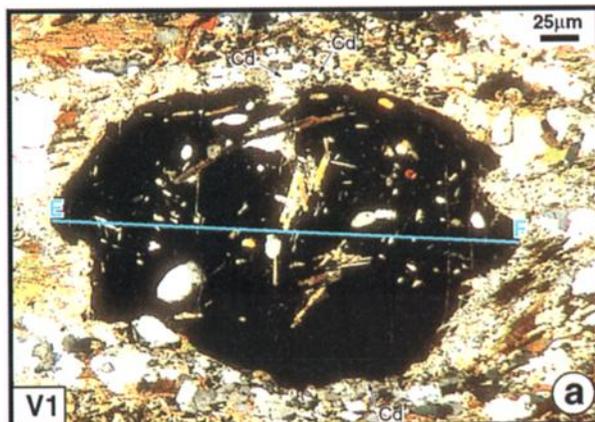
of a CO_2-rich fluid phase is consistent with the occurrence of numerous marble and ultramafic boudins within the shear zone where fluid circulation may have been strong as suggested by the presence of skarn in the Ailao Shan range [*Leloup and Kienast*, 1993].

The asymmetric shape of pressure shadows (e.g., Plate 1b) indicates that GP IV formed during shearing. The parallelism between the garnet rims and the foliation, and the fact that many garnets are elongated parallel to the stretching lineation strongly suggest that GP III was also synkinematic. In some cases, garnets are cut and offset by shear planes underlined by sillimanite (sample V4, Plate 1b), confirming that shear occurred at high temperature after the growth of these garnets. For example, the study of V4 shows that all garnet evolution (initial growth, shearing and asymmetric tail crystallization) took place at temperatures above 600°C (Plate 1b and 1h). With the lack of helicitic inclusions it is difficult to determine to what extent GP I and II developed during shearing. The existence of lower-grade mylonites [*Nam*, 1998b] and broken garnets indicates that deformation continued at lower temperatures (Plate 1h).

Taken all together, the samples from the DNCV tend to follow a clockwise P-T path at moderate pressure and high temperature (Plate 1h). This P-T path is not completely constrained as thermal or pressure constraints are lacking for some parageneses. More complex P-T histories might be proposed, such as an initial growth of garnets at higher pressures, but in the absence of evidence for a more complex P-T path we think that the rocks followed the P-T paths close to those depicted on Plate 1h (bold solid and dashed arrows). In particular, the heating phase between garnet cores and garnet rims and subsequent cooling from garnet rims to pressure shadows are seen in all samples exept V12, which shows continuous cooling. In the absence of any temperature constraint for the Ca-rich inner core of V132, two main P-T paths may be envisaged for this sample. The first one is that the inner core formed at P-T conditions close to those of the core of the other

garnets (including V127 located within few hundred meters at site G) and suffered less heating during decompression (path A, Plate 1h). The second one is that V132 inner core could be a relic from a previous metamorphic event. This second hypothesis (path B, Plate 1h) could explain why some oblique lineations are found at site G (Figure 13f).

A comparable study on four garnet-sillimanite micaschists from the central DNCV by *Nam* [1998b] found three P-T stages (Plate 1h). The first stage corresponds both to the garnet cores of garnet-sillimanite gneiss and to an amphibolite gneiss. These two parageneses give P-T estimates of $6.2^{+1.4}_{-1.7}$ kbar and 690^{+30}_{-60}°C, and 7.3 ± 0.9Kb and 690 ± 28°C, respectively. These estimates are close to those that we calculated in the garnet cores of samples V1, V4a, and V127 (Plate 1h). According to *Nam* [1998b], P-T conditions of the second stage that corresponds to the garnet rims do not differ significantly from those of the first stage. However, because the samples he used retrogressed, he concluded that the P-T estimate of the second stage probably has no significance. The third stage occurs in lower-grade mylonites and yields temperatures between 400°C and 560°C and pressures lower than 4 kbar (Plate 1h). *Nam* [1998b] also noted that the reaction muscovite + quartz <-> K-feldspar + AlSi + H_2O occurred along both the prograde and retrograde parts of the P-T path.

The results we present in this study together with those of *Nam* [1998b] allow us to propose the following P-T path for the DNCV (Plate 1h, Figure 17c). After an initial heating phase, conditions corresponding to an average vertical temperature gradient of ≈40°C/km were reached during left-lateral shearing. In a water-saturated environment, such P-T conditions should yield extensive partial melting (Plate 1h, Figure 17c). In the DNCV, probably due to reduced water activity, such conditions only induced local partial melting by biotite breakdown (Figure 17c). As shearing and denudation continued, temperature decreased gradually leading to an even higher apparent averaged vertical gradient of ≈65°C/km. Those high gradients are equal to, or greater than, those documented in the

Plate 1. (opposite) Petrology of DayNuiConVoi range. (a to d) Garnets from the DNCV. (a) Sample V1 (site F, Figure 4). Polished thin section under crossed nichols. E-F designate cross section the composition of which is detailed on Plate1e; note sillimanite crystals incorporated within garnet. (b) Sample V4 (site E3, Figures 12 and 14). (top) Polished thin section. (bottom) Sketch showing garnet cut by top to the south (left-lateral) sillimanite shear plane. (c) Polished slab of sample V5 (site E3). Note the elongated garnets with biotite tails and the leucosomes parallel to foliation both implying high-temperature shear. (d) Sample V132 (site G2, Figure 4). (left) Polished thin section; A-B designate cross section the composition of which is detailed on Plate 1f; dashed box corresponds to the composition maps shown on the right. (right) X-ray calcium and magnesium maps (color tables on the right, with higher contents on top). Note thin Mg-poor rim and Mg-poor and Ca-rich central inner core that contains many small inclusions. (e to h) Garnet composition from microprobe measurements. (e) Garnet composition along section E-F, sample V1. (f) Garnet composition along section A-B, sample V132. (g) Garnet compositions from core to rim, plotted in a pyrope/almandine + spessartite/calcic garnet ternary diagram showing four garnet phases (GP). See text for details. (h) P-T paths deduced from thermobarometry using garnets compositions (Tables 5, A1 and A2). P-T paths for each sample are represented by the large colored arrows. Circles represent points where both pressure and temperature are constrained by the gt-bt thermometer [*Hodges and Spear*, 1982] and the q-sill-gt-pl thermobarometer [*Ganguly and Saxena*, 1984]. Colors of circles correspond to garnet phase (same colors as Plate 1g). Dashed parts of P-T paths are only constrained by one thermobarometer (small divergent arrows indicate in which directions P-T estimate can be shifted). For samples V4a and V4b the absence of plagioclase precludes any pressure estimate. The light blue frame represents V1 garnet rim (GP III) P-T estimate with Thermocalc [*Holland and Powell*, 1990]. P-T estimates of *Nam*, [1998b] are also shown. Simplified petrogenetic grid: (1) kyanite (ky) - sillimanite (sill) - andalusite (and) triple point [*Spear and Cheney*, 1989]; (2) muscovite + quartz > aluminosilicate + K-feldspar [*Spear and Cheney*, 1989]; (3) biotite + sillimanite > cordierite + garnet [*Powell and Holland*, 1990]; (4) H_2O saturated pelite solidus [*Thompson*, 1982]; (5) biotite + aluminosilicate + plagioclase + quartz > garnet + K-feldspar + liquid [*Le Breton and Thompson*, 1988]. See text for details.

other metamorphic ranges of the ASRR: from 22 to 34°C/km in the DianCang Shan and ≈40 to 60°C/km in the Ailao Shan (Figure 17); [*Leloup et al.*, 1993; *Leloup and Kienast*, 1993]. *Leloup et al.* [1999] interpreted these high gradients as resulting from the combination of shear heating and upward heat advection along a lithospheric strike-slip fault zone.

6.3. Thermochronology of the DNCV Range

The $^{40}Ar/^{39}Ar$ results obtained for the DNCV are summarized in Table 6 and Figure 18.

6.3.1. BaoYen section (section D).

K-feldspar from sample V12 yields an age spectrum reflecting two cooling events (Table 6, Figure 18a). The first 18 steps, corresponding to furnace temperatures below 850°C, show a sawtooth-like age spectrum classical for two-stage isothermal stepwise heating (Figure 18a). The first-stage steps are affected by strong excess argon ($^{40}Ar/^{36}Ar_i \approx 830$) and give progressively younger ages, whereas the second-stage steps are much less affected ($^{40}Ar/^{36}Ar_i \approx 330$) and show remarkably constant ages (22.8±0.2 Ma. on average, Table 6 and Figures

Table 5. DayNuiConVoi Garnet-Sillimanite Micaschists Thermobarometry Results[a]

Section	GP[b]	Equilibrium gt-bt			Equilibrium gt-pl-sill-q			Intersection[d]	Thermocalc	
Site		E.L.[c]	T, °C (P= 0kb)	T, °C (P=10kb)	E.L.[c]	P, kbar (T= 0°C)	P, kbar (P=1000°C)	gt-bt and gt-pl-sill-q	Phases[e]	Best Result[f]
				V12						
Section D Site D2 Figures 12 and 14	II	N=2 Min Max average	705 730 717	748 774 761	no plagioclase				no calculation	
	III	N=2 Min Max average	689 698 694	732 741 736	N=1	-3.76	6.1	N=1 707°C, 3.2 kbar	gt + bt + pl + q+sill+Kf+H₂O+CO₂	average P-T T=678±76 °C P=6.3±2.8 kbar XH₂O=0.2
	IV	N=3 Min Max average	649 690 672	690 733 714	no plagioclase				no calculation	
				V4a						
Section E Site E3 Figures 12 and 14 Plate 1b	II	N=5 Min Max average	609 672 640	648 713 680	no plagioclase				no calculation	
	III	N=6 Min Max average	646 754 689	687 799 732	no plagioclase				no calculation	
	IV	N=9 Min Max average	627 706 660	667 749 701	no plagioclase				no calculation	
				V4b						
Section E Site E3 Figures 12 and 14	III	N=2 Min Max average	720 725 722	764 768 766	no plagioclase				no calculation	
	IV	N=2 Min Max average	597 651 524	635 692 663	no plagioclase				no calculation	
				V1						
Site F Figure 4 Plates 1a and 1e	II	N=3 Min Max average	617 644 631	657 685 671	no plagioclase				no calculation	
	III	N=4 Min Max average	706 728 719	749 772 777	N=2 Min Max average	-4.1 -4.14 -4.12	10.2 8.66 9.42	N=2 733°C, 6.37 kbar 752°C, 5.49 kbar 746°C, 597 kbar	gt+bt+pl+cord+Kf+ q+sill+H₂O+CO₂	average P-T T=697±68 °C P=4.9±0.7 kbar XH₂O=0.5
	IV	N=3 Min Max average	708 779 732	752 826 777	N=1	-5.9	9.95	N=1 727°C, 4.3 kbar	no calculation	

Table 5. (continued)

Section / Site	GP[b]	Equilibrium gt-bt E.L.[c]	T,°C (P= 0kb)	T,°C (P=10kb)	Equilibrium gt-pl-sill-q E.L.[c]	P, kbar (T= 0°C)	P, kbar (P=1000°C)	Intersection[d] gt-bt and gt-pl-sill-q	Thermocalc Phases[e]	Best Result[f]
					V132					
Site G1 Figure 4 Plates 1d and 1f	I	no biotite			N=3 Min Max average	-2.81 -2.56 -2.66	10.84 11.99 11.66		no calculation	
	II	N=6 Min Max average	612 726 658	651 770 700	N=2 Min Max average	-3.2 -3.2 -3.2	8.5 8.7 8.6	N=1 645°C, 4.3 kbar	gt + bt + pl + q+sill+Kf+H₂O+CO₂	average P-T T=717±82 °C P=6.1±2.4 kbar XH₂O=0.3
	III	N=7 Min Max average	648 747 672	689 792 714	N=4 Min Max average	-3.68 -3.91 -3.8	7.33 8.9 8.28	N=2 666°C, 4.65 kbar 693°C, 4.75 kbar	gt + bt + pl + q+sill+Kf+H₂O+CO₂	average P-T T=687±73°C P=6.3±2.4 kbar XH₂O=0.3
	IV	N=5 Min Max average	581 692 654	619 750 698	N=2 Min Max average	-4.36 -4.59 -4.47	6.79 7.76 7.28	N=1 590°C, 2.7 kbar	gt + bt + pl + q+sill+Kf+H₂O+CO₂	average PT T=631±60°C P=5.7±2.1 kbar XH₂O=0.2
					V127					
Site G2 Figure 4	II	N=4 Min Max average	619 668 648	659 710 689	no plagioclase				no calculation	
	III	N=3 Min Max average	640 767 721	680 813 765	N=1	-4.1	8.4	N=1 793C, 5.8 kbar	gt + bt + pl + q+sill+Kf+H₂O+CO₂	no satisfying result
	IV	N=3 Min Max average	613 728 689	652 773 732	no plagioclase				no calculation	

[a]For a synthesis of these results see Plate 1h.

[b]GP : Garnet Phase. See plate 1g and text.

[c]E.L. : Equilibration lines. N= number of equilibration lines calculated. Min, Max and average correspond to the lower temperature (or pressure), higher temperature (or pressure) and mean equilibration line respectively.

[d]The intersection between gt-bt and gt-pl equilibrium lines are for a single gt measurement and not for averaged results.

[e] Phases considered for thermocalc calculations. Top line corresponds to phases whose composition was measured by microprobe analysis while phases of the bottom line were not measured.

[f]Best Thermocalc results with from top to bottom : method used, temperature range, pressure range and H₂O activity.

18a and 18b). Then the ages rise rapidly to reach a rough plateau of 39.5±0.6 Ma (HT, steps 26 to 36, Table 6 and Figure 18a). This plateau starts with a small age bump suggestive of excess argon [*Foster et al.*, 1990]. Indeed, an inverse isochron of the plateau high T° steps suggests excess argon and an age of 37.4 ± 0.4 Ma, which we consider as the maximum age for the high T° portion of the sample (HT, steps 32 to 36, $^{40}Ar/^{36}Ar_i$ = 335±4, Table 6 and Figure 18c). Such results suggest two phases of rapid cooling, the first one occurring later than 37 Ma and the second one at ≈23 Ma. Multidomain diffusion model assuming eight domains with a common activation energy of 59.63 kcal/mol and $\log(D_0/r_0^2)$=9.172 (Figure 18k), yields a cooling history with rapid cooling at 42 and 23 Ma (Figure 18e), which correctly fits the data except the small bump at the begining of HT rough plateau (Figure 18f). Because of excess argon in the HT plateau and the very high activation energy used, only the younger part of this cooling history is reliable, and the HT

cooling could have occurred later than 42 Ma (Figure 18d). Three biotite fractions from the same sample give an average total fusion age of 23.1±0.4 Ma (Table 6). This age is compatible with the K-feldspar model cooling history (Figure 18d). Biotite fractions from samples V18 and V20 yield average total laser fusion ages of 23.9±0.2 and 23.4±0.1, respectively (Table 6 and Figure 18d).

6.3.2. LucYen. It is difficult to reach primary deposits where rubies are still in place because of dense forest and extensive removal by local people. To date the metamorphism related to pegmatite intrusions and ruby crystallization in LucYen area, north of the DNCV range, we used sample V161 acquired in LucYen from local merchants. This sample contains the typical paragenesis calcite + corundum (ruby) + phlogopite + graphite that we have observed in place in the large marbles boudins south of LucYen (Figure 12). The phlogopites from V161 yielded a plateau age of 33.5±0.7 Ma (Table 6, Figure 18e).
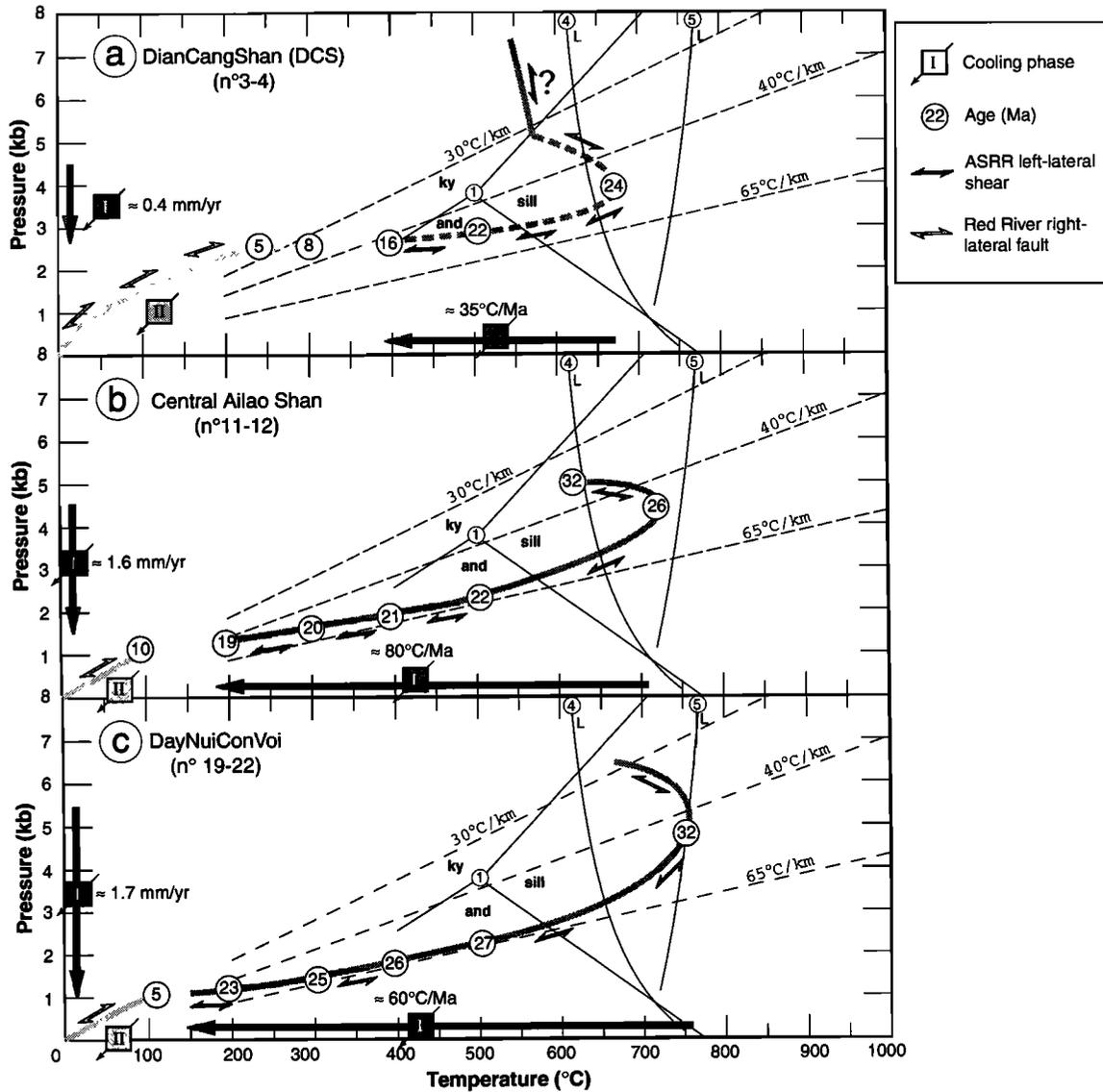
Figure 17. P-T-t-deformation paths in the ASRR. (a) DianCang Shan range. (b) Central Ailao Shan range. (c) DayNuiConVoi range. Built from combination of Plates 1h and 2b (this study), *Leloup and Kienast* [1993], and *Leloup et al.* [1993]. Large arrows parallel to temperature and pressure axis, respectively, show cooling and decompression during cooling phase I. Circled numbers are time estimations (Ma). Small arrows show shear sense at that time: sinistral (dark) or dextral (light shading). Aluminosilicate triple point and partial melting curves 4 and 5 are as in Plate 1.

6.3.3. YenBai section (section E). Sample V4 contains K-feldspar and biotite. K-feldspar shows an age spectrum comparable to V12Kf described above (Table 6 and Figure 18f). The average age of the second-stage isothermal steps at low furnace temperatures is 23±0.1 Ma. This age is close to the isochron ages of both most of the first-stage isothermal steps and the second-stage isothermal steps (LT, Table 6 and Figure 18g). The age bump, located at 29% of gas release (step 29), culminates at 28.75 Ma before a progressive decrease in age with a small plateau at 27±0.1 Ma, corresponding to 34% of gas release (steps 35 to 39). On an inverse isochron plot, these steps do not show excess argon (HT, Table 6, Figure 18g). Modeling of the data assuming eight diffusion domains fits both to the Arrhenius plot and the age spectrum if rapid cooling takes place at 27.5 and 23 Ma (Figure 18f, 18h and

18i). Note that as for V12, the model does not fit the small age bump at the begining of HT plateau (Figure 18f). Coexisting biotites give a total laser fusion age of 24.9±0.2 Ma compatible with this model cooling history (Table 6 and Figure 18i).

6.3.4. BaiBang (site F). V1 K-feldspar has an age spectra similar to V4 and V12 (Figure 18j). Perturbations at 17 and 22% gas release (steps 14 and 18) are due to analytical problems. The average age of low temperature second-stage isothermal steps is 22.5±1 Ma (LT2, Table 6 and Figure 18j). Such an age is comparable to the low furnace temperature first stage steps isochron age (LT1, Table 6 and Figure 18k). The age bump culminates at 27 Ma. The following plateau corresponding to 24% of gas release has an age of 25.8±0.1 Ma (HT, Table 6 and Figure 18j). The inverse isochron of steps 30 to 42 (36% of gas release) gives 25.6 ± 0.5 Ma (HT, Table 6

Table 6. DayNuiConVoi range ^{40}Ar/^{39}Ar Results

Section/Site	Sample		Lab[a]	Mineral	Plateau Age		Inverse Isochron Age				Reference
	Number	Location			Age[b], Ma	Steps	Age, Ma	^{40}Ar/^{36}Ar$_i$	MSWD[d]	Steps	
Bao Yen section (section D)	V12	22°13'27"N 104°27'17"E Figures 12 and 13	UCLA	biotite	23.1±0.4[c]	mean of three laser total fusions	20.4 ± 0.6	831 ± 49	113	first stage steps from 7 to 17 44% of gas	Harrison et al. [1996]
			UCLA	Kf	LT1	no plateau	22.6 ± 0.3	329±21	47	second stage steps from 6 to 18 12.9 % of gas	this study
					LT2: 22.8±0.2[c]	second stage steps from 6 to18 12.8 % of gas					
					HT: 39.5± 0.6	11 steps/42 (26-36) 44% of gas	37.4 ± 0.4[c]	335 ± 4	4.3	5 steps/42(32-36) 23% of gas	
	V20	22°10'55"N 104°22'05"E Figures 12 and 13	UCLA	biotite	23.4±0.1[c]	mean of three laser total fusions					Harrison et al. [1996]
	V18	22°10'50"N 104°21'56"E Figures 12 and 13	UCLA	biotite	23.9±0.2[c]	mean of three laser total fusions					Harrison et al. [1996]
Luc Yen	V161	Luc Yen see text	UBP	phlogopite	33.5±0.7[c]	3 steps/6 (3-5) 98% of gas					this study
Yen Binh (section E)	V4	≈21°47'10"N ≈104°54'15"E Figures 12 and 13	UCLA	biotite	24.9±0.2[c]	mean of three laser total fusions					Harrison et al. [1996]
			UCLA	Kf	LT1	no plateau	21.7 ±0.7	757±84	189	first stage steps from 4 to 12 5.3% of gas	this study
					LT2: 23± 0.1[c]	second stage steps from 7to13 6 % of gas	22.7± 0.3	299±12	21	second stage steps from 3 to 11 5.2 % of gas	
					HT: 27± 0.1[c]	5 steps/43 (35-39) 33.5 % of gas	27.3 ± 0.3	298.5 ± 5	33	6 steps/43(34-39) 35.6% of gas	
Bai Bang (site F)	V1	21°24'20"N 105°18'39"E Figure 4	UCLA	biotite	24.1±0.1[c]	mean of three laser total fusions					Harrison et al. [1996]
			UCLA	Kf	LT1	first stage-steps: no plateau	23.9± 0.3	340±8.4	4.9	first stage steps from 3 to 9 4.2% of gas	this study
					LT2: 22.5 ± 1[c]	second stage steps from 6 to 12 6 % of gas	21.9± 0.2	298± 8	4	second stage steps from 2 to 10 10 % of gas	
					HT: 25.8± 0.1[c]	7 steps/42 (32-38) 24 % of gas	25.6± 0.5	297 ± 3	59	20 steps/42(30-42) 36 % of gas	
NinhBinh (site G)	V126	20°19'47"N 106°04'34"E Figure 4	UBP	biotite	27.4±0.6	88% of gas 6 steps/12	27.4±0.3[c]	303±3	4.2	9 steps/12 -1,11,12 99.5% of gas	this study

[a] UBP, Université Blaise Pascal, Clermont Ferrand, UCLA, University of California, Los Angeles.
[b] LT, low furnace temperature (400-700°C) age, LT1, first stage isothermal steps, LT2, second stage isothermal steps, HT, high furnace temperatures (1000-1200°C) age.
[c] Preferred age.
[d] MSWD : mean square weighted deviation.

a V12 K-feldspar age spectra

HT: 39.5 ± 0.6

age spectrum
model

LT 2nd stage steps: 22.8 ± 0.2

Age (Ma)

cumulative ^{39}Ar released (%)

b V12 K-feldspar inverse isochrones

air

HT: ^{40}Ar/^{36}Ar$_i$ = 335±4
37.4 ± 0.4 Ma

LT 2nd stage steps: ^{40}Ar/^{36}Ar$_i$ =329±21
22.6 ± 0.3 Ma

LT 1st stage steps: ^{40}Ar/^{36}Ar$_i$ = 831±49
20.4 ± 0.6 Ma

^{36}Ar/^{40}Ar

^{39}Ar/^{40}Ar

c V12 K-feldspar Arrhenius plot

sample

59.63 kcal/mol
log(D0/r02)=9.172
model

log D / r^2 (s^{-1})

10000 / T (1/°K)

d section D cooling history ⑲

19B
V12
6
V20
V12
V18
19B
V12
19B
V12-HT
?
V12

Temperature (°C)

Time (Ma)

	section D	site RR19	site RR6
amphibole	V12	19B	6 (K/Ar)
biotite	V18		
K-feldspar model	V20	(Wang et al. 1998)	(Nam 1998b)
K-feldspar			

e V161 phlogopite age spectrum

33.5 ± 0.7

Age (Ma)

cumulative ^{39}Ar released (%)

f V4 K-feldspar age spectra

29
35
39
HT: 27 ± 0.1

sample
model

LT 2nd stage-steps: 23± 0.1

Age (Ma)

cumulative ^{39}Ar released (%)

g V4 K-feldspar inverse isochron

air

HT: ^{40}Ar/^{36}Ar$_i$ = 298.5±5
27.3 ± 0.3 Ma

LT 1st stage steps: ^{40}Ar/^{36}Ar$_i$ = 707±28
21.7 ± 0.7Ma

LT 2nd stage steps: ^{40}Ar/^{36}Ar$_i$ = 292±2
22.7 ± 0.3 Ma

^{36}Ar/^{40}Ar

^{39}Ar/^{40}Ar

Figure 18. The ^{40}Ar/^{39}Ar data from DayNuiConVoi range. Results are summarized in Table 7, samples are located on Figures 12 and 14. (a, e, f, j, l) Conventional age spectra. In the case of K-feldspar, model age spectra are also shown. (b, g, k, m) Inverse isochrons. Each step is plotted with corresponding error bars and step number, the drawn regression line corresponds to the calculated age and ^{40}Ar/^{36}Ar$_i$. Step numbers in shaded boxes were not used for calculations. (c, h) K-feldspar Arrhenius plots showing both experimental data and models (see text for details). (d, i, n) Local cooling histories deduced from the geochronological results. Circled numbers refer to site numbers on Plate 2. Large shaded lines represent preferred T-t histories.

Figure 18. (continued)

n° on Plate2 ▷ **19** **20** **21** **22**

NW SE

All K/Ar and $^{40}Ar/^{39}Ar$ ages

amphibole □
biotite ○
muscovite △
Kf HT cooling +
Kf LT rapid cooling ◇
Wang et al. 1998 ($^{40}Ar/^{39}Ar$)
◇ Nam 1998b (K/Ar)
◆ This study ($^{40}Ar/^{39}Ar$)

(a) ± 0.5 Ma

Age (Ma)

≈ 250°c
≈ 150°c

selected K/Ar and $^{40}Ar/^{39}Ar$ ages

(b) ≈ 450°c
≈ 350°c
≈ 250°c
≈ 150°c

Age (Ma)

Distance along strike (km)

220 210 200 190 180 170 160 150 140 130 120 110 100 90 80 70 60
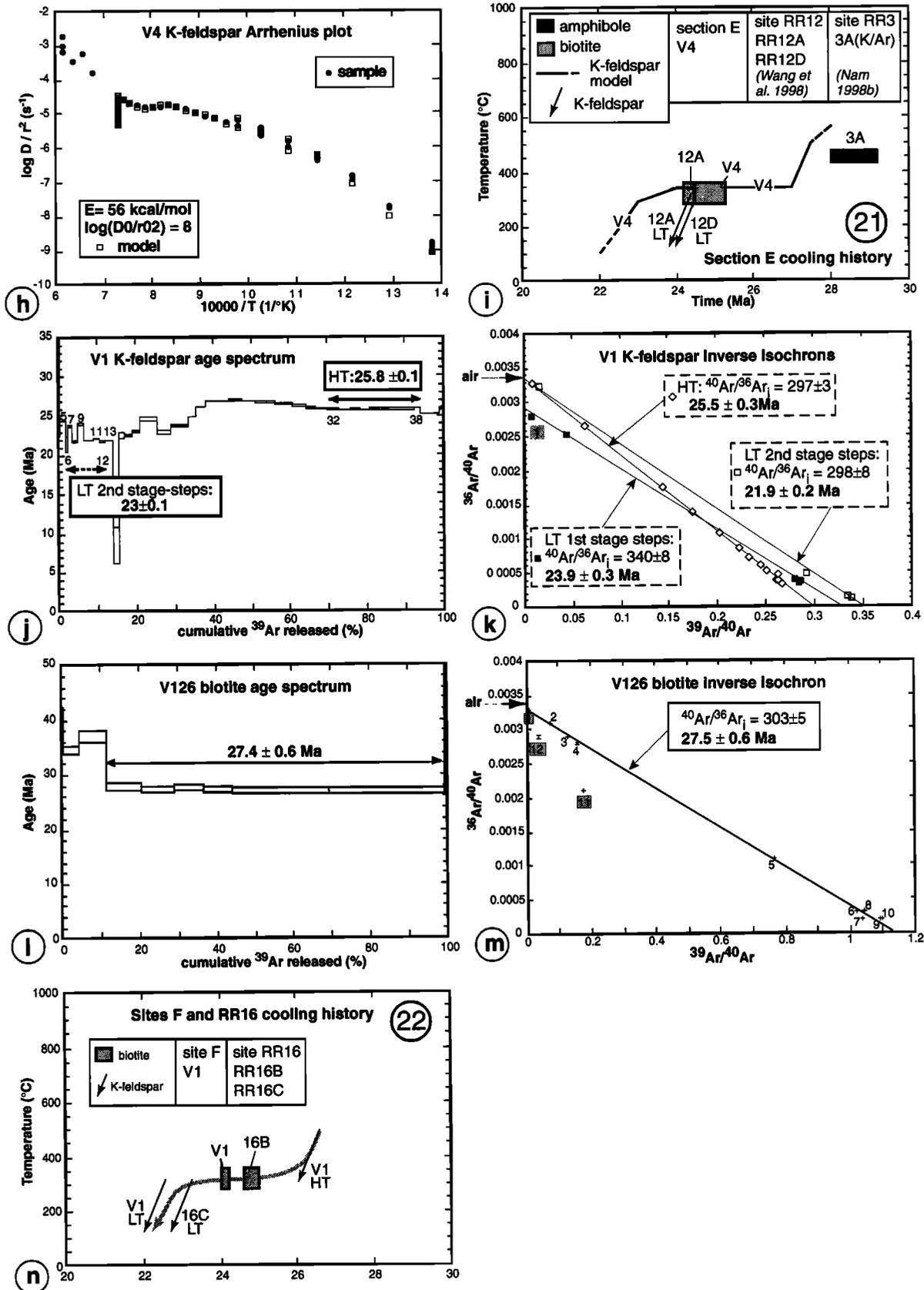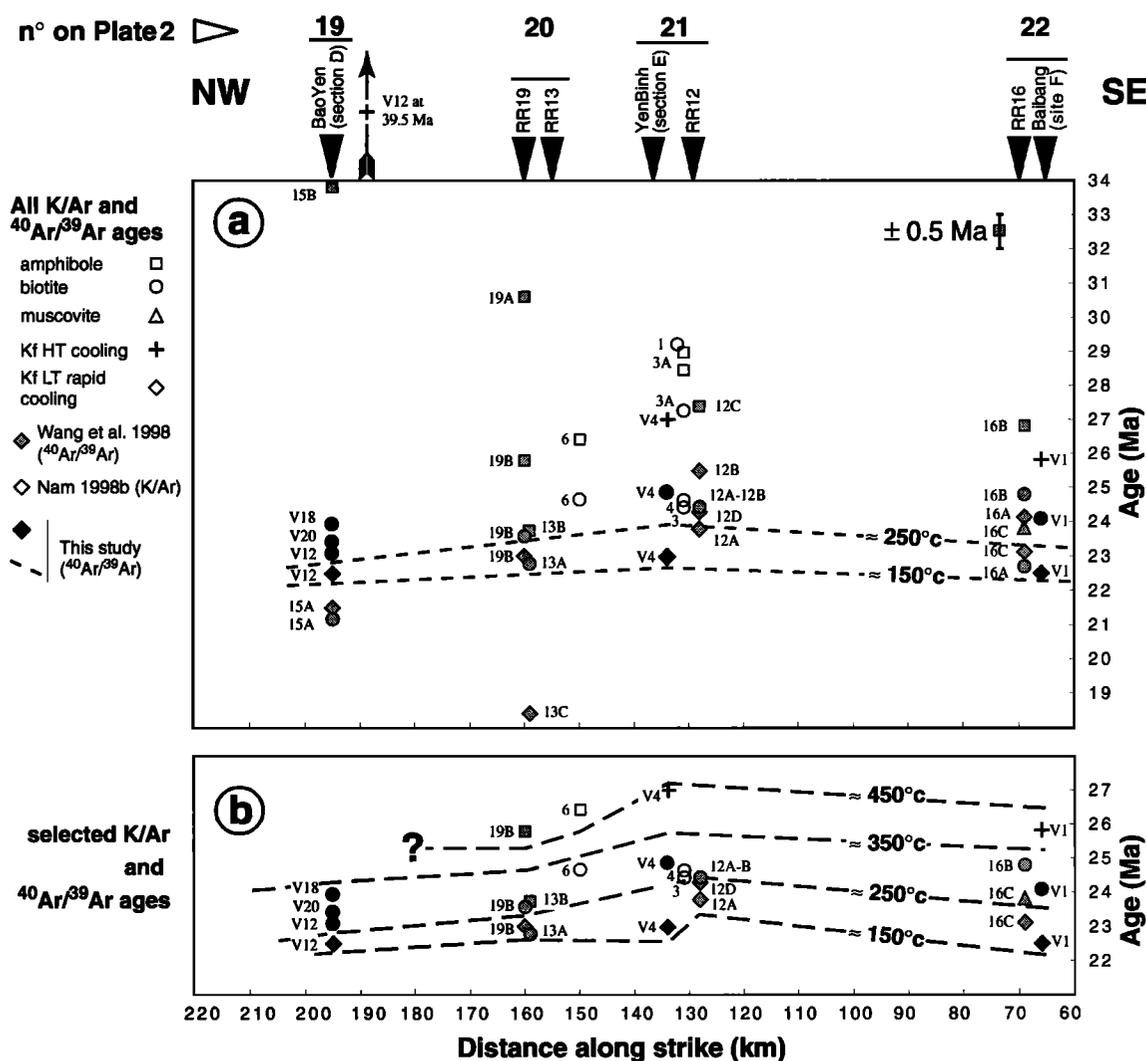
Figure 19. Summary of thermochronological data from central DayNuiConVoi range. Mineral ages are plotted as a function of distance along ASRR taken from a reference point at Hanoi. Data are from this study (solid symbols), Nam [1998b] (shaded symbols) and Wang et al., [1998] (open symbols) (Table 7). (a) All data; most uncertainties are smaller than ±0.5 Ma (Table 7). (b) Selected data with the proposed ≈450°, ≈350°, 250°C, and 150°C time-space isotherms (dahed lines); see text for details.

and Figure 18k). The above mentioned analytical problems do not affect the interpretation of the age spectrum, which suggests rapid cooling at ≈26 and ≈23 Ma (Figure 18n), but preclude calculation of any diffusion model. Biotites from the same sample give a total laser fusion age of 24.1±0.1 Ma (Table 6 and Figure 18n).

**6.3.5. Outcrops east of NinhBinh (site G).** Biotites from sample V126 show a flat age spectrum of 27.4±0.6 Ma (Figure 18l) with slight excess argon: An inverse isochron age of 27.4±0.3 for $^{40}Ar/^{36}Ar_i = 303±3$ can be calculated for all steps but the first and two last ones (Figure 18m).

6.3.6. Cooling history of the DNCV range. The $^{40}Ar/^{39}Ar$ ages presented above from the DNCV span from ≈37 to 22 Ma with all but two younger than 28 Ma (Table 6). Such ages confirm the Oligo-Miocene cooling of the range previously detected [Harrison et al., 1996; Nam, 1998b; Wang et al., 1998]. On Figure 19a, we have plotted all available K/Ar and $^{40}Ar/^{39}Ar$ ages as a function of the distance along strike

from a reference point located at Hanoi. On such a plot, minerals from the same locality plot on the same vertical line. If ages correspond to the time of cooling below a given closure temperature, the minerals having higher closure temperature should be older than those having a lower temperature. On a vertical line, the minerals should thus follow a logical order with closure temperature decreasing from top to bottom, i.e., amphiboles (≈510°C), biotites (≈320°C), and LT K-feldspar (300-150°C). If the data are coherent on a regional scale, it is possible to draw isothermal lines that represent the along-strike timing of cooling through a given temperature. Note that samples from various sites along a cross section of the range share the same distance along strike and thus also plot on the same vertical line. As samples located far from each other may have cooled at different times (across-strike diachronism), plotting them together may disturb the logical succession order. This is not the case in the central DNCV, where the only two samples from the SW side of the range (V18 and V20) give nearly the same age as V12 from the same

section but on the NE side (Figures 12 and 14). From the results of this study alone, the 250°C and 150°C isotherms can be drawn (dashed lines on Figure 19a). However, if all other published K/Ar and ^{40}Ar/^{39}Ar ages are taken into account, it is not possible to draw simple isothermal lines. This can be due to several reasons: (1) ages do not correspond to their a priori closure temperature or different samples of the same mineral species have different closure temperature, (2) the thermal structure of the range was complex and isotherms were convoluted, and (3) there are problems with some of the data. We will show below that discrepancies are mostly due to the third reason and that first-order isothermal lines can be drawn at the scale of the range for temperatures below 450°C.

Wang et al [1998] published ^{40}Ar/^{39}Ar ages from four localities along the NE side of the central DNCV (from our site F to section D): Six amphibole ages spanning from 33.8 to 23.7 Ma, seven biotite ages spanning from 24.8 to 21.2 Ma, a white mica yielding 23.8 Ma, and 10 K-feldspar with low-temperature plateau ages spanning from 25.5 to 18.4 Ma (Figure 19a). They concluded that the DNCV suffered slow cooling from ≈34 to 25 Ma followed by rapid early Miocene cooling (25-21 Ma) and that this cooling was diachronous along strike, becoming progressively younger toward the NW as in the Ailao Shan range [*Harrison et al.*, 1996]. However, a careful look at their data reveals several problems. First, many of the plateau ages (e.g., amphiboles) are dubious, and no detailed discussion on the isochron results was provided. Second, in some cases, the results on different minerals from a given sample are contradictory (i.e., biotites younger than the low T° rapid cooling deduced from the K-feldspars). Third, all K-feldspars measured by *Wang et al.* [1998] show flat age spectra, suggesting very rapid cooling from high ≈400°C to ≈150°C. However, the timing of this rapid event varies significantly from sample to sample even at the same locality. Fourth, the standard they used is much older than the ages obtained from DNCV samples (LP-6 biotite, 127.7±1.4 Ma). We thus chose to select from the data of *Wang et al.* [1998] only those without apparent contradiction between different minerals in the same sample and with a good age spectrum. The selected data are coherent with each others except for site RR13 which gives ages ≈1 Myr younger than the nearby site RR19.

On Figure 19b we propose simple time/space domains that fit all selected data of *Wang et al.* [1998] except those of site RR13 and muscovite RR16c. This interpretation suggests that rapid cooling below ≈250°C at ≈23 Ma was relatively synchronous along strike. The K/Ar data of Nam [1998b] are consistent with this interpretation, the only incompatible samples (biotites 1 and 3A) being those for which the author specified impure separates. At locality RR12 the cooling seems to have occurred a bit earlier (≈24 Ma) than in the other localities. It is difficult, however, to determine if this age difference is an artifact or if it reflects a local perturbation in the timing of cooling. Biotite from site G, far to the SE (Figure 4 and 23 on Plate 2), is significantly older than most biotites within the range. In the absence of other data from this site it is difficult to decide if this age trend is meaningful (Plate 2b). Note that we consider that all ^{40}Ar/^{39}Ar ages are cooling ages, whereas some of them could be recrystallization ages acquired below the blocking temperature. This could be the case for muscovite RR16C which gives an age of 23.8±0.2 Ma, a time at which the temperature was only ≈300°C in locality RR16 according to our analysis. A close look at all published K/Ar and ^{40}Ar/^{39}Ar data from the DNCV thus shows that this range cooled from ≈350°C to below 150°C between 25 and 22 Ma.

In the absence of U/Pb data the cooling history above 350°C is only constrained by the ^{40}Ar/^{39}Ar HT K-feldspar (450-300°C) and amphibole (510±50°C) ages. The most reliable ^{40}Ar/^{39}Ar amphibole age is that of 25.8±0.3 Ma for RR19B [*Wang et al.*, 1998], which suggests that high temperatures were maintained in the DNCV until ≈26 Ma, in relatively good agreement with V4 and V1 ^{40}Ar/^{39}Ar HT K-feldspar ages (Figures 18e and 19b). Amphibole 13B (23.7±0.2 Ma [*Wang et al.*, 1998]) is abnormally young, as are the other results from the same site (see above). The simplest interpretation of all the published ^{40}Ar/^{39}Ar data is that the entire DNCV was above ≈450°C until ≈27 Ma, at which time it started to rapidly cool (Figure 19b). All the P-T paths documented by thermobarometry (Plate 1h) would have thus taken place prior to 27 Ma. Few data correspond to ages older than 27 Ma. These data suggest that temperatures not much higher than 450°C would have lasted for several milion years before final cooling (Figure 19a). These data are, however, all of low quality (amphiboles RR19A, RR15B, and RR3A) or clearly affected by excess argon (V12 HT K-feldspar) and have probably little geologic meaning. A possible explanation could be that some of these data correspond to boudins within which older ages could have been partly preserved.

North of the central DNCV in the LucYen marbles, where fluid circulation was associated with phlogopite and ruby crystallization, V161 phlogopites yield an early Oligocene age (33.5±0.7, Table 6 and Figure 18a). We interpret this age as that of the metamorphism and/or metasomatism responsible for ruby crystallization. This supports the hypothesis of very hot fluid or magma generation in the DNCV shear zone prior to 30 Ma.

7. Discussion: Geometry and Timing of the Ailao Shan-Red River Transform

Ductile deformation in the DNCV is quite similar to that in the other ranges of the ASRR and indicates left-lateral shear parallel to the belt. The main difference is that foliations are often flatter in the DNCV. This could be due to a larger component of transtension during the strike-slip movement. Along most of the ASRR, left-lateral shear occurred under high-grade conditions, compatible with crustal melting. In the DNCV the average vertical gradient reached values close to 65°C/km during left-lateral deformation, the highest documented in the ASRR. This is again compatible with a larger component of transtension toward the SE. In all ASRR ranges, cooling from high temperature is younger than 34 Ma. This suggests that these ranges share a common geodynamic history even if a closer look reveals that each one has its own unique cooling history (see discussion in section 7.1). The fact that the DNCV lies in the same direction as the Ailao Shan range is not fortuitous but reflects that it belongs to the same large structure that extends at least from 27°20'N latitude (XLS range) to 21°20'N (site F). Toward the south, this structure probably lies below the Quaternary Hanoi basin, emerges at site G, and then enters the YinGeHai basin (Figure 4). Toward the NW, evidence for strike-slip faulting has been found as far as 28°40'N [*Leloup et al.*, 1995]. The total documented length of the ASRR thus reaches nearly 1100 km, a length comparable to the North American San Andreas and Turkish North Anatolian faults.

Many authors now agree that large left-lateral displacements took place along the ASRR during the Tertiary [e.g., *Leloup et al.*, 1995; *Lee and Lawver*, 1995; *Chung et al.*,

1997; *Wang and Burchfiel*, 1997]. However, the precise timing of shearing, the total amount of displacement, its variation along strike, and the connection of the continental fault with seafloor spreading in the South China Sea are still controversial issues that we address in the following.

7.1. Timing of Left-Lateral Shear Along the ASRR

Knowledge of the timing of left-lateral shear comes from the geochronological data on the metamorphic and plutonic rocks of the ASRR belt. More than 20 U/Pb ages now constrain the high-temperature evolution of the shear zone [*Schärer et al.*, 1990, 1994; *Zhang*, 1995; *Zhang and Schärer*, 1999] and 100 ^{40}Ar/^{39}Ar ages constrain the shear zone cooling history [*Harrison et al.*, 1992, 1996; *Leloup et al.*, 1993; *Chen et al.*, 1993; *Wang et al.*, 1998; *Chen and Li*, 1998; this study]. On Plate 2a these ages (Table 7) are plotted with respect to their location along the strike of the ASRR. Note that because across-strike diachronism is documented in the Ailao Shan range [e.g., *Harrison et al.*, 1992], only samples from <10km from the NE boundary of the range are plotted on Plate 2. As for central DNCV (Figure 19), it is possible to draw time/space temperature domains that fit most data (Plate 2b). Plate 2b shows that the four metamorphic ranges of the ASRR experienced contrasting thermal histories and that the thermochronological data from the entire length of the ASRR have to be taken into account to infer the timing of shear zone evolution.

Using only ^{40}Ar/^{39}Ar data from the DNCV, without petrographic or structural control, *Wang et al.* [1998, 2000] concluded that the ASRR was not active before 27 Ma. As an important part of the left-lateral shear took place at temperatures >500°C, above the highest Ar closure temperature, this conclusion is unfounded. Because the shear zone suffered prograde metamorphism leading to very high temperatures and crustal melting [e.g., *Leloup and Kienast*, 1993; *Leloup et al.*, 1999], clues to constrain the age of onset of left-lateral shear are difficult to find as most geochronometers have probably been reset during peak metamorphism. It has been, however, possible to date the emplacement of granitoids within the shear zone using the U/Pb method. These granitoids may have formed at the time of, or later than, the peak metamorphism and thus give minimum ages for the onset of left-lateral shear. The limited number of dated leucocratic veins in the Ailao Shan range may have initially yielded the impression that synleft-lateral shear granitoid intrusions were restricted to the 22-26 Ma time span [*Schärer et al.*, 1994, 1990]. New data suggest a longer interval for these intrusions with ages of 31.9±0.3 Ma for zircons from an orthogneiss in central Ailao Shan (YS13 [*Zhang and Schärer*, 1999]) and 33.1±0.2 Ma for Ti-U oxydes from a leucocratic layer of XueLong Shan (YS26 [*Zhang and Schärer*, 1999]). However, it cannot be ruled out a priori that some of these ages correspond to a magmatic event, prior to left-lateral shear, products of which would have been smeared out along the ASRR. Potassic magmas dated between 40 and 30 Ma crop out along and on both sides of the ASRR [e.g., *Chung et al.*, 1997; *Zhang and Schärer*, 1999]. The largest of these is the FSP granite, which is dated at 35 Ma (see section 5.4.1). The way in which these magmatic rocks are interpreted has important bearings on the timing of shear along the ASRR. For *Chung et al.* [1997, 1998] these magmas

resulted from lower lithosphere delamination beneath the whole of eastern Tibet. They claim that this magmatism and the associated extension occurred before the initiation of the ASRR, thus postponing the onset of left-lateral shear until after 30 Ma and pinning the maximum left-lateral offset to ≈600 km (Figure 1). There is, however, no clear evidence for any regional extension at that time in eastern Tibet or in Yunnan. These regions were affected by compression at that time [e.g *Lacassin et al.*, 1996]. Alternatively, it has been proposed that the potassic magmas were generated during left-lateral shear along the ASRR belt, either in the lithospheric part of the shear zone [*Schärer et al.*, 1994; *Leloup et al.*, 1995, 1999; *Zhang and Schärer*, 1999], or triggered by an external heat source like a hot spot [*Zhang and Schärer*, 1999]. The fact that potassic magmatism and left-lateral shear were coeval is confirmed by the structural relationships described above that indicate that the largest alkaline body (the FSP granite) was syntectonic (see section 5). This strongly suggests that left-lateral shear was active at ≈35 Ma and that the ≈600 km offset between the FSP and Jianchuan magmatic provinces was acquired since that time and is only a lower bound of the total offset on the ASRR.

Argon thermochronology data only indirectly constrain the age of the end of left-lateral shearing as they mostly document cooling histories, thus possibly denudation, but not strike-slip motion. As mentioned above, the four ranges forming the ASRR, although having their own cooling histories, show two main episodes of rapid cooling (I and II on Plate 2b) separated by a period of slower cooling. The first episode (cooling I) corresponds to cooling from peak to greenschist metamorphic conditions, whereas the second (cooling II) is more recent and corresponds to cooling from greenschist conditions to present-day exposure.

The previously discussed cooling history of the central DNCV range shows that initial rapid cooling from high temperatures (cooling I) began around 28 Ma and ended at ≈23 Ma and ≈150°C (Plate 2). The only suggestion of a younger cooling event (II) in the DNCV is given by one low-temperature K-feldspar age (5.5 Ma, sample YN20K from the northern part of the range, Plate 2) [*Chen and Li*, 1998]. This age should not be overinterpreted, but we note that it corresponds to the well-constrained age of cooling II in the Diancang Shan range [*Leloup et al.*, 1993] 500 km farther north along strike (Plate 2).

In the Ailao Shan range we propose a cooling history that fits 62 of the 66 available data (Plate 2 and Table 7). Only samples Fa5 (^{40}Ar/^{39}Ar, biotite) and YS59 (fission track, zircon) and, to a much lesser extent, Yu94 (^{40}Ar/^{39}Ar, biotite) and Ys58 (fission track, apatite) are incompatible in terms of age and closure temperature with the other samples. Note that the interpretation we chose in Plate 2 implies that some leucocratic melts dated with U/Pb were emplaced during the first cooling phase in already cooled shear zone rocks (between ≈350°C and 450°C). The most striking feature is that all K-feldspars indicate a rapid low-temperature cooling (≥80°/Myr at $T \leq$ 300°C) and that this rapid cooling is diachronous along strike. It follows a linear relationship of age versus distance, as pointed out by *Harrison et al.* [1996]. This diachronicity is compatible with the other ^{40}Ar/^{39}Ar ages (Plate 2). The average cooling rate from temperatures above 450°C to below 150°C are rapid (between 40 and 90°C/Myr) implying that cooling most probably results from tectonic denudation that

Table 7. ASRR Geochronological Data[a]

No.	D, km	d, km	Sample	Mineral	Method	Remark	Age, Ma	Reference
					XLS			
1	965		YS26	Ti-U oxyde	U/Pb	leucocratic layer	33.1±0.2	1
			YS26	apatite	FT		2.7±0.6	2
			Yn101	white mica	Ar/Ar		30.6±0.6	3
		4	Yn96	biotite	Ar/Ar		28.2±0.6	3
					DCS			
3	797	1.4	DC28	K-feldspar	Ar/Ar	LT cooling	4.5	5
		3	YA8	apatite	FT		3.6±1	7
		4	DC16	K-feldspar	Ar/Ar	LT cooling	5	5
		4.3	YS35	xénotime	U/Pb	leucocratic layer	22.4±0.2	4
		4.3	YS35	monazite	U/Pb	leucocratic layer	24.2±0.2	4
		4.3	DC10a	amphibole	Ar/Ar		22.5±2	5
		4.3	Dc10c	biotite	Ar/Ar		7.75±0.7	5
		4.3	DC10c	K-feldspar	Ar/Ar	LT cooling	4.5	5
		4.3	Dc11a	biotite	Ar/Ar		7.6±0.1	5
		10	Yu5	white mica	Ar/Ar		10±0.5	6
4	785		MD1	zircon	U/Pb	leucocratic layer	24.7±0.2	1
		0.8	Yu9	white mica	Ar/Ar		21.6±0.3	6
		0.8	DC9c	white mica	Ar/Ar		21.9±0.7	5
		0.8	DC9c	K-feldspar	Ar/Ar	LT cooling	4.5	5
		5	Dc5	biotite	Ar/Ar		6.4±0.3	5
		5	DC5	K-feldspar	Ar/Ar	LT cooling	4.2±	5
		8.3	Dc2a	white mica	Ar/Ar		15.4±0.8	5
		8.3	Dc2a	biotite	Ar/Ar		9.47±0.5	5
		8.3	DC2a	K-feldspar	Ar/Ar	LT cooling	4	5
					Ailao Shan			
6	684	1	Yn24	amphibole	Ar/Ar		27±1	8
		6	Ya24	biotite	Ar/Ar		24.57±0.4	9
		6	Ya24	K-feldspar	Ar/Ar	LT cooling	17.5±	8
		6.5	Yn27	amphibole	Ar/Ar		29.75±0.3	8
		6.5	Yn27	K-feldspar	Ar/Ar	LT cooling	17.5	8
8	633	1	Yu97	amphibole	Ar/Ar		20.08±0.5	9
	625	1	YS59	zircon	U/Pb	deformed intrusion	26.2±0.6	4
		1	YS59	titanite	U/Pb	deformed intrusion	26.1±0.3	4
		1	YS60	zircon	U/Pb	leucocratic layer	25±1.5	4
		1	YS60	titanite	U/Pb	leucocratic layer	22.4±0.2	4
		1	YN2	K-feldspar	Ar/Ar	LT cooling	18	10
		1	YS59	zircon	FT		25.7±0.9	2
		1	YS59	apatite	FT		11.2±0.7	2
		1	YS60	apatite	FT		9.9±0.6	2
	623	1	Yu93	amphibole	Ar/Ar		20.9±0.8	9
		1	Yu94	biotite	Ar/Ar		17.8±0.9	9
		1	Yu97	K-feldspar	Ar/Ar	LT cooling	17.3±0.2	9
		1	Yu94	K-feldspar	Ar/Ar	LT cooling	17.5	9
9	575	0.2	YX41c	K-feldspar	Ar/Ar	LT cooling	18.2	9
		1	Yx42b	amphibole	Ar/Ar		22.5±0.4	9
		1	YX42b	K-feldspar	Ar/Ar	LT cooling	18.7	9
		2	YS58	titanite	U/Pb	deformed intrusion	26.3±0.3	4
		2	YS58	apatite	FT		13.9±1	2
10	563	1	FA1	K-feldspar	Ar/Ar	LT cooling	19.5	12
	550	1	Fa2-3	amphibole	Ar/Ar		21.3±0.7	12
	550	1	FA2-1	K-feldspar	Ar/Ar	LT cooling	19.5	12
	545	1	Yx16a	K-feldspar	Ar/Ar	LT cooling	19.5±	9
	542	1	YS9	monazite	U/Pb	leucocratic layer	23.1±0.6	11
11	532	0.4	Fa4-1	K-feldspar	Ar/Ar	LT cooling	20.5	12
		1.6	Yu28	amphibole	Ar/Ar		21.7±0.3	9
		2	YS53	monazite	U/Pb	deformed intrusion	25.8±0.2	1
		2.2	YS54	titanite	U/Pb	leucocratic layer	24.1±0.2	4
		2.2	YS54	apatite	FT		10.3±0.5	2
		4.1	YX29a	biotite	Ar/Ar		20.7±0.2	9
		4.1	YX29	K-feldspar	Ar/Ar	LT cooling	20	9
		4.9	YS53	apatite	FT		10.3±0.9	2
		7.3	YX26	K-feldspar	Ar/Ar	LT cooling	20	9
		8.8	Fa5	biotite	Ar/Ar		26.8±0.3	9
		8.8	Fa5	K-feldspar	Ar/Ar	LT cooling	20.5±	12

Table 7. (continued)

No.	Figure 4	D, km	d, km	Sample	Mineral	Method	Remark	Age, Ma	Reference
					Ailao Shan (continued)				
12		495	1	YX12b	amphibole	Ar/Ar		24.2±0.8	9
			1	Yx12b	K-feldspar	Ar/Ar	LT cooling	19.5	9
			2.9	Yu36	K-feldspar	Ar/Ar	LT cooling	20.5	9
			5.3	Yu38	biotite	Ar/Ar		22.04±0.5	9
			5.3	Yu39	K-feldspar	Ar/Ar	LT cooling	21	9
			6.6	YS11	xénotime	U/Pb	leucocratic layer	23.1±0.3	11
			6.6	YS11	titanite	U/Pb	leucocratic layer	22.7±0.3	11
			9.2	Fa7	K-feldspar	Ar/Ar	LT cooling	20.2	12
			9.2	Yu40	biotite	Ar/Ar		22.76±0.5	9
13		485	7.5	YS13	monazite	U/Pb	deformed intrusion	31.9±0.3	1
			7.5	YS13	apatite	FT		11.4±0.8	2
14		400	1	Yu62	biotite	Ar/Ar		22.87±0.2	9
			1	Yu62	K-feldspar	Ar/Ar	LT cooling	22.5	9
			5	Yu59	K-feldspar	Ar/Ar	LT cooling	21	9
			11.5	Yu57	amphibole	Ar/Ar		23.3±0.4	9
			11.5	Yu57	K-feldspar	Ar/Ar	LT cooling	22.2	9
			17	Yu56	amphibole	Ar/Ar		26.7±0.5	9
			17	Yu56	K-feldspar	Ar/Ar	LT cooling	24	9
			19	Yu55	biotite	Ar/Ar		26.23±0.5	9
			22	Fa8	biotite	Ar/Ar		25.8±0.1	9
			22	FA8	white mica	Ar/Ar		25.9±0.1	12
			22	FA8	K-feldspar	Ar/Ar	LT cooling	24	12
15		350	-	YN18	K-feldspar	Ar/Ar	LT cooling	24.5	10
			-	YN19	K-feldspar	Ar/Ar	LT cooling	23.6	10
16		273	7.2	V103	biotite	Ar/Ar		28.13±0.1	3
			7.2	V103	K-feldspar	Ar/Ar	LT cooling	25.1±0.3	9
		263	0	VN105	biotite	Ar/Ar		28.4±1	13
					FSP-SaPa				
17	B	250	17	V33	biotite	Ar/Ar		34.04±0.8	3
			17	V33	K-feldspar	Ar/Ar	LT cooling	27±2	3
			19	V35	phlogopite	Ar/Ar		34.92±0.7	3
		240	18	V100	biotite	Ar/Ar		32.4±0.7	3
			20	V37	biotite	Ar/Ar		33.3±0.7	3
		250	23	YS50	titanite	U/Pb		35±0.3	1
			23	V40	K-feldspar	Ar/Ar	LT cooling	27.6±	3
					DNCV				
16	D	260	?	YN20K	K-feldspar	Ar/Ar	LT cooling	5.5	10
19	D	195	1.7	V12	biotite	Ar/Ar		23.13±0.4	3
			1.7	V12	K-feldspar	Ar/Ar	LT cooling	22.8±0.2	3
			11.3	V18	biotite	Ar/Ar		23.94±0.2	3
			11.3	V20	biotite	Ar/Ar		23.43±0.1	3
20		160	6	19B	amphibole	Ar/Ar		25.8±0.3	14
			6	19B	biotite	Ar/Ar		23.6±0.1	14
			6	19B	K-feldspar	Ar/Ar	LT cooling	23±0.2	14
		159	5	13B	amphibole	Ar/Ar		23.7±0.2	14
			5	13A	biotite	Ar/Ar		22.8±0.1	14
21	E	134	4	V4	biotite	Ar/Ar		24.88±0.2	3
			4	V4	K-feldspar	Ar/Ar	LT cooling	23±0.1	3
		128	6	12A	biotite	Ar/Ar		24.3±0.2	14
			6	12A	K-feldspar	Ar/Ar	LT cooling	23.8±0.2	14
			6	12B	biotite	Ar/Ar		24.4±0.2	14
			6	12D	K-feldspar	Ar/Ar	LT cooling	24.3±0.4	14
22	F	69	7	16B	amphibole	Ar/Ar		26.8±0.4	14
			7	16B	biotite	Ar/Ar		24.8±0.2	14
			7	16C	K-feldspar	Ar/Ar	LT cooling	23.1±0.1	14
		66	7	V1	biotite	Ar/Ar		24.08±0.1	3
			7	V1	K-feldspar	Ar/Ar	LT cooling	22.2±0.6	3
23	G	-77	?	V126	biotite	Ar/Ar		27.5±0.6	3

[a]No., site number on Plate 2; D (km): distance along strike from a reference point near Hanoi; d (km); distance across strike from the NE boundary of the range. On Plate 1 only samples with $d \leq 10$ are plotted. References are 1, *Zhang and Schärer* [1999]; 2, *Bergman et al.* 1997]; 4 *Schärer, et al.* [1994]; 5 *Leloup et al.* [1993]; 6 H. Maluski (personal communication, 1991); 7, S. Bergman (personal communication, 1998); 8, P. H. Leloup (unpublished result, 1998); 9, *Harrison et al.* [1996]; 10, *Chen and Li* [1998]; 11, *Schärer et al.* [1990]; 12, *Harrison et al.* [1992]; 13, *Maluski et al.* [2000]; 14, *Wang et al.* [1998].
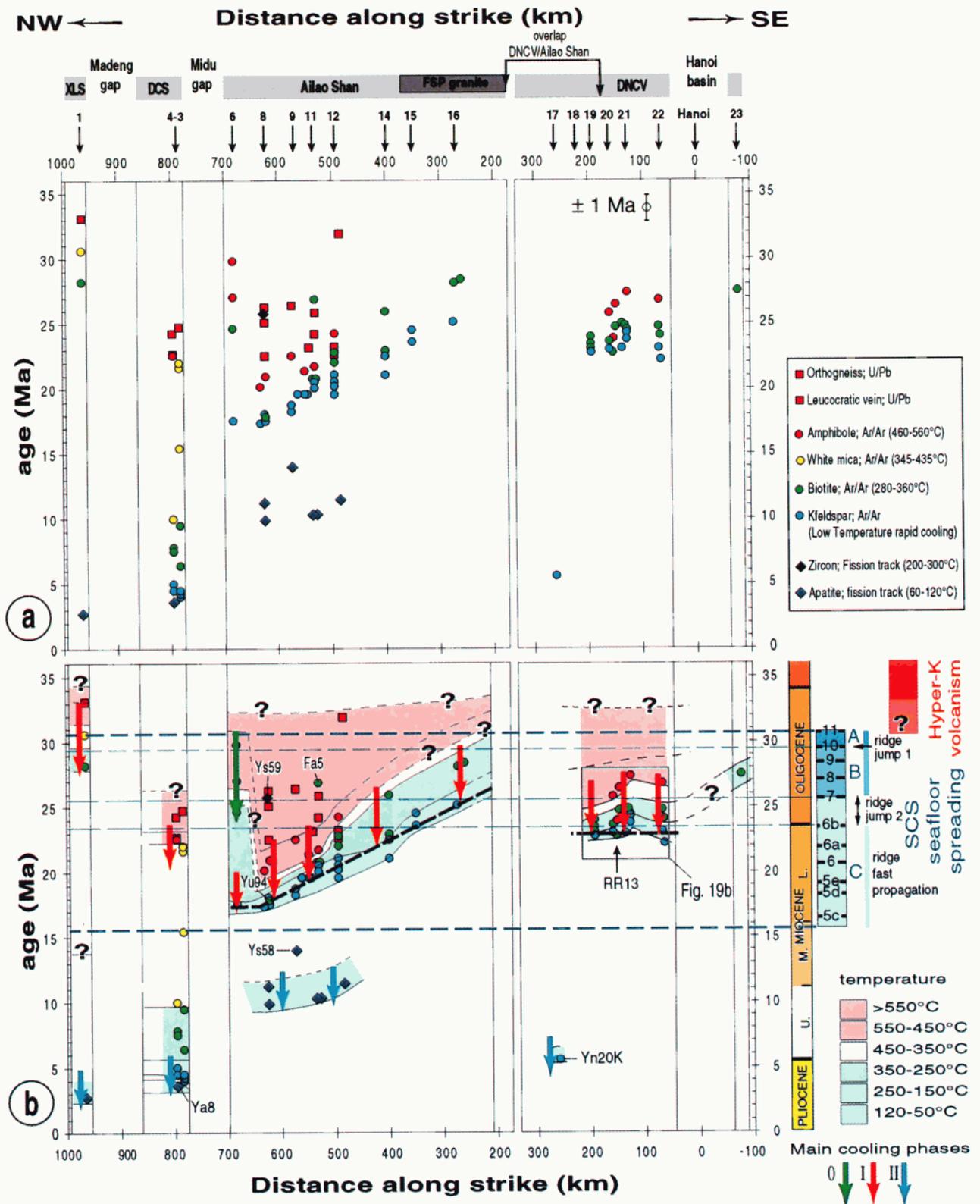
Plate 2. Summary of thermochronological data for entire ASRR. Same representation as for Figure 19. DayNuiConVoi and Ailao Shan ranges overlap near the China/Vietnam border. (a) All data (Table 7). Fission track results from *Bergman et al.* [1997] and S. Bergman (personal communication, 1998), and ^{40}Ar/^{39}Ar results are from Leloup et al. [1993], Chen et al. [1993], *Harrison et al.* [1996], *Wang et al.* [1998], and this study, U-Pb results are from *Schärer et al.* [1990, 1994] and *Zhang and Schärer* [1999]. Uncertainties on most samples are much less than ±1 Ma (Table 7). Because of across-strike diachronous cooling in Ailao Shan, only data coming from <10 km from the range NE border are plotted. (b) Time/temperature domains deduced from Plate 2a. Note the contrasted cooling histories in the four ranges of ASRR. SCS seafloor spreading timing is plotted on the right for comparison.

occurred earlier in the south of the range than in the north. The rate of propagation of this cooling along the range is given by the slope of the linear array defined by K-feldspar results on Plate 2: 48 km/Myr (4.8 cm/yr) between ≈26 and ≈17 Ma. This value is nearly identical to those previously calculated on a smaller database [e.g., *Harrison et al.*, 1996]. Onset of the low-temperature part of cooling I, defined by the K-feldspar, started at ≈26 Ma along the BatXat section (Figure 11d; 16 on Plate 2). The time at which cooling I ended is constrained by the youngest K-feldpar rapid cooling: 17.5 Ma at sites 8 and 6 at the northern extremity of the range. Note that this part of the range also shows an early cooling phase (0 on Plate 2) not seen elsewhere.

Five of the six apatite fission track ages range between ≈10 and 11 Ma (Plate 2), [*Bergman et al.*, 1997]. Track lengths >14μm in all but one sample suggest rapid cooling. The time gap of ≈5 Myr separating the apatite fission track and K-feldspar argon data suggests that it is a distinct cooling event (cooling II).

The DianCang Shan time-temperature history shows rapid cooling at 4.7±0.1Ma (cooling II, Plate 2) [*Leloup et al.*, 1993], confirmed by a 3.6±1 Ma fission track age on sample Ya8 apatites (Table 7, S. Bergman, personal communication, 1998). This cooling has been preceeded by several million years of relatively slow cooling that followed a first rapid cooling phase at high temperatures. This initial phase (cooling I) took place around 22 Ma [*Leloup et al.*, 1993; *Harrison et al.*, 1996].

In the XLS range, as in the other ranges of the ASRR, both the leucocratic layer emplacement and the following cooling probably occurred during left-lateral shear. The 33.1±0.2 Ma U/Pb age of Ti oxides within YS26 thus suggests that left-lateral shear was going on in the XLS around 33 Ma. Cooling from high temperatures (cooling I) occurred earlier than in the

other ranges of the ASRR (Plate 2). Temperatures around 300°C were reached at ≈26 Ma (Figure 3). At that time, the left-lateral ductile deformation in the XLS range [*Leloup et al.*, 1995] probably ended and the main locus of deformation shifted to the numerous fault zones east of the metamorphic range (Figure 2). This indirectly confirms an early age for the onset of left-lateral shear as significant ductile left-lateral deformation had already taken place in the XLS at ≈26 Ma. We have no constraints on the cooling history during the ≈25 Myr following cooling episode I, but a second rapid cooling event (II) is documented at ≈2.7 Ma by the apatite fission track data [*Bergman et al.*, 1997] (Figure 3h).

In the different ranges of the ASRR, the two phases of rapid cooling (I and II) are most probably due to rapid denudation. P-T-t paths (Figure 17) for the DCS, central Ailao Shan and DNCV ranges have been drawn from the combination of cooling histories (Plate 2), P-T paths (Figure 11 of *Leloup and Kienast*, [1993], Figure15 of *Leloup et al.*, [1993], and Plate 1h of this study), and a crude estimate of the amount of denudation induced by the active normal faults bounding these ranges (see *Leloup et al.*, [1993, 1995]). From these P-T-t paths, estimates of the denudation rates during cooling phase I (and left-lateral shearing) vary between 0.4 mm/yr in the DCS to 1.6 and 1.7 mm/yr in the central Ailao Shan and DNCV (Figure 17). In all ranges, this denudation phase started at temperatures for which left-lateral shear is demonstrated.

There are various ways to uplift and erode rocks in a strike-slip shear zone. The fact that cooling occurred at different times throughout the ASRR suggests that several denudation mechanisms may have been active. In the DCS, cooling I (≈22 Ma) most probably resulted from a local event: the activation of a south dipping shear plane cutting the shear zone and denuding the DCS [*Leloup et al.*, 1993]. In the Ailao Shan a linear relationship between the age of cooling I and distances ex-
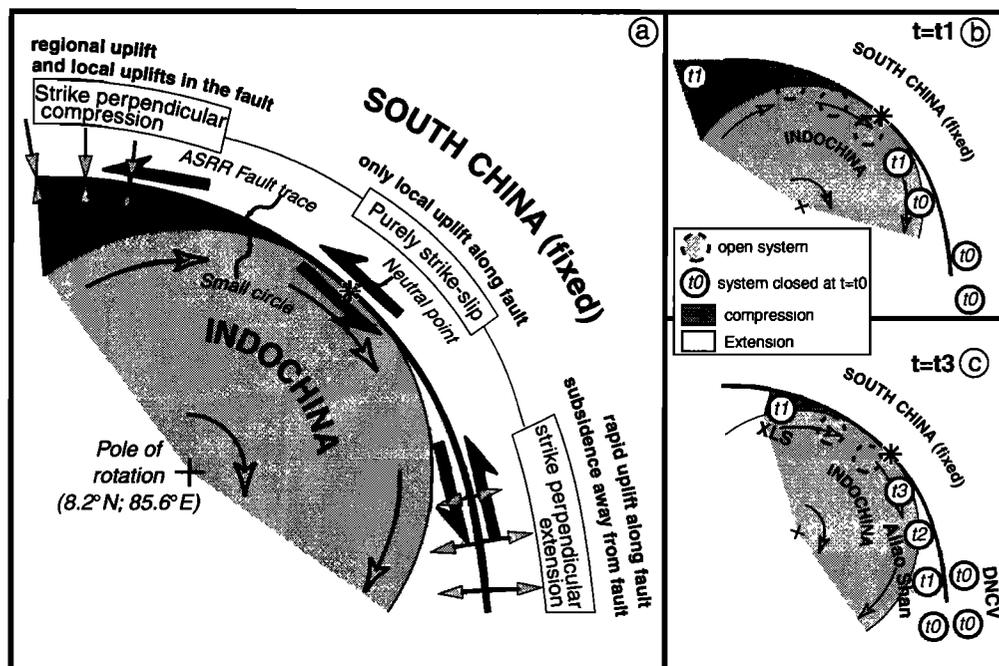

Figure 20. Zipper tectonic model. (a) Theorical location of transpression, pure strike-slip and transtension along a strike-slip fault that does not follow a small circle. (b, c) Schematic evolution of Xue Long Shan (XLS), Ailao Shan, and DayNuiConVoi (DNCV) samples within zipper tectonic system through time.

ists for more than 300 km along strike, suggesting a regional denudation mechanism. A model explaining the apparent along-strike cooling diachronism has been proposed (zipper tectonics [Harrison et al., 1996]). If the ASRR was a transform fault in the strictest sense, it would follow a small circle of the Euler rotation pole between the Indochina and South China Blocks, and the movements would be purely strike-slip. There would be only local denudation along the fault zone in restraining or releasing bends. On the other hand, if the fault does not follow a small circle, transpression and transtension take place along large portions of the fault: in the NW and SE parts respectively, of the left-lateral ASRR fault zone [Briais et al., 1993]. The neutral point that corresponds to the place where the fault zone aligns with a small circle is the only place where motion is purely strike slip (Figure 20). Rocks originally located within the Indochina Block along of the NW portion of the fault zone will thus first deform in a transpressional regime, then in pure strike-slip near the neutral point, before entering the transtensional domain. In this zone, extension induces normal faulting and thus denudation and rapid cooling of the footwall of the fault zone. The apparent rate of progression of cooling along strike would thus correspond to the rate at which rocks located on the Indochina Block pass through the neutral zone and enter the transtensional zone (Figure 20). We infer that at the end of left-lateral motion the neutral point was located between the Ailao Shan and DCS ranges, in the "Midu metamorphic gap" where denudation has been minimal. The parts of the shear zone located farther north would not have been exhumed by transtension but by local mechanisms. Such local mechanisms may also explain the early cooling phase that occurred at the northern extremity of the Ailao Shan (0 on Plate 2), more than 10 Myr earlier than cooling due to zipper tectonics. The northward decrease in width of the Ailao Shan range would reflect the progressive decrease of finite denudation due to the zipper mechanism. If this interpretation is correct, we may estimate the minimum offset, the rate of strike-slip deformation, and the time strike-slip shear ended. If the neutral point was fixed relative to the South China (SC) Block (Indo/SC pole fixed relative to SC block during the whole deformation), the minimum offset would correspond to the length of rocks that passed through the neutral point (≥400 km), and strike-slip rate would equal the apparent migration rate of cooling along strike (4.8 cm/yr). Any motion of the neutral point may alter the strike-slip rate determination. For example, if the neutral point migrated NW, we would overestimate the strike-slip rate. On the other hand, estimating when left-lateral shear ended does not depend on the stability of the neutral point but is the age of the end of cooling I at the final location of the neutral point in the Midu gap. A maximum estimate is thus given by the cooling ages at the northern tip of Ailao Shan: 17 to 18 Ma (Plate 2).

The DNCV rocks, although located southeast of the neutral point, do not show any along-strike cooling diachronism (Figure 19 and Plate 2). We infer that in the DNCV denudation brought to the surface the NE belt corresponding to the edge of the South China Block. These rocks were always located in a transtensive regime. The time of initiation of denudation in the DNCV (cooling phase I, ≈28 Ma) should thus correspond to the onset of the zipper tectonics. Indeed this age is close to that of the oldest cooling phase I documented along the northeastern edge of the Ailao Shan (BatXat section, n°16, Plate 2). This age is also found between the two southward jumps of the

South China Sea spreading ridge at anomaly 10 (29 Ma) and between anomalies 7 and 6b (25.5 and 23.3 Ma) [Briais et al., 1993; Cande and Kent, 1995]. The synchronism of the initiation of zipper tectonics and the ridge jumps suggests that these events are mechanically linked. It is probable that a major propagation of the ASRR fault tip induced the southward ridge jump, after which a stable situation prevailed for ≈10 Myr: zipper tectonics along the ASRR and continuous seafloor spreading in the SCS.

A detailed analysis of the geochronological database on the ASRR thus shows that left-lateral shear was probably active prior to 36 Ma, certainly at 32 Ma, and that it lasted until shortly after 17 Ma. A strike-slip rate of ≈4.8 cm/yr between ≈27 and 17 Ma is derived from the diachronism of cooling ages but may slightly overestimate the true rate.

7.2. Total Displacement Along the ASRR and Its Variation Along Strike

Considering large-scale geological makers (ophiolite belts, Mesozoic basins, Permian basalts, Triassic arc volcanics, Cretaceous granites, and Permian gabbros), Leloup et al. [1995] concluded that 700±200 km was the best estimate for the Tertiary left-lateral offset on the ASRR. Some new estimates confirm this values. The apparent offset of Permian gabbros (≥ 450 km) has been corroborated by that of Permian picritic lavas [Wu, 1993; Chung et al., 1997]. According to Gilder et al. [1996] a major NE-SW Cretaceous discontinuity affecting the South China Block (the Shi-Hang zone) is truncated by the ASRR and cannot be found in the Indochina Block. It probably lies below sea level on the Sunda shelf, implying more than 1000 km of left-lateral offset on the southern part of the ASRR (Figure 1). As noted in section 7.1, the ≈600 km offset of Cenozoic-Potassic magmatic rocks only corresponds to a fraction of the total offset on the ASRR. Given the age of that magmatism (≈35 Ma, see section 7.1) and considering that left-lateral shear stopped at 17 Ma, this offset would correspond to a rate of ≈3.3 cm/yr. In any case, the initial geometries of offset geological units are unknown leading to large uncertainties, and large-scale smearing along the fault zone may cause the total offset to be underestimated.

Paleomagnetism is often used to detect large north-south relative motions between tectonic plates, with a typical precision of a few hundred kilometers, which is usually too low to detect motion on intracontinental strike-slip faults. For the ASRR the motion is large enough to be detected paleomagnetically. Compilations of paleomagnetic data show that since the early Mesozoic, south China can be considered as a rigid block and that Indochina has been displaced southward relatively to this block [e.g., Yang et al., 1995; Sato et al., 1999]. Taken separately, individual studies are often not convincing because they possess large uncertainties (≥7°). However they all indicate a relative southward motion and a clockwise rotation of Indochina relative to south China and hence a left-lateral displacement on the ASRR. This is particularly spectacular for the Cretaceous basins where N-S motion estimates vary between 6° and 12° of latitude for an average of 10±3° at seven sites [Yang et al., 1995; Sato et al., 1999]. These estimates are confirmed by a new study of the Simao basin [Burchfiel et al., 1999]. Calculation of the left-lateral displacement on the ASRR from these data depends on the trend of the transform. For a north-south fault, left-lateral displacement would be equal to the southward relative motion. It would tend to infinity for an E-W fault. Taking the present

trend of the ASRR (140°), a southward relative motion of 10±3° corresponds to 1400±400 km of left-lateral displacement. This may be an underestimation as the ASRR probably trended more easternly at the time of its initiation.

Whatever the correct estimate for the left-lateral offset (≥ 450 km from geological offset and zipper tectonics or ≥ 1000 km from paleomagnetism), such large horizontal movements have to be absorbed at both extremities of the strike-slip zone. The western extremity of the ASRR corresponds to the region in front of the Indian plate indenter. There northward motion of Indian and Tibetan lithosphere continuously fills the gap created by eastward extrusion. The southeastern stretch of the ASRR is more informative. Inland, the ASRR shear zone can be followed toward the southeast as far as the South China Sea (site G, Figure 4). It has been recently proposed that left-lateral movement was absorbed by thickening in Yunnan and in the Anamitic cordillera (Figure 1) [e.g., *Wang and Burchfiel*, 1997]. In that case, the ASRR would have not significantly offset any geological marker east of the Hanoi basin or the eastern margin of the Asian continent. We do not accept this interpretation. First, the abrupt disappearances of NE-SW structures and of the Cretaceous granitic belt of south China against the ASRR are difficult to explain. Second, more than 450 km of NW-SE shortening would have been absorbed southeast of the FSP area where such minimum offset has been documented (Figure 1). In north Vietnam all folds and thrusts are nearly parallel to the ASRR [e.g., *Lacassin et al.*, 1998], (Figure 4), a trend unlikely to absorb NW-SE shortening. Furthermore, it is improbable that this region of modest relief and normal crustal thickness absorbed an amount of shortening comparable to that of the Himalayas (≈ 500km [*Coward and Butler*, 1985; *Ratschbacher et al.*, 1994]). Alternatively, the left-lateral motion could have been absorbed by NE-SW extension north of the ASRR. This is clearly not the case for mainland south China, where Cenozoic extension is negligable. However, it has been proposed that the ASRR continues southeastward and that the opening of the South China Sea (SCS) absorbed a significant part of the left-lateral motion (Figure 1); [e.g., *Tapponnier et al.*, 1986; *Peltzer and Tapponnier*, 1988; *Briais et al.*, 1993].

7.3. Relationship Between Left-Lateral Shear Along the ASRR and Opening of the SCS

A link between SCS seafloor spreading and left-lateral shear along the ASRR shear zone is sustained by kinematic and timing evidence. From the matching of magnetic anomalies, finite and incremental Euler rotation poles describing the relative motion between the southern (Reed Bank) and northern (south China) margins of the SCS have been calculated [*Briais et al.*, 1993]. Assuming that the southern margin of the SCS was rigidly linked with Indochina, these poles imply ≈3.5 cm/yr of left-lateral strike-slip deformation along the ASRR shear zone between ≈32 and ≈16 Ma with transpression in the NW and transtension in the SE. This is in very good agreement with the structural and geochronologic results presented above. Some authors, however, link the SCS opening to the subduction beneath Borneo, which dragged (slab-pull) the southern margin of the SCS south, thus opening a gap that would have to be filled with new oceanic crust [e.g., *Taylor and Hayes*, 1983].

The slab-pull hypothesis requires ≈500 km of subduction beneath Borneo and Palawan between ≈31 and 16 Ma and the same amount of right-lateral motion along the southern part of the western SCS margin between Dangerous Grounds and
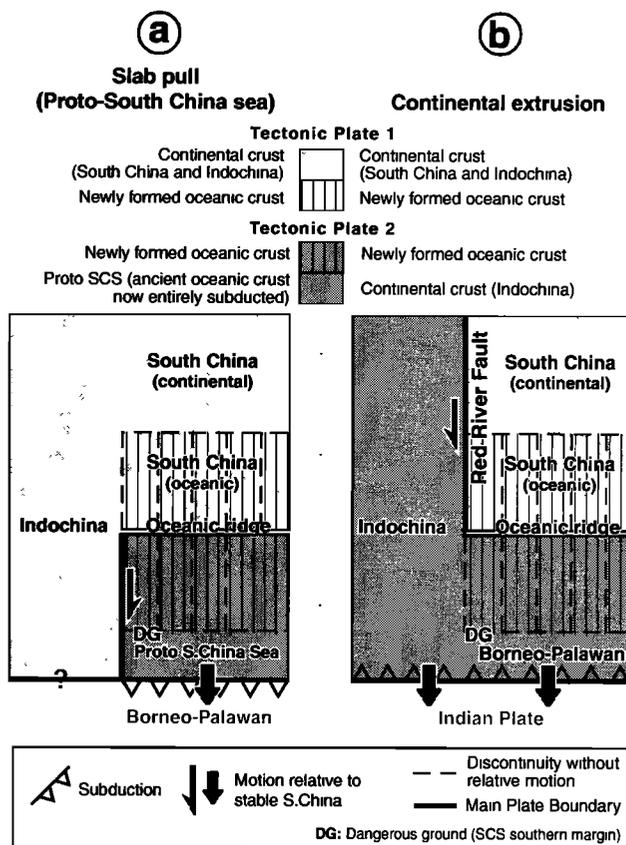

Figure 21. Sketchs of end-member mechanical models proposed for South China Sea (SCS) opening. (a) Slab-pull hypothesis. (b) Pull-apart hypothesis (continental extrusion).

Indochina (Figure 21a). It requires no strike-slip motion along the northern part of this transform. In contrast, extrusion-driven spreading requires ≈500 km of left-lateral displacement along the northern extension of the western SCS margin and no (or minor) relative motion between Dangerous Grounds and Indochina (Figure 21b). Note that subduction beneath Borneo does not contradict the extrusion model, as long as Dangerous Grounds were linked to Indochina. It is thus essential to determine where major strike-slip displacement has taken place between ≈31 and 16 Ma. The fact that seafloor spreading migrated southward [*Briais et al.*, 1993] implies that the tip of the active strike-slip boundary migrated in the same direction. Despite extensive drilling and seismic reflection data acquisition for oil prospecting in the SCS, it is still difficult to map submarine strike-slip faults blanketed by sediments and to determine their timing, sense, and amount of motion. The location, extent, and age of the strike-slip boundary required by the slab-pull hypothesis between the SCS and Indochina have never been addressed in detail. A series of north to NW striking right-lateral faults are mapped affecting the northern margin of Palawan and Borneo. However, very little is known about these faults, and it is dubious that they accommodated large strike-slip motions contemperaneous with SCS seafloor spreading [e.g., *Mat-Zin and Swarbrick*, 1997]. Most of these faults more likely correspond to transform faults within the south SCS margin rather than plate boundary faults between that margin and Indochina. On the other hand, strike-slip motion of several hundred kilometers is plausible along the Vietnamese margin, where strike faults can be followed along the northern part of the YingeHai basin [*Nielsen et al.*, 1999;

Rangin et al., 1995], the QuiNhon ridge [Roques et al., 1997a] and down to 11.5°N [Wirasantosa, 1992] (QuiNhon fault zone, Figure 1). The sense, amount, and timing of movement on these faults is disputed. It, however, appears that (1) prior to 30 Ma, left-lateral motion was restricted north of the Yingehai basin and was mostly absorbed by NW-SE extension in the Beibu basin, in good agreement with the kinematics of the initial phase of seafloor spreading [e.g., Rangin et al., 1995], (2) all strike-slip faults but one are sealed by early to middle Miocene unconformities (≈16 Ma to 12 Ma), [e.g., Rangin et al., 1995; Roques et al., 1997a], (3) the YingeHai basin contains more than 15 to 20 km of Tertiary sediments [Nielsen et al., 1999] and is a pull-apart basin of that age and (4) the geometry of secondary faults on both sides of the QuiNhon fault zone between 14 and 15°N has been interpreted in two ways. From the spoon shape of one NW-SE normal fault affecting the SCS margin and by analogy with undated brittle microstructures observed onshore, Roques et al. [1997a, 1997b] infer a right-lateral shear sense, whereas from the orientation of numerous faults affecting the Vietnamese margin, Wirasantosa [1992] deduces a left-lateral sense of shear. It is thus clear that strike-slip motion took place all along the QuiNhon fault at the time of seafloor spreading in the SCS but the shear sense remains controversial. This is not surprising if one remembers that onshore, the ASRR kinematics were determined only by the mean of microstructural observations [Tapponnier et al., 1990]. Such observations are unfortunately impossible along the QuiNhon ridge, where an inaccessible equivalent of the DayNuiConVoi shear zone may lie, buried below more than 2 km of late Tertiary and Quaternary sedimentary rocks. The simple fact that strike-slip motion occurred along the Vietnamese margin favors the extrusion hypothesis because in the slab-pull hypothesis this margin should only correspond to the limit between unstretched and stretched (or newly created) crust (Figure 21).

The interpretation of the Vietnamese margin as a Mid-Cenozoic dextral strike-slip boundary has led some authors to propose that only the initial stage of rifting until 29 to 26 Ma was induced by the extrusion of Indochina, whereas the subsequent seafloor spreading was due to southward subduction of a proto-SCS [e.g., Marquis et al., 1997]. Other hybrid models where Indochina extrusion and proto-SCS subduction occur either simultaneously or successively have been proposed [e.g., Rangin et al., 1995; Hall, 1997; Jolivet et al., 1999]. As the major tenets of the extrusion model are confirmed, although arguments for the alternating model rest on weak grounds, such models are unnecessary. The quasi-coevality of the end of denudation (and very probably left-lateral shear) along the ASRR, the end of major strike-slip motion in the NW YingeHai basin and along the QhuiNon fault zone, and the end of seafloor spreading suggest that all these events are linked to a common mechanism. As do the fact that the Euler rotation pole determined for the SCS seafloor spreading describes well the motions observed along the ASRR at that time [Briais et al., 1993; Harrison et al., 1996]. We thus propose in section 7.4 a kinematic history of Southeast Asia that incorporates the new constrains on the timing of deformation in northern Vietnam and in which lateral extrusion plays a major role.

7.4. Tertiary Kinematics of Indochina Extrusion

Our structural and geochronological study confirms that the South China Sea opening rotation poles [Briais et al., 1993] describe the motion of Indochina relative to the South China

Block between ≈31 and 16 Ma. By closing the SCS, we can propose a paleogeographic reconstruction of continental SE Asia at ≈31 Ma, significantly after the activation of the ASRR. This approach has already been followed by Briais et al. [1993], Leloup et al. [1995], and Harrison et al. [1996]. Although we fundamentally agree with these reconstructions, we note that they did not consider deformation that occurred since the end of SCS opening. The reconstructions of Figure 22 take these deformations into account. This is the result of a new approach of backward continental deformation [Replumaz, 1999]. Starting from the present situation, continental blocks of the whole India/Asia collision zone are restored along the main faults. The amount and duration of these movements are given by geological constraints (oceanic plate kinematics, timing of major kinematic changes, rate of active faults, offsets on older faults). The originality of this method is that it visualizes the compatibility of motion on contemporaneous faults and unveils the necessity of local rotation, shortening, or stretching. The result is a reconstruction of the whole Asian continent at 5, 16, 32, 40, and 47 Ma [Replumaz, 1999]. We focus on the SE part of the 16 and 32 Ma reconstructions.

At ≈16 Ma (Figure 22a) the extrusion of Indochina and the SCS seafloor spreading ended. The reconstruction takes into account the main deformation that occurred between 0 and ≈16 Ma: (1) northward drift of India and related compressive deformation (formation of the Himalayas and oroclinal bending of the ASRR west of 100°E); (2) the eastward extrusion of Qiantang and South China Blocks that induced the activation of the dextral Red River fault; and (3) 150 km of left-lateral movement along the Xian Shui He fault.

At ≈32 Ma (Figure 22b), prior to the onset of seafloor spreading in the SCS, the ASRR was active for several million years, (probably since before 36 Ma, see discussion in section 7.1). The ASRR trace is difficult to follow west of 95°E within the Tibetan Plateau. However, left-lateral shear has been found near Rutog, close to the western end of the Jurassic Bangong-Nujiang suture zone [Matte et al., 1996]. This suggests that the ASRR fault could have reactivated a section of this discontinuity along one small circle of the pole of rotation for initial SCS seafloor spreading (phase A, Figure 22b). Farther east, the fault clearly deviates from this small circle, suggesting an increase of transtension along strike. Such extension could have triggered the denudation of the ASRR and of nearby structures like the BuKhang dome [Jolivet et al., 1999]; (Figure 22b). Up to 300 km of crustal extension took place across the northern margin of the SCS prior to seafloor spreading [Hayes et al., 1995; Nissen et al., 1995]. Part of this extension is attributed to Cretaceous-Eocene back arc extension, but most of it was probably related to the reactivation of these normal faults in the horsetail termination of the ASRR. Left-lateral movement on the ASRR prior to 31 Ma can thus be estimated to ≥ 200 km.

In its early stage of development the ASRR showed striking similarities with the present-day North Anatolian fault (NAF). To allow direct comparison, Figure 22c is a mirror image of the NAF. Since ≈10 Ma, the right-lateral NAF allowed the lateral escape of the Anatolia Block consecutive to the collision of Arabia and Eurasia [e.g., Armijo et al., 1999]. The present rate on the fault is of the order of 2 cm/yr, and the total offset is evaluated at ≈90 km. GPS measurements show that Anatolia is essentially behaving as a rigid block, for which an Euler pole of rotation with respect to Eurasia can be calculated [Reilinger et al., 1997]. At large scale the branches of the

NAF follow small circles of that pole. After 1000 km of single trace the fault splits in two main branches separated by the large Sea of Marmara pull-apart basin. This basin is probably a good analogue to what was the YingeHai basin at ≈35 Ma. At the western termination of the NAF the grabens of the Aegean domain are reactivated to form a horsetail structure (North Aegean trough, Gulf of Corinth [*Armijo et al.*, 1996]; see Figure 22c). The way Aegean normal faults are reactivated at the termination of the strike-slip fault is quite similar to what happened at the SCS margins at ≈35 Ma. Such normal fault reactivation can explain fault geometries that give contradictory shear senses on both sides of the QuiNhon fault zone (right-lateral for *Roques et al.* [1997a, 1997b] and left-lateral for *Wirasantosa* [1992], see section 7.3). Faults affecting the SCS margin are reactivated and their orientation cannot be used to infer the strike-slip sense, whereas faults affecting the Vietnamese margin are new and indicate a left-lateral shear sense. The NAF propagated through the Sea of Marmara at ≈5 Ma, implying a fault propagation rate one order of magnitude higher than the strike-slip rate [*Armijo et al.*, 1999]. In the case of the ASRR, a fault propagation rate of the order of 30 cm/yr would correspond to fault propagation time of the order of 10 Myr from the Himalaya western syntaxis to Vietnam.

After ≈31 Ma the tip of the ASRR propagated southward and diffuse extension at its termination evolved into seafloor spreading in the SCS (phase A). Seafloor spreading jumped twice toward the south (phases B and C). These southward ridge jumps, and the corresponding minor plate kinematics reorganizations, are probably linked to southward propagation of the strike-slip fault tip along the QuiNhon fault zone. The second jump occurred between magnetic anomalies 7 and 6b (≈25.5 and 23.3 Ma). After that jump, seafloor spreading continued along the same ridge until ≈16 Ma. Final localization of spreading could correspond to the stabilization of fault geometry and of zipper tectonics. We note that the QuiNhon zone has always been nearly parallel to a small circle and was thus favorably oriented to absorb large strike-slip motions (Figures 22a and 22b). The deep Tertiary YingeHai basin formed in a releasing bend between two small circles (Figure 22a). It thus seems that continental left-lateral faulting and extension in the SCS marginal basin are mechanically coupled, with each propagation of the strike-slip fault tip inducing a reorganization of the extensional structures.

7.5. Conclusions

We confirm that the ASRR has absorbed at least 500 km and probably more than 700 km of left-lateral extrusion of Indochina relative to south China in the Oligo-Miocene. The

ASRR was a left-lateral strike-slip lithospheric discontinuity prior to 32 Ma (probably even prior to 36 Ma) until ≈16 Ma. Motion of Indochina relative to south China occurred at ≈5cm/yr between ≈28 and 17 Ma along the central part of the ASRR (Ailao Shan range). This controlled the formation of a new marginal basin: the South China Sea.

The only tectonic model that satisfactorily predicts deformation along the ASRR is the two stage extrusion model proposed by *Tapponnier et al.*, [1986] on the basis of plasticine experiments. Other models either omit the existence of the ASRR or fail to explain the late Miocene reversal of shear along it. The extrusion model is oversimplified, in that the Indochina continental block was not perfectly rigid. The Three Pagodas and Wang Chao strike-slip faults sliced the block in early stages of eastward extrusion [*Lacassin et al.*, 1997] (Figure 22b) and some deformation affected the core of the block during eastward extrusion of Indochina. The largest of these deformations are, however, an order of magnitude smaller than that observed along the ASRR. Between ≈36 and ≈16 Ma, Indochina can be considered as a large coherent block where internal deformations were minimal with respect to deformation along its boundaries. A simple explanation compatible with what we know from the lithospheric strength profile is that deformation is localized in the upper mantle and is more diffuse in the lower crust. In that case, the plasticine experiments would be an image of what happens in the upper mantle.

References

Allen, C.R., A.R. Gillespie, Y. Han, K.E. Sieh, B. Zhang, and C. Zhu, Red River and associated faults, Yunnan province, China: quaternary geology, slip rates, and seismic hazard, *Geol. Soc. Am. Bull.*, *95*, 686-700, 1984.

Armijo, R., B. Meyer, G.C.P. King, A. Rigo, and D. Papanastassiou, Quaternary evolution of the Corinth rift and its implications for the Late Cenozoic evolution of the Aegean, *Geophys. J. Int.*, *126* (1), 11-53, 1996.

Armijo, R., B. Meyer, A. Hubert, and A. Barka, Westward propagation of the North Anatolian fault into the northern Aegean: timing and kinematics, *Geology*, *27* (3), 267-270, 1999.

Bergman, S.C., P.H. Leloup, P. Tapponnier, U. Schärer, and P. O'Sullivan, Apatite fission track thermal history of the Ailao Shan-

Figure 22. Paleogeographic reconstructions of SE Asia. (a) Approximately 16 Ma, prior to the end of SCS seafloor spreading. (b) Approximately 32 Ma, prior to onset of SCS seafloor spreading. Figures 22a and 22b are from slightly modified backward reconstrutions of *Replumaz* [1999]. Rotation poles of Indochina with respect to south China and corresponding small circles (thin lines) from *Briais et al.* [1993]. Pole A is initial seafloor spreading, anomalies 11 and 10 (84.9°E, 10.9°N). Pole C is third stage of seafloor spreading, anomalies 6b to 5c (87.07°E, 6.69°N). Faults active around considered ages are represented. BKD, BuKhang dome; YB, YingeHai basin; MB, Mergui basin; DNCV, DayNuiConVoi range; DCS, DianCang Shan range. Stars correspond to Jianchuan and FanSiPan areas (see Figure 1). (c) Mirror image of present-day extrusion of Anatolia. Modified from *Armijo et al.* [1999]. Thin lines are small circles of Euler pole of rotation of Anatolia with respect to Eurasia given by GPS measurements [*Reilinger et al.*, 1997]. Note the two stages of extension: Aegean diffuse extension (1, light shading) preceding localized extension in pull aparts induced by right-lateral shear along the North Anatolian fault (2, dark shading). NAF, North Anatolian fault; SM, Sea of Marmara; NAT, North Anatolian trough; CR, Corinth rift; EAF, East Anatolian fault; DSF, Dead Sea fault.

Red River shear zone, China, paper presented at meeting, Eur. Union of Geosci., Strasbourg, France, March 23-27 1997.

Berthé, D., P. Choukroune, and D. Gapais, Orientations préférentielles du quartz et orthogneissification progressive en régime cisaillant: L'exemple du cisaillement sud-armoricain, *Bull. Minéral.*, *102*, 265-272, 1979.

Briais, A., P. Patriat, and P. Tapponnier, Updated interpretation of magnetic anomalies and seafloor spreading stages in the South China Sea, implications for the Tertiary tectonics of SE Asia, *J. Geophys. Res.*, *98*, 6299-6328, 1993.

Burchfiel, B.C., J.W. Geissman, E. Wang, C. Liangzhong, and Y.J. Yin, Cenozoic tectonic rotations in Northern Indochina and implications for Middle Cenozoic extrusion of crust South of the Ailao Shan shear zone, *Eos Trans. AGU*, *80*(46), Fall Meet. Suppl., F1044, 1999.

Bureau of Geology and Mineral Resources of Yunnan, Geological map of Yunnan, scale 1:1,000,000, Kunming, 1983.

Bureau of Geology and Mineral Resources of Yunnan,, Geological map of Yunnan, scale 1:200,000, sheet G-47-X (Weixi), Kunming, 1984a.

Bureau of Geology and Mineral Resources of Yunnan, Metamorphic map of Yunnan province, scale 1:2,000;000, Geol. Publ. House, Beijing, 1984b.

Cande, S.C., and D.V. Kent, Revised calibration of the geomagnetic polarity timescale for the Late Cretaceous and Cenozoic, *J. Geophys. Res.*, *100*, 6093-6095, 1995.

Chen, W., and Q. Li, New evidences of tectonic uplift and transform of movement style along the Ailao Shan-Red River fault zone, paper presented at International Geological Congress, Beijing, China,1998.

Chen, W., P.H. Leloup, and M. Harrison, ^{40}Ar/^{39}Ar results from the Ailao Shan and the Diancang Shan, report, Univ. of Calif., Los Angeles, 1993.

Chung, S.-L., T.-Y. Lee, C.-H. Lo, P.-L. Wang, C.-Y. Chen, N. Trong Yem, T. Trong Hoa, and W. Genyao, Intraplate extension prior to continental extrusion along the Ailao Shan-Red River shear zone, *Geology*, *25*, 311-314, 1997.

Chung, S.-L., C.-H. Lo, T.-Y. Lee, Y. Zhang, Y. Xie, X. Li, K.-L. Wang, and P.-L. Wang, Diachronous uplift of the tibetan plateau starting 40 Myr ago, *Nature*, *394*, 769-773, 1998.

Cobbold, P., and P. Davy, Indentation tectonics in nature and experiment, 2, Central Asia, *Bull. Inst. Uppsala*, *14*, 143-162, 1988.

Coward, M.P., and R.W.H. Butler, Thrust tectonics and the deep structure of the Pakistan Himalaya, *Geology*, *13*, 417-420, 1985.

Deprat, J., Les charriages de la région de la Rivière-Noire sur les feuilles de Thanh-ba et de Van-yên, *Mém. Serv. Geol. Indochine*, *2*, 47-65, 1914.

Dewey, J.F., S. Cande, and W.C.I. Pitman, Tectonic evolution of the India/Eurasia collision zone, *Eclogae Geol. Helv.*, *82*, 717-734, 1989.

Dodson, M.H., Cooling temperature in cooling geochronological and petrological systems, *Contrib. Mineral. Petrol.*, *40*, 259-274, 1973.

Duong, C.C., and K. Feigl, Geodectic measurement of horizontal strain across the Red River fault near Thac Bà, Vietnam., *J. Geod.*, *73*, 298-310, 1998.

England, P., and G. Houseman, Finite strain calculations of continental deformation, 2, Comparison with the India-Asia collision zone, *J. Geophys. Res.*, *91*, 3664-3676, 1986.

Foster, D.A., T.M. Harrison, P. Copeland, and M.T. Heizler, Effects of excess argon within large diffusion domains on K-feldspar age spectra, *Geochim. Cosmochim. Acta*, *54*, 1699-1708, 1990.

Ganguly, J., and S. Saxena, Mixing properties of aluminosilicate garnets: Constraints from natural and experimental data, and applications to geothermo-barometry, *Am. Mineral.*, *69*, 88-97, 1984.

General Department of Mines and Geology of the Socialist Republic of Vietnam, Geological map of Kampuchea, Laos and Vietnam, scale 1:1,000,000, Hanoi, 1988.

General Geological Department of the Democratic Republic of Vietnam, Geological map of Vietnam (the north part), scale 1:1,000,000, General Geological Department of the Democratic Republic of Vietnam, Hanoi, 1973.

General Geological Directorate of Vietnam, Geological map of the socialist republic of Vietnam, LaoCai-KimBinh sheet, scale 1:200,000, Hanoi, 1978.

Geological Bureau of Yunnan Province, Geological map of Yunnan province, scale 1:500,000, Kunming, China, 1979.

Gilder, S.A., J. Gill, R.S. Coe, Zhao X., Liu Z., Wang G., Yuan K., Liu W., Kuang G., and Wu H., Isotopic and paleomagnetic constraints on the Mesozoic tectonic evolution of south China, *J. Geophys. Res.*, *101*, 16,137-16,154, 1996.

Giletti, B.J., Studies in diffusion, I, Argon in phlogopite mica, in *Geochemical Transport and Kinetics*, edited by A.W. Hofmann et al., pp. 107-115, Carnegie Inst. of Washington, Washington, D. C., 1974.

Hall, R., Cenozoic plate tectonic reconstructions of SE Asia, in *Petroleum Geology of Southeast Asia*, edited by A.J. Fraser, S.J. Matthews, and R. W. Murphy, *Geol. Soc. Spec. Publ.*, *126*, 11-23,1997.

Hames, W.E., and S.A. Bowring, An empirical evaluation of the argon diffusion geometry in muscovite, *Earth Planet. Sci. Lett.*, *124*, 161-167, 1994.

Hanmer, S., and C. Passchier, Shear-sense indicators: A review, 72 pp., Geol. Surv. of Can., Ottawa, 1991.

Harrison T.M., Diffusion of ^{40}Ar in hornblende, *Contrib. Mineral. Petrol.*, *78*, 324-331, 1981.

Harrison, T.M., I. Duncan, and I. McDougall, Diffusion of ^{40}Ar in biotite: temperature, pressure and compositional effects, *Geochim. Cosmochim. acta*, *49*, 2461-2468, 1985.

Harrison, T.M., M.T. Heizler, and O.M. Lovera, ^{40}Ar/^{39}Ar results for alkali feldspar containing diffusion domains with differing activation energy, *Geochim. Cosmochim. Acta*, *55*, 1435-1448, 1991.

Harrison, T.M., Chen W., P.H. Leloup, F.J. Ryerson, and P. Tapponnier, An early Miocene transition in deformation regime within the Red River fault zone, Yunnan, and its significance for Indo-Asian tectonics, *J. Geophys. Res.*, *97*, 7159-7182, 1992.

Harrison, T.M., M.T. Heizler, O.M. Lovera, Chen W., and M. Grove, A chlorine disinfectant for excess argon released from K-feldspar during step heating, *Earth Planet. Sci. Lett.*, *123*, 95-104, 1994.

Harrison, T.M., P.H. Leloup, F.J. Ryerson, P. Tapponnier, R. Lacassin, and W. Chen, Diachronous initiation of transtension along the Ailao Shan-Red River Shear zone, Yunnan and Vietnam, in *The Tectonic Evolution of Asia*, edited by A. Yin and T.M. Harrison, pp. 208-226, Cambridge Univ. Press, New York, 1996.

Hayes, D.E., S.S. Nissen, P. Buhl, and J. Diebold, Through-going crustal faults along the northern margin of the South China Sea and their role in crustal extension, *J. Geophys. Res.*, *100*, 22,435-22,446, 1995.

Hodges, K.V., and F.S. Spear, Geothermometry, geobarometry and the Al$_2$SiO$_5$ triple point at Mt. Moosilauke, New Hampshire, *Am. Mineral.*, *67*, 1118-1134, 1982.

Holland, T.J.B., and R. Powell, An enlarged and updated internally consistent thermodynamic dataset with uncertainties and correlations: the System K$_2$O-Na$_2$O-CaO-MgO-MnO-FeO-Fe$_2$O$_3$-Al$_2$O$_3$-TiO$_2$-SiO$_2$-C-H$_2$-O$_2$, *J. Metamorph. Geol.*, *8*, 89-124, 1990.

Houseman, G., and P. England, Crustal thickening versus lateral expulsion in the Indian-Asian continental collision, *J. Geophys. Res.*, *98*, 12,233-12,249, 1993.

Izokh, E.P., D.H. Le, and V.T. Nguyen, New information on magmatic activity in North Vietnam, *Doklady Akad. Nauk SSSR*, *155*, 96-98, 1964.

Jolivet, L., H. Maluski, O. Beyssac, B. Goffé, C. Lepvrier, T.T. Phan, and V.V. Nguyen, Oligocene-Miocene Bu Khang extensional gneiss dome in Vietnam: geodynamic implications, *Geology*, *27*, 67-70, 1999.

Kirschner, L., M.A. Cosca, H. Masson, and J.C. Hunziker, Staircase ^{40}Ar/^{39}Ar spectra of fine-grained white mica: timing and duration of deformation and empirical constraints on argon diffusion, *Geology*, *24* (8), 747-750, 1996.

Lacassin, R., Large-scale foliation boudinage in gneisses, *J. Struct. Geol.*, *10*, 643-647, 1988.

Lacassin, R., P.H. Leloup, and P. Tapponnier, Bounds on strain in large Tertiary shear zones of SE Asia from boudinage restoration, *J. Struct. Geol.*, *15*, 677-692, 1993.

Lacassin, R., U. Schärer, P.H. Leloup, N. Arnaud, P. Tapponnier, Liu X., and Zhang L., Tertiary deformation and metamorphism SE of Tibet: The folded tiger-leap décollement of NW Yunnan (China), *Tectonics*, *15*, 605-622, 1996.

Lacassin, R., H. Maluski, P.H. Leloup, P. Tapponnier, C. Hinthong, K. Siribhakdi, S. Chuaviroj, and A. Charoenravat, Tertiary diachronic extrusion and deformation of western Indochina: structural and ^{40}Ar/^{39}Ar evidence from NW Thailand, *J. Geophys. Res.*, *102*, 10,013-10,037, 1997.

Lacassin, R., P.H. Leloup, T. Phan Trong, and P. Tapponnier, Unconformity of red sandstones in north Vietnam: Field evidence for Indosinian orogeny in northern Indochina?, *Terra Nova*, *10*, 106-111, 1998.

Lanphere, M.A., and H. Baadsgaard, The fish canyon tuff: A standard for geochronology, *Eos Trans. AGU*, *78*(17), Spring Meet. Suppl., S326, 1997.

Le Breton, N., and A.B. Thompson, Fluid-absent (dehydration) melting

of biotite in metapelites in the early stages of crustal anatexis, *Contrib. Mineral. Petrol.*, *99*, 226-237, 1988.

Lee, T.Y., and L.A. Lawver, Cenozoic plate reconstruction of Southeast Asia, *Tectonophysics*, *251*, 85-138, 1995.

Leloup, P.H., and J.R. Kienast, High Temperature metamorphism in a major Tertiary ductile continental strike-slip shear zone: The Ailao Shan-Red River (P.R.C.), *Earth Planet. Sci. Lett.*, *118*, 213-234, 1993.

Leloup, P.H., T.M. Harrison, F.J. Ryerson, Chen W., Li Q., P. Tapponnier, and R. Lacassin, Structural, petrological and thermal evolution of a Tertiary ductile strike-slip shear zone, Diancang Shan, Yunnan, *J. Geophys. Res.*, *98*, 6715-6743, 1993.

Leloup, P.H., R. Lacassin, P. Tapponnier, U. Schärer, Zhong D., Liu X., Zhang L., Ji S., and T. Phan Trong, The Ailao Shan-Red River shear zone (Yunnan, China), Tertiary transform boundary of Indochina, *Tectonophysics*, *251*, 3-84, 1995.

Leloup, P.H., Y. Ricard, J. Battaglia, and R. Lacassin, Shear heating in continental strike-slip shear zones: Numerical modeling and case studies, *Geophys. J. Int.*, *136*, 19-40, 1999.

Lovera, O.M., F.M. Richter, and T.M. Harrison, The $^{40}Ar/^{39}Ar$ thermochronology for slowly cooled samples having a distribution of diffusion domain sizes, *J. Geophys. Res.*, *94*, 17,917-17,935, 1989.

Lovera, O.M., F.M. Richter, and T.M. Harrison, Diffusion domains determined by ^{39}Ar released during step heating, *J. Geophys. Res.*, *96*, 2057-2069, 1991.

Lovera, O.M., M. Grove, T.M. Harrison, and K.I. Mahon, Systematic analysis of K-feldspar $^{40}Ar/^{39}Ar$ step heating results, I, Significance of activation energy determination, *Geochim. Cosmochim. Acta*, *61*, 3171-3192, 1997.

Maluski, H., C. Lepvrier, L. Jolivet, V. Carter, V. Roques, V. Beyssac, T.T. Ta, D.T. Nguyen, and D. Avigad, Ar-Ar and fission-track ages in the Song Chay massif, indosinian and Cenozoic tectonics in northern Vietnam, *J. Asian Earth Sci.*, in press, 2000.

Marquis, G., D. Roques, P. Huchon, O. Coulon, N. Chamot-Rooke, C. Rangin, and X. Le Pichon, Amount and timing of extension along the continental margin off central Vietnam, *Bull. Soc. Geol. Fr.*, *168*, 707-716, 1997.

Mat-Zin, I.C., and R.E. Swarbrick, The tectonic evolution and associated sedimentation history of Sarawak Basin, eastern Malaysia: A guide for future hydrocarbon exploration, in *Petroleum Geology of Southeast Asia*, edited by A.J. Fraser, S.J. Matthews, and R. W. Murphy, *Geol. Soc. Spec. Publ.*, *126*, 237-245, 1997.

Matte, P., P. Tapponnier, N. Arnaud, L. Bourjot, J.P. Avouac, P. Vidal, L. Qing, P. Yusheng, and W. Yi, Tectonics of Western Tibet, between the Tarim and the Indus, *Earth Planet. Sci. Lett.*, *132*, 311-330, 1996.

Nam, T.N., P-T-t paths and post metamorphic exhumation of the Day Nui Con Voi shear zone in Vietnam, *Tectonophysics*, *290*, 299-318, 1998b.

Nam, T.N., Thermotectonic events from early Proterozoic to Miocene in the Indochina craton: Implication of K-Ar ages in Vietnam, *J. Asian Earth Sci.*, *16*, 475-484, 1998a.

Nielsen, L.H., A. Mathiesen, T. Bidstrup, O.V. Vejbaek, P.T. Dien, and P.V. Tiem, Modelling the hydrocarbon generation in the Cenozoic Song Hong basin, Vietnam: A highly prospective basin, *J. Asian Earth Sci.*, *17*, 269-294, 1999.

Nissen, S.S., D.E. Hayes, Yao B., Zeng W., Chen. Y., and Nu X., Gravity, heat flow, and seismic constraints on the process of crustal extension: Northern margin of the South China Sea, *J. Geophys. Res.*, *100*, 22,447-22,483, 1995.

Passchier, C.W., and C. Simpson, Porphyroclast systems as kinematic indicators, *J. Struct. Geol.*, *8*, 831-843, 1986.

Passchier, C.W., and R.A.J. Trouw, *Micro-tectonics*, 289 pp., Springer-Verlag, New York, 1996.

Peltzer, G., and P. Tapponnier, Formation and evolution of strike-slip faults, rifts, and basins during the India-Asia collision: An experimental approach, *J. Geophys. Res.*, *93*, 15,085-15,117, 1988.

Pouchou, J.L., and F. Pichoir, Quantitative analysis of homogenous or stratified microvolumes applying the model PAP, in *Electon Probe Quantitation*, edited by K. F. J. Einrich and Dale E. Newbury, pp. 31-75, Plenum Press, New York and London, 1991.

Powell, R., and T. Holland, Calculated mineral equilibria in the pelite system, KFMASH $(K_2O-FeO-Al_2O_3-SiO_2-H_2O)$, *Am. Mineral.*, *75*, 367-380, 1990.

Rangin, C., M. Klein, D. Roques, X. Le Pichon, and L.V. Trong, The Red River fault system in the Tonkin Gulf, Vietnam, *Tectonophysics*, *243*, 209-222, 1995.

Ratschbacher, L., W. Frisch, and G. Liu, Distributed deformation in the

southern and western Tibet during and after the India-Asia collision, *J. Geophys. Res.*, *99*, 19,917-19,945, 1994.

Reilinger, R.E., S.C. McClusky, M.B. Oral, R.W. King, M.N. Toksoz, A.A. Barka, I. Kinik, O. Lenk, and I. Sanli, Global Positioning System measurements of present-day crustal movements in the Arabia-Africa-Eurasia plate collision zone, *J. Geophys. Res.*, *102*, 9983-9999, 1997.

Replumaz A., Reconstruction de la zone de collision Inde-Asie: Etude centrée sur l'Indochine, Ph. D. thesis, 229 pp., Univ. Paris 7, Paris, 1999.

Replumaz, A., R. Lacassin, P. Tapponnier, and P.H. Leloup, Large river offsets and Plio-Quaternary dextral slip rate on the Red River fault (Yunnan, China), *J. Geophys. Res.*, in press, 2000.

Roddick, J.C., R.A. Cliff, and D.C. Rex, The evolution of excess argon in alpine biotites, a $^{40}Ar/^{39}Ar$ analysis, *Earth Planet. Sci. Lett.*, *48*, 185-208, 1980.

Roques, D., S.J. Matthews, and C. Rangin, Constrains on strike-slip motion from seismic and gravity data along the Vietnam margin offshore Da Nang: Implications for hydrocarbon prospectivity and opening of the East Vietnam Sea, in *Petroleum Geology of Southeast Asia*, edited by A.J. Fraser, S.J. Matthews, and R. W. Murphy, *Geol. Soc. Spec. Publ.*, *126*, 341-353,1997a.

Roques, D., C. Rangin, and P. Huchon, Geometry and sense of motion along the Vietnam continental margin: Onshore/offshore Da Nang area, *Bull. Soc. Geol. Fr.*, *168*, 413-422, 1997b.

Sato, K., Y. Liu, Z. Zhu, Z. Yang, and Y.-I. Otofuji, Paleomagnetic study of middle Cretaceous rocks from Yunlong, western Yunnan, China: Evidence of southward displacement of Indochina, *Earth Planet. Sci. Lett.*, *165*, 1-15, 1999.

Schärer, U., P. Tapponnier, R. Lacassin, P.H. Leloup, Zhong D., and Ji S., Intraplate tectonics in Asia: A precise age for large-scale Miocene movement along the Ailao Shan-Red River shear zone, China, *Earth Planet. Sci. Lett.*, *97*, 65-77, 1990.

Schärer, U., Zhang. L.S., and P. Tapponnier, Duration of strike-slip movements in large shear zones: The Red River belt, China., *Earth Planet. Sci. Lett.*, *126*, 379-397, 1994.

Spear, F.S., and J.T. Cheney, A petrogenetic grid for pelitic schists in the system $SiO_2-Al_2O_3-FeO-MgO-K_2O-H_2O$, *Contrib. Mineral. Petrol.*, *101*, 149-164, 1989.

Tapponnier, P., and P. Molnar, Active faulting and tectonics of China, *J. Geophys. Res.*, *82*, 2905-2930, 1977.

Tapponnier, P., G. Peltzer, R. Armijo, A.-Y. Le Dain, and P. Cobbold, Propagating extrusion tectonics in Asia: New insights from simple experiments with plasticine, *Geology*, *10*, 611-616, 1982.

Tapponnier, P., G. Peltzer, and R. Armijo, On the mechanics of the collision between India and Asia, in *Collision Tectonics*, edited by M.P. Coward and A.C. Ries, *Geol. Soc. Spec. Publ. 19*, 115-157, 1986.

Tapponnier, P., R. Lacassin, P.H. Leloup, U. Schärer, Zhong D., Liu X., Ji S., Zhang L., and Zhong J., The Ailao Shan/Red River metamorphic belt: Tertiary left-lateral shear between Indochina and south China, *Nature. 343*, 431-437, 1990.

Taylor, B., and D.E. Hayes, Origin and history of the south China Basin, in *The Tectonic and Geologic Evolution of Southeast Asian Seas and Islands, Part 2*, *Geophys. Monogr. Ser.*, vol 27, edited by D.E. Hayes, pp. 23-56, AGU, Washington, D. C., 1983.

Thompson, A.B., Dehydration melting of pelitic rocks and the generation of H_2O-undersaturated granitic liquids, *Am. J. Sci.*, *282*, 1567-1595, 1982.

Tran V. T., et al., Explanation to the 1:1,000,000 geological map of Vietnam (The north part), Socialist Republic of Vietnam, Gen. Dep. of Geol., Res. Inst. of Geol. and Miner. Resour., Hanoi, 1979.

Wang, E., and B.C. Burchfiel, Interpretation of Cenozoic tectonics in the right-lateral accomodation zone between the Ailao Shan shear zone and the eastern Himalayan syntaxis, *Int. Geol. Rev.*, *39*, 191-219, 1997.

Wang, P.-L., C.-H. Lo, T.-Y. Lee, S.-L. Chung, C.-Y. Lan, and N. Trong Yem, Thermochronological evidence for the movement of the Ailao Shan-Red River shear zone: A perspective from Vietnam, *Geology*, *26*, 887-890, 1998.

Wang, P.-L., C.-H. Lo, S.-L. Chung, T.-Y. Lee, C.-Y. Lan, and T.V. Thang, Onset timing of left-lateral movement along the Ailao Shan-Red River shear zone: $^{40}Ar/^{39}Ar$ dating constraint from the Nam Dinh area, northeastern Vietnam, *J. Asian Earth Sci.*, *18*, 281-292, 2000.

Wirasantosa, S., Cenozoic seismic stratigraphy and structure of the continental margin offshore Vietnam, South China Sea, Ph. D. thesis, Tex. A&M Univ., College Station, 1992.

Wu, G.Y., Permian basalts in Lijiang and Jinping, western Yunnan: A

comparative study and its geologic significance, *Acta Pet. Sin. 9,* suppl., 63-69, 1993.

Yang, Z.Y., J. Besse, V. Sutheetorn, H. Fontaine, and E. Buffetaut, Lower-Middle Jurassic paleomagnetic data from the MaeSot area (Thailand): Paleogeographic evolution and deformation history of southestern Asia, *Earth Planet. Sci. Lett., 136,* 325-341, 1995.

Zhang, L.-S., Age, durée et magmatisme du décrochement Tertiaire du Fleuve Rouge, Yunnan, Chine, Ph.D. thesis, Univ. Paris 7, Paris, 1995.

Zhang, L.-S., and U. Schärer, Age and origin of magmatism along the Cenozoic Red River shear belt, China, *Contrib. Mineral. Petrol., 134,* 67-85, 1999.

N. Arnaud, Laboratoire "Magmas et Volcans", UMR 6524 CNRS, Université Blaise Pascal, 5 rue Kessler, F-63000, Clermont-Ferrand, France.

T. M. Harrison, W. M. Keck Center for Isotope Geochemistry, Department of Earth and Space Sciences and Institute of Geophysics and Planetary Physics, University of California, Los Angeles, 405 Hilgard Avenue, Los Angeles, CA 90024.

J. R. Kienast, Laboratoire de Pétrologie, Minéralogie, Métallogénie, UPRES-A 7058 CNRS, Université Denis Diderot, 4 Place Jussieu, F-75252 Paris Cedex 05, France.

R. Lacassin, P. H., Leloup, A. Replumaz, and P. Tapponnier, Laboratoire de Tectonique, Mécanique de la Lithosphère, UMR 7578 CNRS, Institut de Physique du Globe de Paris, 4 Place Jussieu, F-75252 Paris Cedex 05, France. Leloup@ipgp.jussieu.fr

Phan T. T., Institute of Geological Sciences, NCNST Technology, Hanoi, Vietnam.